THE TEMPERATURE STRUCTURE OF THE QUIESCENT REGIONS OF THE SOLAR CORONA

Carl Alexander de Rouillon Spencer Foley

Mullard Space Science Laboratory
Department of Space and Climate Physics
University College London

Submitted to the University of London
for the degree of Doctor of Philosophy

August 1998

Abstract

This thesis addresses the energy balance in the solar corona, and consequential requirement upon the ubiquitous heating mechanism. To this end the observations of the quiescent regions of the solar corona made with the Yohkoh Soft X-ray Telescope are utilised. These observations are most sensitive to coronal plasma in the region of two to ten million Kelvin, and thus provide a view of the most energetic parts of these regions where heating would be expected to take place. In all regions investigated the temperature is observed to increase with height above the solar limb. This is interpreted as evidence of sustained heating up to the maximum observed height of almost several hundred megametres (one solar radius). A more refined examination of the energetics along a resolvable complex of magnetic elements (Coronal Loop), and through the axis of an arcade is used to determine the most suitable heating mechanism to reproduce the observed soft X-ray emission.

Contents

List of Figures

List of Tables

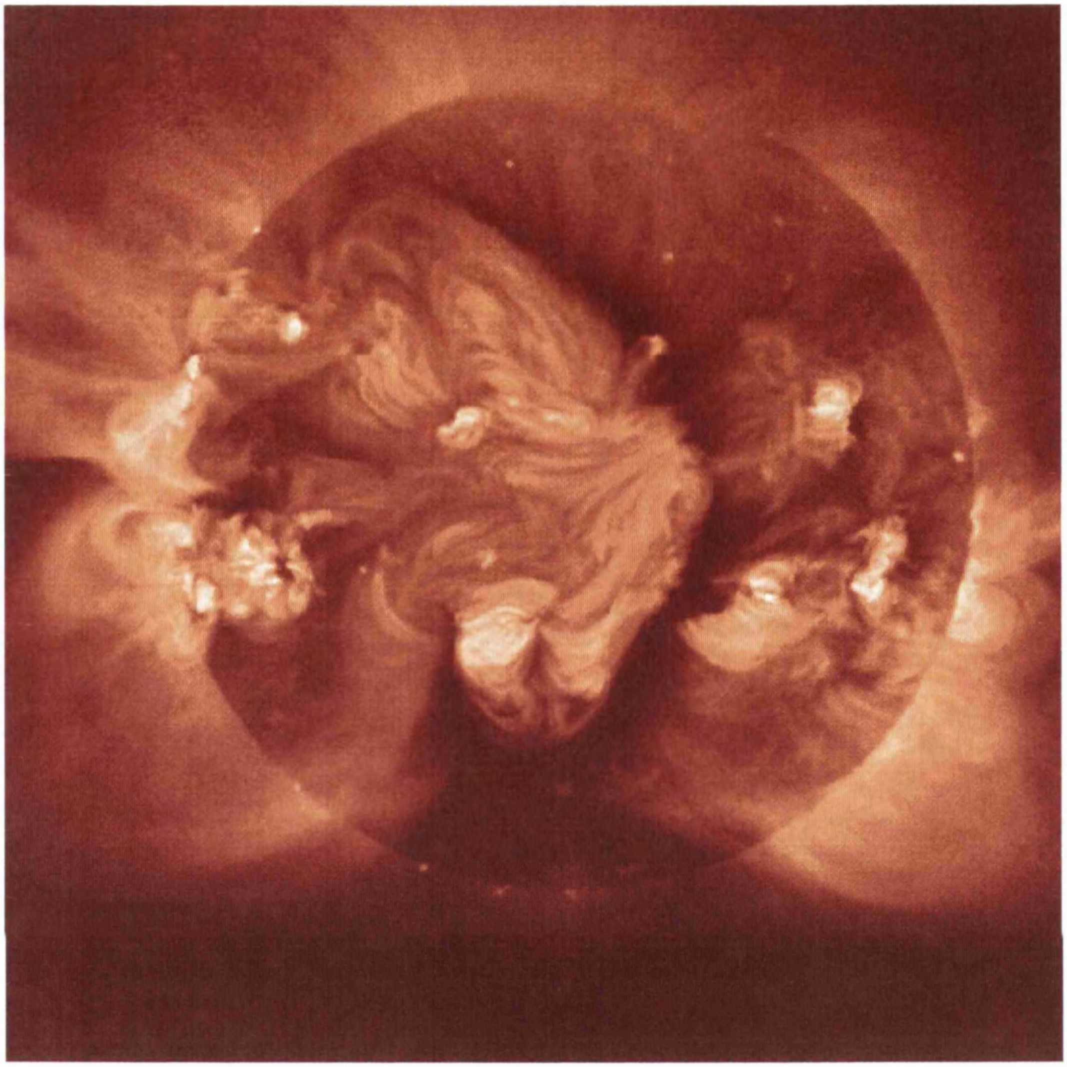

In 1933 Rosseland reviewed the problems of the corona and observed that the corona " has stimulated speculation to the breaking point", " the familiar laws of nature are set at naught in the corona " He hastened to add that experienced physicists are not very willing to accept such an explanation.

- The Sun , ed Kuiper, G.P. - 1952

Chapter 1

Introduction

The Sun's atmosphere is hot, tenuous, and magnetically dominated. The temperature increases strongly from a few $\times 10^3$K at the solar surface to temperatures in the corona of a few $\times 10^6$K. This truly dramatic increase occurs over a relatively small distance of about 10^4Km and clearly from the second law of thermodynamics requires a direct heating mechanism. The search physically and conceptually for this heating mechanism has been an active area of research for solar physicists, both observationally and theoretically, for over half a century now.

The hot nature of the solar corona may in some part be related to its tenuousness; in the corona the typical density is of the order of 10^{-13} Kg m^{-3}. Due to this observational fact the actual energy budget required to sustain such enhanced temperatures is relatively small. In fact the total energy budget for the corona is only approximately $10^{-5}\times$ the total radiative loss from the solar surface. This demonstrates that the heating mechanism for the corona may appear to be rather unassuming in its operation. Indeed this has stimulated much work on the theory of the most fundamental forms of energy transfer the most notably associated with sound waves and other similarly refined heating mechanisms.

In the following sections the current understanding of the structure of the Sun's atmosphere, and the history of the observations which form the basis of this understanding are reviewed.

1.1 A Brief Observational History of the Corona

The modern study of the Sun's corona commenced in the last century with observations made during eclipse. These observations were aided by one which occurred in 1842, the totality of which was visible over much of southern Europe. The major breakthrough of the work for this period was in correctly identifying the nature of the corona and its requirement for direct heating mechanisms. These defining results included: (1) the observation of coronal emission lines by Young (1869); (2) the extent of the emission lines were found to be inconsistent with a hydrostatic corona (Lockyer, 1870; and subsequently by Mitchell, 1913); and (3) the broadening of the coronal emission lines (Hastings, 1873). The conclusion which was drawn by many was that these problems could only be reconciled if the corona were orders of magnitude hotter than the photosphere. The implication of this conclusion, namely the requirement for direct heating of the corona, demanded that more substantial evidence be obtained. This was achieved in the combined works of the scientists Grotrian, Edlén, and Lyot.

Lyot (1937) on investigation of the line width for the 530.3nm line found this line to have a width greater than that due to thermal Doppler broadening alone. However, a specific temperature could not be assigned to the width determined since the ion's weight was unknown. Two emission lines were identified by Grotrian (1939) located at the wavelengths 637.4 and 789.2nm. These were found to be due to forbidden transitions of highly ionised Fe lines which had been documented (from laboratory spark discharge experiments) by Edlén (1942). The ionisation energies involved with these transitions were consistent with temperatures in the region of 10^6K being present within the corona. The final piece of evidence which satisfied most observers of the validity of the accentuated coronal temperatures was the radio observations of the Sun in which the observed emission was consistent with thermal emission from a 1MK plasma (Martyn, 1946).

Plasma at these temperatures radiates most strongly in the X-ray regime. In fact it had been demonstrated by Hoyle and Bates (1948) that the flux of X-rays from the Sun could easily explain the E-region ionisation of the

Earth's ionosphere (a conjecture first proposed by Hulburt, 1938; and Vegard, 1938). However, observations in this wavelength range are complicated by the role the Earth's atmosphere performs in attenuating (re-processing) much of these harmful high energy radiations. To circumvent this obstacle rocket and space born instrumentation were required.

1.1.1 X-ray Observations

The first X-ray observations of the Sun were made by scientists at the US Naval Research Laboratory (NRL) in 1948 (Burnight, 1949). This used an experiment not dissimilar to that in which Roentgen had first discovered X-radiation. Photographic plates which were obscured by Aluminium and Beryllium filters, were propelled to a height of 130Km using a German V-2 Rocket. The plates, as in Roentgen's experiments were similarly blackened and thus began the exploration of the X-ray corona of the Sun and other stellar objects. These preliminary experimental observations were followed by more complex observations and observatories. These included spectrometers, and crude pinhole cameras to provide spatial as well as spectral resolution to some extent. A typical image obtained for this period is illustrated in figure 1.1 which was obtained by the Leicester group on the 17^{th} December 1964. Although the image is produced with simple pinhole optics, it still demonstrates the separation of the corona into three physically distinct regions; the polar regions, which are most reduced in soft X-ray emission; then a general emission from the rest of the corona in which limb brightening could be resolved ; and bright localised intense emission which were found to be associated with location of sunspot regions. These bright regions were found to account for almost 90% of the soft X-ray flux below 1.5nm (Culhane, 1966), and due to their appearance were termed coronal condensations. The typical scale of these structures in the images were however comparable with the spatial resolution of the camera (2 minutes of arc) and thus observations were required with better spatial resolution to determine if these were in fact condensations as they appeared.

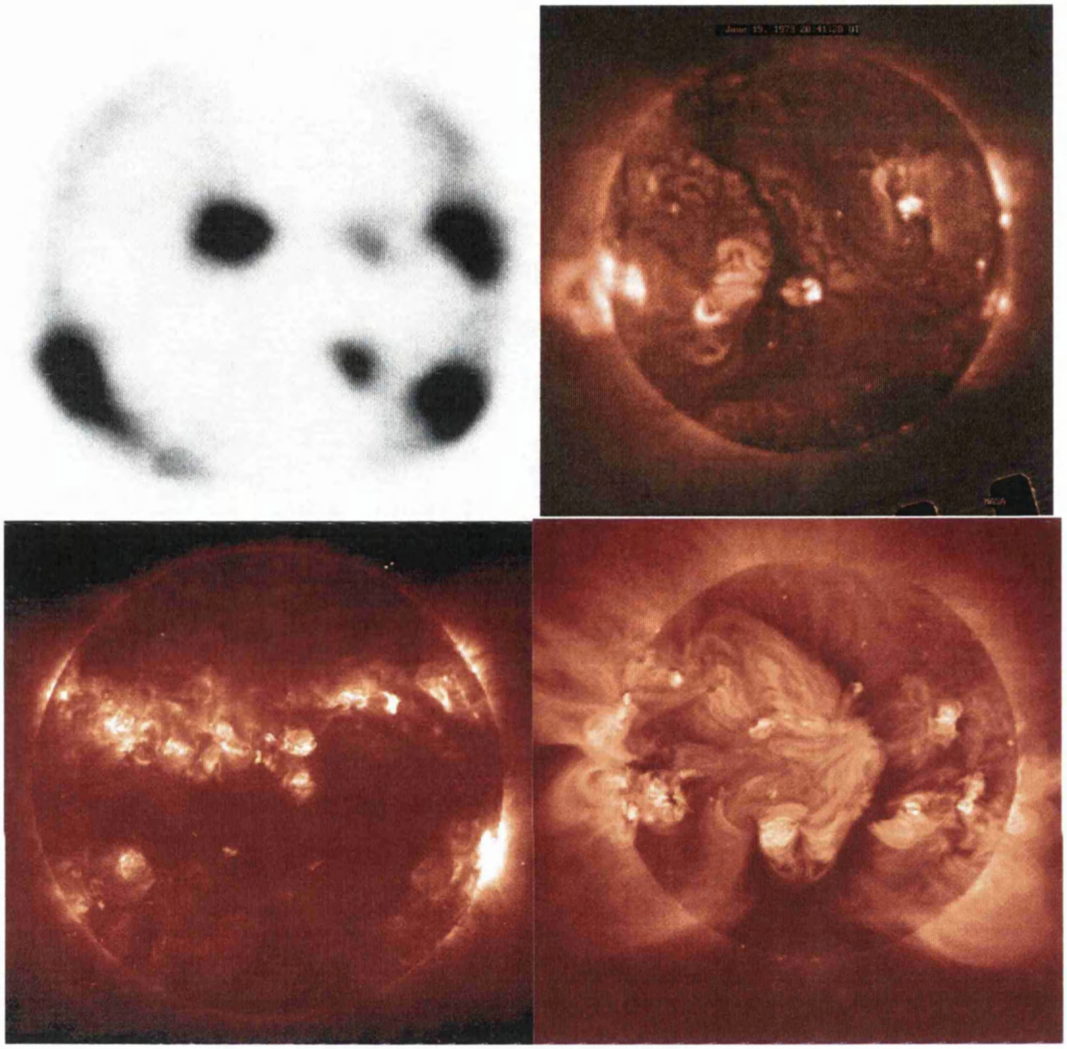

Figure 1.1: **Our Evolving View of the Sun** (Top-Left) An observation of the Sun's corona obtained on the 17^{th} December 1964, with instrumentation mounted in a sounding rocket. This was produced by the Leicester group and represents one of the optimum images of the Sun's corona of that time (*from Culhane, 1966).* (Top Right) The improvement that grazing incidence optics has in imaging the corona is illustrated dramatically in this image obtained with the S-052 instrument mounted on Skylabs ATM (*from web*). (Bottom Left) With the advance of multilayer optics normal incidence telescopes such as NIXT (1988-1993) were possible (*from http://hea-www.harvard.edu/SSXG/sept89-big.gif*), (Bottom Right) The vast improvement and excellent selection of filter bandpass to emphasize the coronal plasma is evident in this Yohkoh image of the Sun (*Produced at MSSL*)

.

1.1.2 Coronal Loops and the Scaling Law

A dramatic improvement in observing of the X-ray corona was achieved with the launch of the Skylab space station which had a collection of Sun observing instrumentation on the Apollo Space Telescope Mount (ATM). One of these telescopes (S-054) utilized grazing incidence mirrors to form a soft X-ray image of the Sun with an effective spatial resolution of a few arcseconds. These observations demonstrated that the condensation regions were in fact composed of complex loop like structures (see top-right figure 1.1). The loop structures were subsequentually demonstrated to be well correlated with current-free extrapolations of the observed photospheric magnetic field (Poletto *et al.*, 1975). This marked an important evolution in the way the corona was envisioned, and led to the concept that the corona was entirely composed of discrete coronal loops which operate as independent mini-atmospheres.

This concept was embodied in the work of Rosner, Tucker and Vaiana (1978, henceforth referred to as RTV) who developed a scaling law for quiescent coronal loops. These loops were assumed to be in a state of hydrostatic equilibrium. This allowed them to greatly simplify the energy conservation equation, by dropping terms representing the gradient of enthalpy, kinetic and gravitational energy. Further manipulation and thermal stability arguments, concluded with an expression which represented the variation of maximum (located at the top of the loop) loop temperature, T_m, with loop pressure, P, and Length, L;

$$T_m = 1.4 \times 10^3 (PL)^{1/3} \tag{1.1}$$

This was found to provide reasonable fits to observations over a wide range of T_m and L values. More recently Kano and Tsuneta (1995) have reinvestigated this relationship and found a modified expression represented the data. The difference was attributed to the different sensitivity of the instruments used for the analysis.

1.1.3 Coronal Holes

Coronal holes are the most clearly distinguished regions of the Sun's corona when observed in the soft X-ray regime. They appear dark and devoid of any intrinsic coronal emission. They originate in large unipolar regions (Babcock and Babcock, 1954) which are magnetically open (Altschuler *et al.* 1972). Using the image data provided by Skylab's soft X-ray telescope, Krieger *et al.* (1973) extrapolated the fast speed wind streams observed in-situ back to coronal holes located in the equatorial regions. This was more recently confirmed for the polar holes during the Ulysses pass over the Sun's poles (Marsden and Smith, 1995). Measurements of the electron temperatures and densities for the coronal hole regions (see Munro & Withbroe 1972, Raymond & Doyle 1981, Habbal *et al.*, 1993) have demonstrated that these regions are cooler than the surrounding quiet corona, with temperatures in the region of 1-1.5MK. At such temperatures the requirement for non-thermal energy sources to further accelerate the wind to flow velocities observed at 1AU (800km/s) is great, and has stimulated considerable work into ways in which this can be achieved.

The data presented in this thesis were obtained using the Yohkoh (Solar-A) spacecraft. This spacecraft has been operating successfully now for almost seven years, obtaining broadband soft X-ray images of the Sun's corona, like that illustrated in the lower right of figure 1.1, every few minutes. The instrument is described in chapter 2, and its Point Spread Function (PSF) in chapter 3.

1.2 Present Day View of the Corona

The presence of the strong magnetic field which emerges from the photosphere and threads the corona has dramatic consequences for the behaviour of the plasma of which it comprises. The magnetic pressure dominates the plasma pressure so that the magnetic topology defines the configuration of the coronal field and flows. The ratio of these two forces is generally termed the plasma beta ($\beta = \frac{P_{gas}}{P_{mag}}$). A typical value of this β for the quiescent regions of the Sun's atmosphere is 10^{-3} which illustrates one of the more important characteristic of the corona, namely that the magnetic field strongly dominates flow of material and energy within the solar atmosphere.

Region	Height Range Km	Electron Temperature K	Density e^-/cm^3
Outer Corona	2×10^6-10^7	10^5	10^1
Inner Corona	10^4-10^6	2×10^6	10^8
Transition region	2000-2050	10^5	10^{10}
Chromosphere	100-2000	10^4	10^{14}
Photosphere	0	6×10^3	10^{16}

Table 1.1: The different regions of the Sun's atmosphere, and their relative temperatures and densities

The corona is separated from the visible solar surface, the photosphere by the chromosphere. The typical values for the different regions are tabulated in table 1.1. The chromosphere gets its name from its characteristic pink flash when observed during eclipse. The colour is representative of the Hα emission which dominates in this region. The steep temperature gradient which exists between the chromosphere and corona, called the transition region, has been demonstrated by Athay (1990) to be well represented as a constant pressure region in which the temperature at different heights is governed by the amount of heat flow from the overlying corona until radiative efficiency increases in the chromosphere (due to strong density enhancements). In this sense these lower regions of the Sun's atmosphere simply respond to the heating that occurs in the corona, and the energy deposition is small in comparison to that which flows through it from the corona.

1.2.1 Coronal Emission

The emission of the corona has been modelled using the solar abundances which are summarised in Meyer (1985), in combination with the spectral calculations and data presented in Mewe *et al.* (1985,86). An example is illustrated for an isothermal coronal plasma at 2MK in figure 1.2. The emission at these typical coronal temperatures is dominated by emission lines which represent bound-bound atomic transitions. The continuum has its origins from free-free transitions (Bremsstrahlung) and free-bound transitions (recombination radiation).

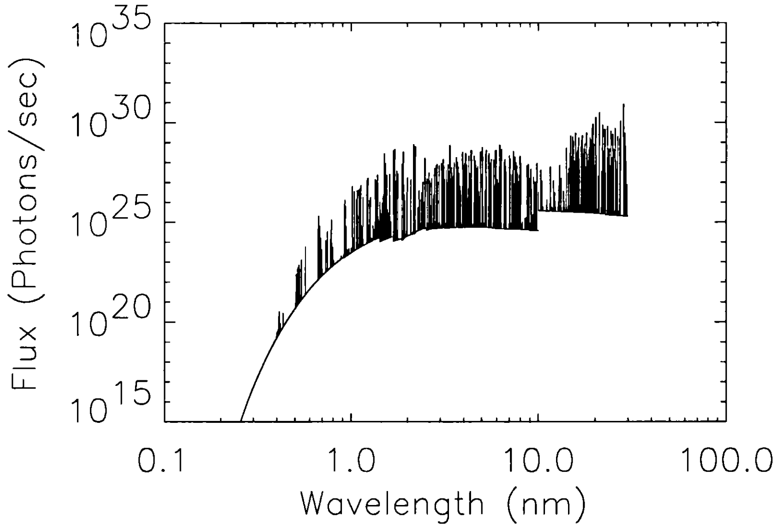

Figure 1.2: The coronal emission spectrum generated using the results of Mewe *et al.* (1985,86) for a coronal plasma of 2 million Kevin. The black body like region represents the coronal Bremsstrahlung (electron - atom collisions) and recombination radiation, whilst the lines represent bound-bound atomic transitions

1.2.2 Scale Height of Emission

The effect of gravity on the coronal plasma is to stratify it creating a barometric atmosphere, the density and pressure of which decays exponentially with a characteristic scale height. If we assume spherical symmetry and neglect radial magnetic forces this may be illustrated using momentum conservation :

$$\frac{dP(r)}{dr} = -(N_e + N_i)\mu g(r) \tag{1.2}$$

where P(r) is the gas pressure at distance r, g is the gravitational acceleration, N_e and N_i are the electron and ion number density, and μ the effective particle mass. For the Sun where the helium abundance is $\sim 10\%$ μ has a value of 1.04×10^{-24}g

Using the ideal gas law this becomes

$$\frac{dP(r)}{P} = -\frac{\mu g(r)}{kT}dr = -\frac{dr}{\mathbf{\Pi(r)}} \tag{1.3}$$

where k is Boltzmann's constant T is the effective temperature of the plasma and

$$\mathbf{\Pi(r)} = \frac{kT}{\mu g(r)} \tag{1.4}$$

is the scale height. Its value is $\sim 5800\mathbf{T}cm$ and $7000\mathbf{T}cm$ at heights of 1.1 and $1.2R_{\odot}$. For small regions, over which the corona may be assumed isothermal and the variation of $\Pi(r)$ small, equation (1.3) may be integrated to find

$$P = P_o \exp[\mathbf{\Pi_r}^{-1}(1-\rho)] \tag{1.5}$$

where ρ and Π_r represent r and the scale height in units of solar radius. An expression for the electron number density is obtained by interchanging N_e and N_{eo} for P and P_o

$$N_e = N_{eo} \exp[\mathbf{\Pi_r}^{-1}(1-\rho)] \tag{1.6}$$

The expression which represents how rapidly the corona falls off with height is useful in estimating coronal temperatures when other suitable diagnostic techniques are unavailable. Although the scale height is dependent on isothermal and static conditions being realised the temperatures often do not differ from those found using other techniques (*see* Guhathakurta *et al.* 1992).

1.3 Heating Mechanisms

The ultimate source of mechanical energy for the Sun's corona is widely accepted as originating with the turbulent motions of the Sun's convective zone. These motions give rise to a number of characteristics which are reflected in the photosphere, namely granulation and other generally random motions. These motions are responsible for waves of various mode which can provide sufficient energy to heat the corona if suitable dissipation mechanisms exist.

1.3.1 Wave Heating

From the discussion above, acoustic and magnetohydrodynamical waves are a natural candidate for heating the solar atmosphere. Indeed, these were generally accepted as the most likely candidates for the hot corona after it was discovered (Alfven, 1947; Biermann, 1948; Schwartzschild, 1948). However, with the corona being 10^7 times less dense than the photosphere the propagation of these (compressional) waves is highly improbable with most of the power being reflected. Waves which are believed to reach the corona with sufficient power to accommodate the energy requirements (10^5 - 10^7 ergs cm^{-2} s^{-1}) are Alfven waves. These are transverse waves of the magnetic field which are relatively unimpeded by the large gradients of density between the chromospheric corona transition. Consequentially mechanisms by which they dissipate their energy are more complex. The most popular of these mechanisms include resonant absorption (see Davila, 1987; Grossmann and Smith, 1988; and Ofman, Klimchuk and Davila, 1998), and phase mixing (see Heyverts and Priest, 1983; Abdelatif, 1987; Parker, 1991 ; and Hood, Gonzalez-Delgado, and Ireland, 1997). The former of these dissipation mechanisms has been tested and is used to heat plasmas within Tokamaks.

1.3.2 Flares

Solar flares are a dominant energy release mechanism in the corona, with each radiating up to 10^{32}ergs (*see* Culhane, 1997). Their occurence rate has been found to vary linearly with the total energy released raised to a power, typically of the value -1.8 (see Hudson, 1991). It is a natural hypothesis to extrapolate these events to lower energies, and then to determine if the energy supplied by the very small but more frequent events would be adequate to supply the energy required to sustain the corona. Numerical simulations performed by Georgeolis (1996) confirms that this is expected as the scale of energy release becomes more elemental. Hudson (1991) points out that for the smaller events to dominate the powerlaw index must less than -2. Recent observations from SOHO EIT reported in Krucker & Benz (1998) find the powerlaw for microflares to be of the order ; -2.6 to -2.3.

1.3.3 Velocity Filtration

The velocity filtration model of Scudder (1992,94) provides an alternative way to form a corona without the requirement for direct heating mechanisms. The model requires that the particle distribution in the transition region be non-Maxwellian and possess a high energy tail (evidence for such a particle distribution is found in studies of the solar wind at 1AU). This would naturally lead to higher temperatures at greater heights as the more energetic electrons overcome gravity. Hara (1994) points out that the Scudder model predicts a variation of nonthermal velocity, η, with electron temperature, T_e, which goes as $\eta \propto T_e^{0.5}$. In Hara's work, evidence for just such a distribution is not found for the corona. Anderson *et al.* (1996) investigated the likelyhood that the velocity filtration model could explain the EUV intensities obtained from Skylab data. This work demonstrated that the emission measure distribution of plasma in the lower transistion region, but not the corona, could be reproduced with the model.

1.4 Summary

It is the aim of the rest of the work presented here to determine the average state of the coronal plasma in the more quiescent regions. This begins in chapter 2 with a description of the soft X-ray telescope flown on the Solar-A (Yohkoh) spacecraft, and the analysis techniques used. In **Chapter** 3 the telescope scattered light characteristics are described. **Chapter** 4 describes the analysis of a polar coronal hole. **Chapter** 5 the temperature structure of diffuse regions of emission. In **chapter** 6 this is extended to a large scale loop structure. **Chapter** 7 summarises the thesis and discusses the future extension of the work.

Chapter 2

The Yohkoh SXT

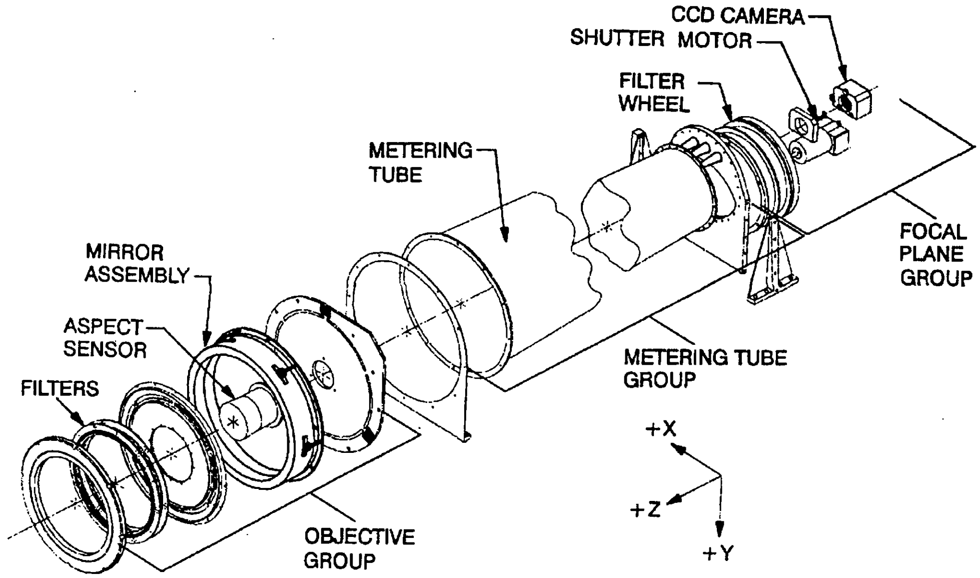

Figure 2.1: The optical bench of the SXT (from Tsuneta *et al.*, 1991), illustrating the major components which comprise the telescope.

In this chapter a general overview of the construction and operation of the Yohkoh Soft X-ray Telescope (SXT) is given. Tsuneta *et al.* (1991) is the primary source of information with additional sources being ; Hara (1996), the Yohkoh Analysis Guide (YAG), and the various calibration notes which are distributed as part of the Yohkoh analysis software installation.

2.1 Overview

Bringing X-rays to a focus is a problem which has been addressed since the first experiments by Roentgen where it was concluded that the refractive index must be very close to unity. The consequence of this is that X-rays cannot be focused by conventional optical lenses. Instead grazing incidence reflections with angles typically less than $\sim 1^o$ are required. Popular designs for telescopes which utilize grazing incidence to focus X-rays are based on the Wolter design (Wolter, 1952,52a). These telescopes use the focusing properties of concentric surfaces of rotation to bring the X-rays to a focus. Typically the mirrors are nested to provide optimal effective areas which are substantially reduced because of the requirement for grazing incidence. However, in the case of solar telescopes the requirement for large effective area is much reduced because of the relative brilliance of the Sun. The Yohkoh SXT is similarly a grazing incidence telescope but uses a novel design adapted from the simpler Wolter designs by Nariai (1987, 88) to optimize the off-axis response at the slight loss of the on-axis response. The telescope is designed to obtain broadband images of the solar corona in the 0.3-4.5nm wavelength range.

A schematic of the primary elements which lie along the optical bench can be found in figure 2.1. These consist of the grazing incidence mirror, the CCD camera, dual filter wheel, and entrance filters. The detector is a Charge Coupled Device (CCD) and consists of 1024$\times$1024 pixel elements each of which subtends $\sim$ 2.45 arc-seconds (which corresponds to $\sim$1.8Mm on the surface of the Sun). There is also a capability for 2$\times$ and 4$\times$ summing of the images on chip which allows images to be produced which are either half or quarter the full resolution. In its normal mode of operation the SXT records a Full Frame Image (FFI) of the Sun every few minutes in half resolution. The dual filter wheel, which is located at the focal end of the optical bench just before the CCD, provides broadband spectral selection. The front filter wheel is used to select whether a soft X-ray image or optical image is recorded, whilst the rear filter is used to provide plasma diagnostics in the soft X-ray regime. The various filter positions available for use is tabulated in table 2.1.

Commanded Position	Front Wheel	Rear Wheel
1	Open	Open
2	3 nm @ 4310	Al .126 μm
3	CCD Flood Lens	Al/Mg/Mn
4	Glass Diffuser	Be 119μm
5	1.4nm @ 4580	Al 11.6μm
6	8% Mesh	Mg2.52μm

Table 2.1: The possible filter positions of the Yohkoh SXT filter wheel. The filters in the front wheel are used to select whether an optical/X-ray image is registered at the CCD. Whilst the rear filter is used for diagnostics in the X-ray regime

The CCD operates in a charge accumulation mode in which the charge liberated by the incident photons in each pixel collect before being read out. The duration of this is actuated by a rotating shutter located just fore of the CCD. This has been identified as being responsible for a jitter in the pointing of the spacecraft when periods of high cadence are in operation (flare mode); in its quiet mode the pointing accuracy of the SXT is better than 1 pixel. The charge which is recorded on the CCD is converted into the Data Number (DN) which represents an arbitrary number of electrons liberated in the CCD. A single DN represents ~100 electron hole pairs being liberated in a CCD pixel (one 365 **eV** photon). The data are then compressed using a square root algorithm to 12bits before being transmitted to a ground station. This is reprocessed into orbit files which are distributed to the relevant institutions.

2.2 The Analysis Filters

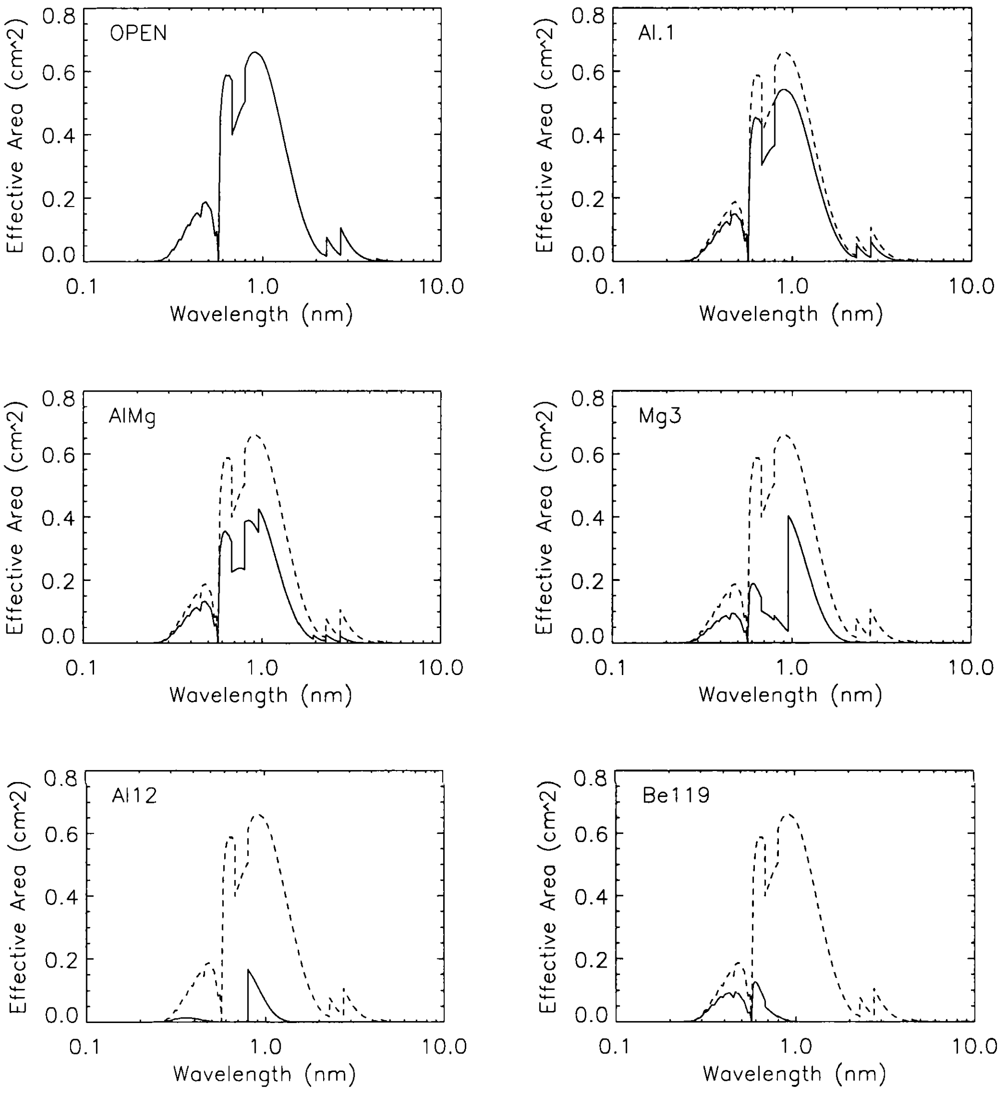

Figure 2.2: The effective area of the SXT's various filters (solid line). The dotted line represents the open case as illustrated in the top left hand panel.

The analysis filters of the SXT were carefully selected to provide the optimum temperature diagnostics in the 1-20MK regime. This is made possible by the dominance of the line emission in the 0.3-5nm bandpass (see figure 1.2). The coronal spectrum produced using the atomic information and abundances described in §1.2.1 is convolved with the overall response function of the telescope.

The bandpass of each of the filters is illustrated in figure 2.2. The signal which is recorded on the CCD is the convolution of the observed solar spectrum with the response function of the telescope. The latter includes the mirror reflectivity, filter transmission, mirror effective area, and CCD quantum efficiency. These are encompassed in equation (2.1) which represents the Filtered Spectrum Integral (FSI; Maxson & Vaiana, 1977) the predicted response of the SXT to an isothermal coronal plasma.

$$\mathrm{F_i(T_e)} = \int \psi(\lambda, \mathrm{T_e})\nu_\mathrm{i}(\lambda)\mathrm{d}\lambda \tag{2.1}$$

where T_e is the electron temperature and $\nu_i(\lambda)$ the overall response of the SXT for filter i. $\psi(\lambda, T_e)$ represents the coronal emission line and continuum spectrum determined by Mewe *et al.* (1985, 86) whilst using the abundances of Meyer (1985). The FSI's determined for all the X-ray analysis filters on the SXT are illustrated in figure 2.3. The uncertainties in the curves are estimated to be less than 2 percent (see Porter & Klimchuk, 1995).

The intensity, I, as measured by the SXT for an isothermal plasma may then be expressed by

$$\mathrm{I} = \mathrm{F_i(T_e)} \int \mathrm{N_e}^2\mathrm{dv} \tag{2.2}$$

where N_e is the electron density, dv is the line of sight element. $\int N_e^2 dv$ represents the emission measure.

2.3 Plasma Parameters from SXT Images

The method used for extracting plasma parameters from the SXT data are based on a procedure first used in the Skylab era by Vaiana, Krieger, & Timothy (1973). It is based upon the use of the average emission observed almost simultaneously through different filters over a broad wavelength range. It was first implemented in the case of the SXT by Hara *et al.* (1992). The method uses the ratio of the intensities observed simultaneously through the two filters which is only dependent on temperature.

$$\Gamma = \frac{I_1}{I_2} = \frac{F_1(T)}{F_2(T)} \tag{2.3}$$

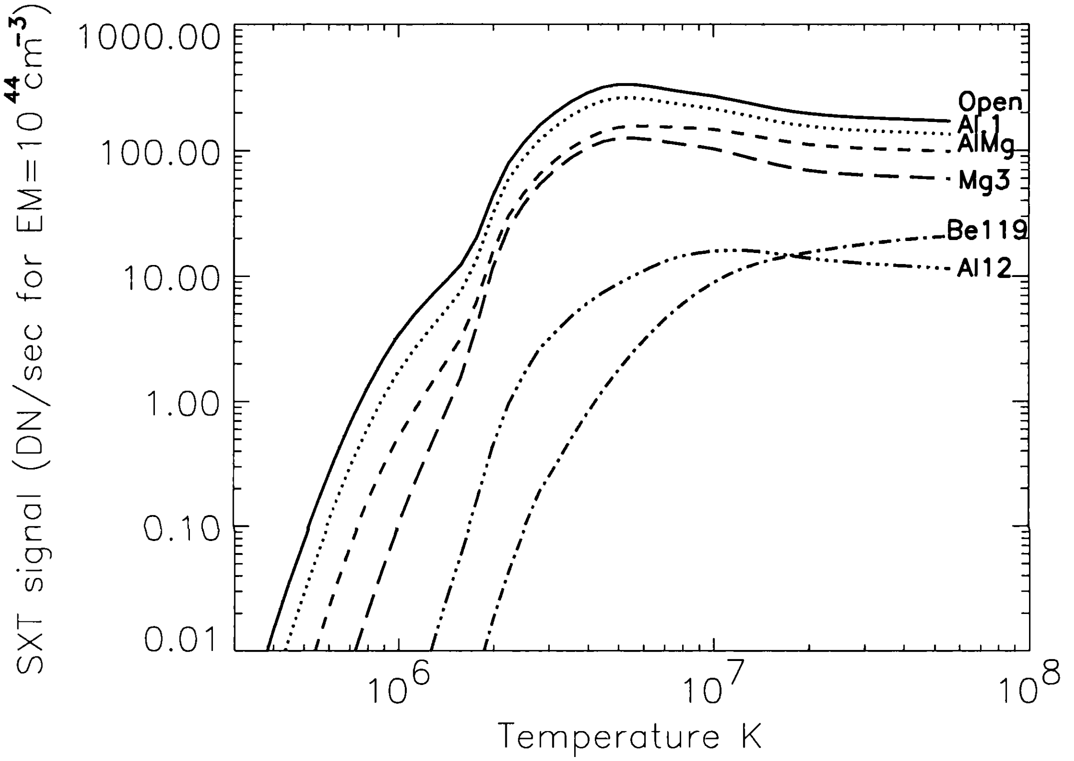

Figure 2.3: The response of the SXT for each of the filter 2 positions (front filter in open position) to an isothermal coronal plasma (Lemen et al., 1991). The curves are generated by convolving the response of the SXT with the theoretical continuum spectrum and line spectrum of Mewe *et al.* (1985,86) whilst using the abundances of Meyer *et al.* (1985).

The ratio of the signal through two SXT filters may be used along with the FSI's to determine an isothermal temperature (T_e) for the column of plasma in the line of sight. The ratios used in much of the SXT data analysis are illustrated in figure 2.4. The corresponding line of sight emission measure ($\int N_e^2 dv$) of the plasma is related to the intensity (I) observed through the SXT and the FSI by

$$\mathrm{EM} = \int N_e^2 dv = \frac{I}{\mathrm{F_1(T_e)}} \tag{2.4}$$

The SXT data can thus be used to reproduce accurately the temperature and emission measure of an isothermal plasma. However, if there is a wide distribution of temperatures in a pixel reconstructing the original differential emission measure distribution in most cases is not possible [1]. The resultant isothermal temperature in this case is highly uncertain and may only be used for comparative purposes.

2.4 Vignetting

The vignette function of the SXT represents the variation of effective area with increasing off-axis angle. This variation is due primarily to the reduced collecting area of the mirror surfaces and secondly the obscuration of the optical axis by the telescope construction elements and baffles (Fuller, Lemen, & Acton, 1994). The second of these dominates at larger off-axis angles, as illustrated in figure 2.5, by an increased reduction of effective area outside 21 arc-min. It is particularly important to understand the vignetting characteristics when there is an interest in the absolute and relative value of the emission measure ($\int N_e^2 dl$) of a particular region. The effective area at three different energies (C_K 0.3keV, Al_K 1.5keV, and Ag_L 3keV) was evaluated preflight in a test facility located at White Sands Missile Range (WMSR). No significant difference was found between the responses for the C_K and Al_K lines whilst the response for Ag_L was found to be significantly steeper. The corrections are thus split into a low energy and high energy correction. Since I focus on low energy emission the lower energy correction has been

---

[1] This is due to most observations being taken through less than three filters when four filters are required for a two temperature analysis

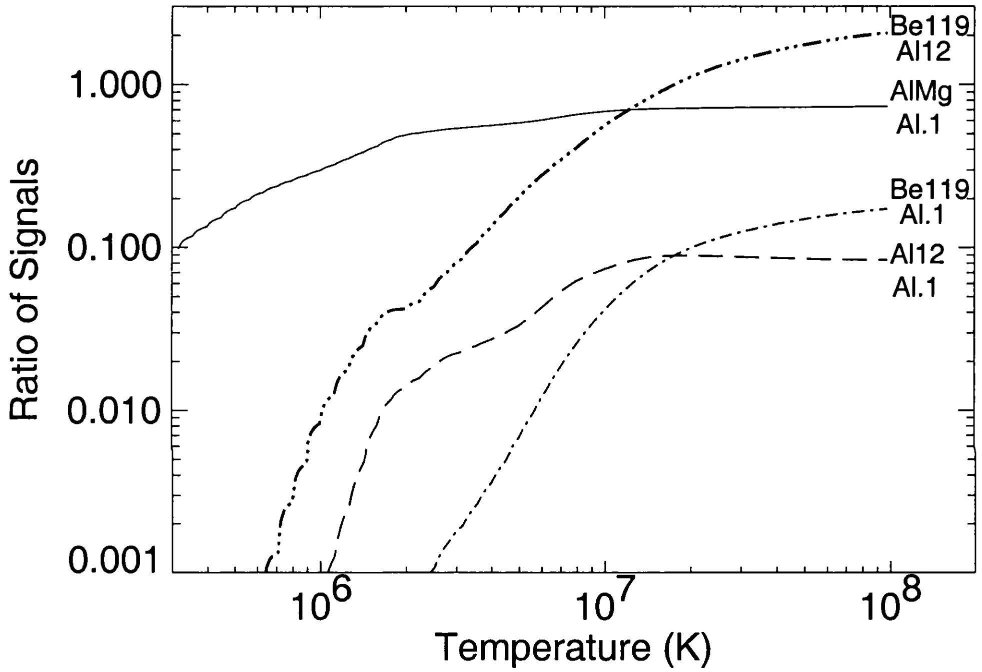

Figure 2.4: The ratio of the response curves which gives a reliable indication of the plasma temperature assuming there is not a broad distribution of temperatures in each pixel.

used throughout this thesis.

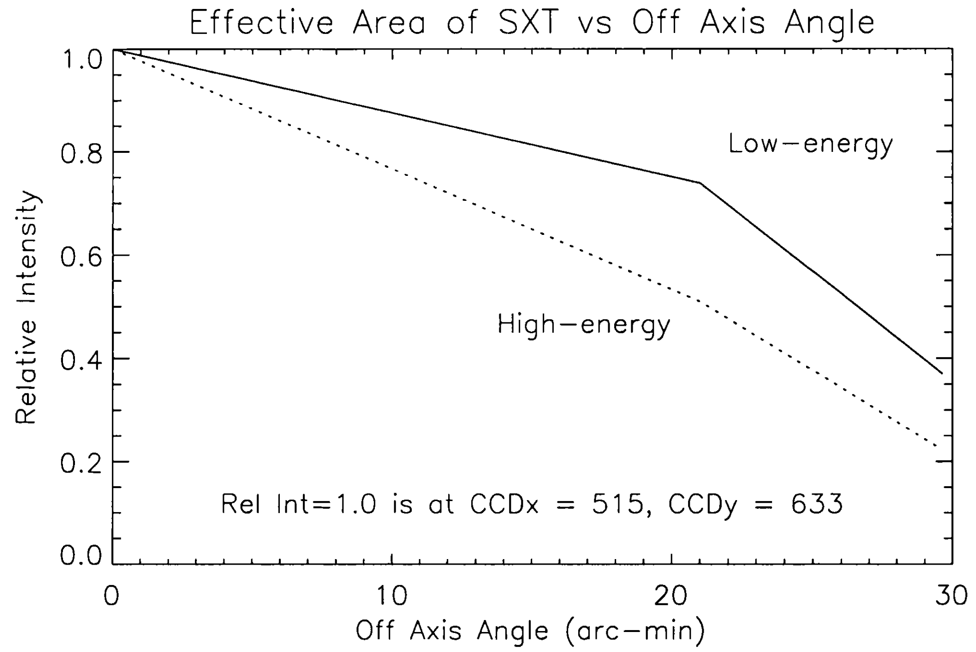

Figure 2.5: The effective area of the SXT as determined from the WMSR data

2.5 Point Spread Function

When light is reflected from an imperfect interface the reflected radiation consists of a specularly reflected component and a diffuse component. The effect of the scattered light is to reduce the throughput of the telescope (since some of the signal will not reach the focal plane) and reduce the telescopes effective resolution due to the diffusely scattered light. On a large scale the broad angle scatter will reduce the overall image contrast. The evaluation of the small angle scatter has been evaluated prior to the launch of the SXT (see figure 2.6). Measuring the larger angle scatter was made difficult in a laboratory due to its relative faintness and the lack of a suitable high intensity sources. For this reason it has been necessary to evaluate it in flight. This has been performed by Hara (1994) but is re-examined in the next chapter.

The small angle scatter was investigated in some detail by Martens et

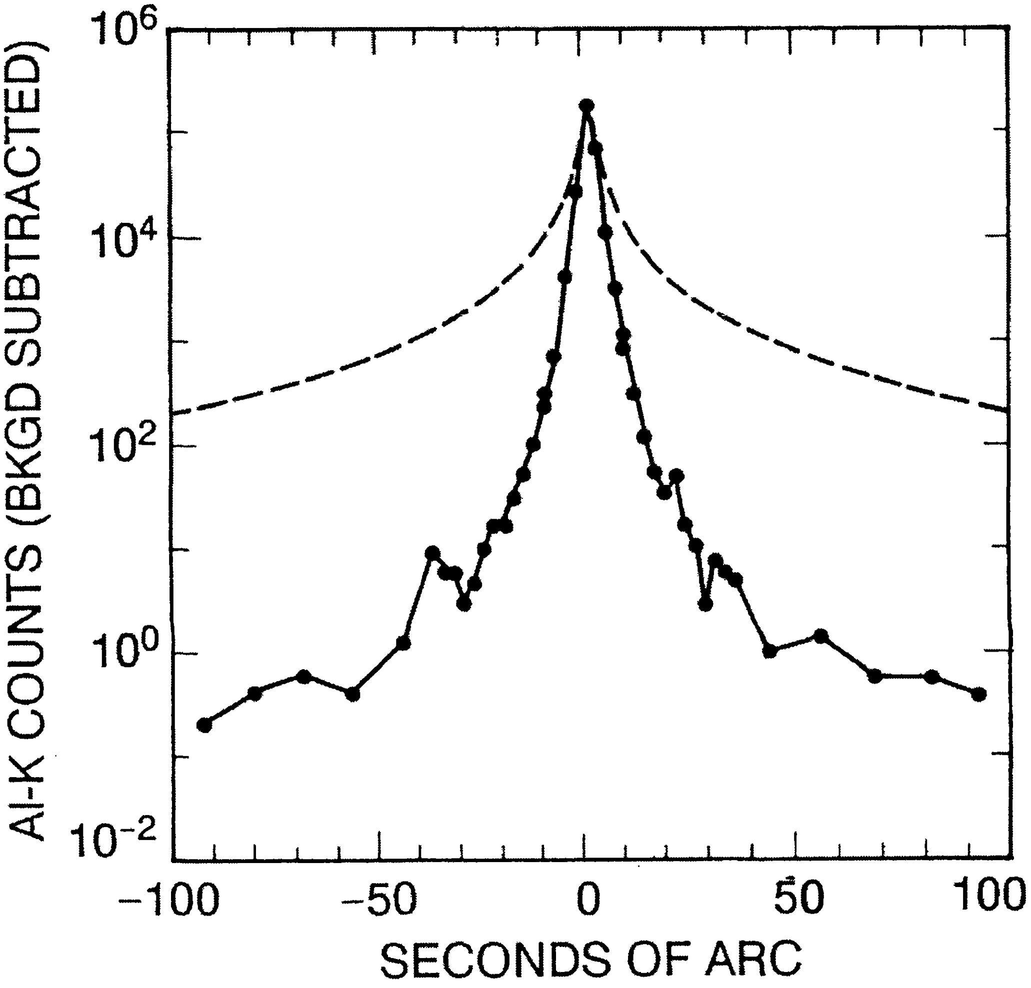

Figure 2.6: The Measured Point Spread Function (PSF) for the Yohkoh SXT and the Skylab SO-54 telescope. Great improvement is evident in the level of scattered light for the SXT (*from Tsuneta et al. 1991*).

al., (1994). The result of this was that the small angle PSF could be characterized by a Moffat function. This representation was found to be highly vignetted at large off-axis angles with the major axis typically being tangential to the arc at that point. Correction for this is only necessary for analysis of regions of intense emission such as those observed during flaring. An alternative process for determining the distribution of the emitting region has been established for the SXT data by Sylwester *et al.* (1996) who uses an adaptive Lucy method to evaluate the small angle scattered light.

2.6 Data Reduction

The data (which are held at the MSSL) are received in orbit files for each of the instruments (SXT, Hard X-ray Telescope, Bragg Crystal Spectrometer, Wide Band Spectrometers) on a single data tape. The data are in an uncalibrated format, but analysis routines to correct the data are distributed by the instrument teams to the scientific community [2]. In the case of the Yohkoh SXT the data corrections required are applied in a modular fashion by a main routine called sxt_prep. These corrections include data decompression (and uncertainty evaluation), dark pixel subtraction, image co-alignment, and vignette corrections. Additionally, other necessary corrections are those due to image over-exposure and telescope scattered light. The scattered light corrections described in section 3.3 of the next chapter have all been written into a single routine (*sxt_scatim_spider*) which has been made available as part of the Yohkoh software distribution.

2.6.1 Dark Current and The South Atlantic Anomaly

The dark current, hot pixels, and cosmic rays have the most detrimental effect on measurement of temperatures. This is because the noise can uniformly bias the signals recorded through each filter. It can then act as a secondary temperature component in the region of 10MK for the thin filters. It is obvious that the possible inclusion of this and understanding of its uncertainty must be properly understood if any meaningful conclusions are to be made from the data. The dark current and CCD hot pixels are evaluated in weekly intervals by recording the signal obtained from the CCD with the front filter in the closed position. Data obtained when the spacecraft is in the South Atlantic Anomaly (SAA) are substantially more prone to contamination by high energy cosmic rays; for this reason all the data obtained whilst in transit has been excluded from inclusion in this work. This was achieved by inspecting the radiation monitors which are part of the wide band spectrometer. Code to do this have been provided by Sam Freeland in the IDL program *saa_in*. In addition hot pixels are excluded from the analysis.

2.6.2 Scattered Light Evaluation

When selecting data for analysis another consideration is estimation of the telescope scattered light. This is investigated in detail in the next chapter. In its normal mode the SXT records images of various cadence to provide data for regions of differing brightness. However, due to the limited full well capacity of the CCD (approximately 10^5 electrons) the images obtained for the fainter regions frequently contain saturated regions. Thus, in order to evaluate the scattered light images the shorter cadence images must be used to replace the saturated regions. The total time required to obtain such a series of images can take as long as thirty minutes during which time the emissivity of the coronal plasma could have substantially changed. For this reason the analysis which is included in this thesis was selected from periods during which no appreciable change in solar activity was noted over the period of observation.

---

[2] available in the UK from the Yohkoh Data Analysis Center, YDAC

Chapter 3

Telescope Scattered Light

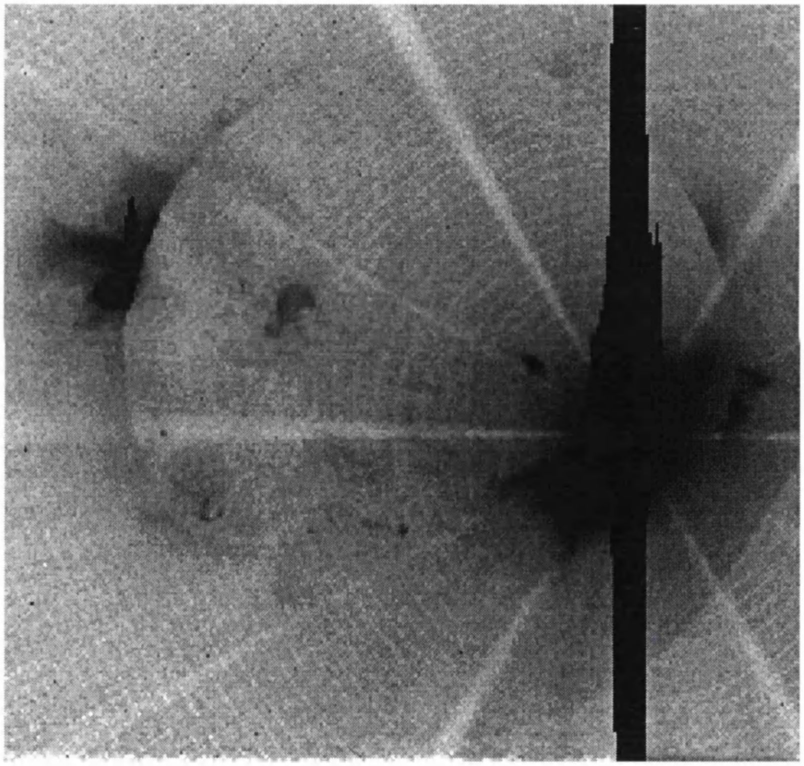

*The dominance of the telescope-scattered light from the intense solar flare located at the centre of the "***Spiders Web***". The web is formed by the attenuation of the scatter by the support structure of the filters (circumferential rays) and telescope (radial rays)*

3.1 Introduction

A fundamental problem in any imaging system used in astronomy is that associated with the imperfect nature of the reflecting surface. These imperfections are usually described in terms of a spatial frequency which is simply the reciprocal of the spatial wavelength. The spatial wavelength in turn represents the Fourier components of the surface deviation from ideal. The low and medium spatial frequency errors are due to the larger scale errors of figure. These surface deformations are associated with the manufacturing process and are responsible for the core portion of the PSF. The high frequency errors are due to a residual micro-roughness which often left behind even after careful polishing. This roughness is responsible for the large-angle scatter wings. This component of scatter results in part of the incident signal being spread over the entire field of view. The resultant images often appear with a halo surrounding most bright features. This often results in a significant reduction in image contrast which makes it considerably more difficult to resolve the faint structures. To be able to properly evaluate the origins of the signal recorded in the imaging system it is important to characterise the nature of the PSF. This requires the full characterisation of the mirror surface over the whole range of spatial frequency. This is often summarised in terms of a low, mid and high spatial frequency error. In the case of the SXT the high and mid errors were evaluated to be 0.38 and 5.1nm respectfully. The measurements of the core part of the PSF and near wings were conducted at a testing facility located at the WSMR. These tests revealed that the level of the large-angle scatter for the SXT's mirrors were approximately two orders of magnitude smaller than that of the Skylab's SO-54 telescope (Tsuneta *et al.*, 1991). This may be attributed to the many advances which have been made, in surface fabrication and finishing methods, since the Skylab mirrors were created (Hoover, 1989). The level of this scatter although substantially reduced can still dominate the emission in the fainter regions such as coronal holes and the high latitude corona. Thus, evaluation of this scatter is crucial when measuring the signal in these faint regions. A complication when trying to estimate the contribution of this scattered light is that shorter wavelength light tends to scatter more than longer wavelength light. This wavelength dependence was investigated by Hara *et al.* (1992) who used the images of three over-exposed images of solar flares. These images are sometimes recorded accidentally (eg. when the spacecraft is passing through the SAA) and are usually dominated by the telescope-scattered light. The result of Hara's investigation was a scatter normalisation whose wavelength dependence goes as λ^{-1}. This is inconsistent with previous studies which predict that scattering due to random surface roughness the scatter level should vary as $(\lambda\vartheta)^{-2.}$, where λ and ϑ is the wavelength and scattering angle respectfully.

In this chapter an expression is derived to represent the level of scattered light in the SXT images. This is then compared with the levels determined from a series of flare observations. An investigation of the azimuthal variation of the scatter demonstrates that the halos are highly anisotropic. This is characterised empirically. The effect of scattered light on filter ratio temperatures is then illustrated.

3.1.1 Wavelength Dependence of Scattered Light

Understanding the wavelength dependence of the scattered light is necessary for extrapolating the calibration data to other wavelength ranges. Consequentially suitable scattered light levels may then be assigned to non-flaring lower temperature sources and observations made through different filters. In Hara's work this wavelength dependence was determined purely from the data. This left a large uncertainty in the result which was due principly to the limited data available. Ping and Van Speybroeck (1995) have stated that the general wavelength dependence of the scattered light on scattering angle, ϑ, goes as $(\lambda\vartheta)^{-2.}$ for random surface roughness.

This can be demonstrated using an expression derived by Michette (1988) who uses a method originally developed by Debye (1914) to determine the effect of surface roughness on the reflected intensity. The method assumes a crystalline surface but the resultant expression is cited as being applicable for all rough surfaces. Indeed, in a more complicated treatise on the subject of scattering from rough surfaces by Beckmann and Spizzichino (1963) a similar expression is derived:

$$\mathrm{I_r = I_i exp}\left[-\left(\frac{4\pi\sigma\sin\vartheta_\mathrm{A}}{\lambda}\right)^2\right] \tag{3.1}$$

where I_i and I_r are the incident and reflected intensities respectfully. σ is the rms surface roughness, ϑ_A the grazing angle and λ is the wavelength of the radiation. The total integrated scattered light $I_i - I_r$ would then be

$$\mathrm{I_{scat} = I_i}\left(1 - \mathbf{exp}\left[-\left(\frac{4\pi\sigma\sin\vartheta_\mathrm{A}}{\lambda}\right)^2\right]\right) \tag{3.2}$$

The ratio of the scattered light to the unscattered light then

$$\Omega_{psf} = \mathbf{exp}\left[\left(\frac{4\pi\sigma\sin\vartheta_\mathrm{A}}{\lambda}\right)^2\right] - 1 \tag{3.3}$$

or as in the case of the SXT where the grazing angles are small ($\sim 0.04 radians$) the small angle approximation for $\sin\vartheta_A$ may be used, and the exponential may be expanded :

$$\Omega_{psf} = \left(\frac{4\pi\sigma\vartheta_A}{\lambda}\right)^2 \tag{3.4}$$

Incorporating this into an expression similar to that derived by Hara gives:

$$I_{scat} = \alpha(4\pi\sigma\vartheta_A)^2(\lambda r)^{-2.} \tag{3.5}$$

or reconciling constants into α

$$I_{scat} = \alpha(\lambda r)^{-2.} \tag{3.6}$$

This expression is needed to extrapolate the observed scattered light characteristics reported here at flare wavelengths to wavelengths more typical of the quiescent regions of the corona. In the following sections the value of α is determined.

3.2 Analysis

3.2.1 Observational Characteristics of Telescope Scattered Light

In the usual mode of operation the SXT records a full frame image of the Sun every few minutes. When a solar flare occurs the wide band spectrometers detect the rise in the observed radiation and triggers the SXT to switch into a flare mode. In this mode Partial Frame Images (PFI) of the most intense source located on the solar disk are recorded with varying cadence. This mode of operation sometimes fails to be triggered when the spacecraft is in transit of the SAA. When this occurs the SXT instead records a normal image of the solar disk. These images are often dominated by the scattered light halo which subtends from an intense solar flare (*e.g.* figure 3.1). These images are used to evaluate the level of scattered light.

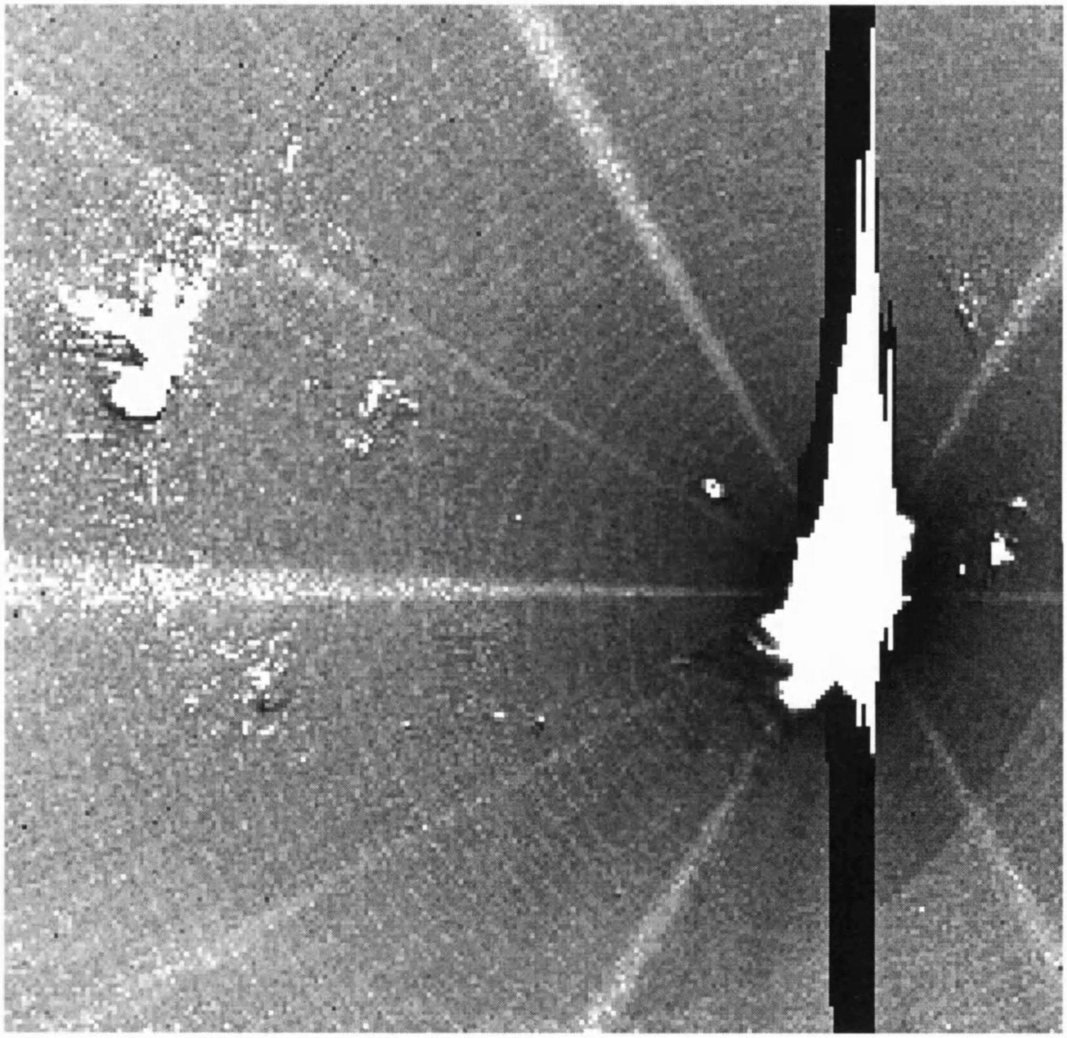

Figure 3.1: The domination of the scatter field by the scattered light surrounding the flare observed on the 6th September 1992 at 18:57UT. For the analysis of the scattered light alone a suitable image is selected for the background and removed. The feature that runs from the top to the bottom of the CCD is due to the saturation and overflow of charge in a CCD channel.

To remove the emission and scatter not related to the flaring region an image before the flare commenced is subtracted to leave an excellent image of the scattered light halo. It is clear that the scatter is anisotropic in that there is considerable variation azimuthly around the flare centroid. These features are caused by optical elements which lay along the optical bench and differences in the telescope's entrance aperture. The criss cross pattern which is also visible is generated by the filter support structure (mesh) which is present in all the X-ray analysis filters apart from the Be119. The radial variation of the scattered light for a segment (lower right hand corner of figure 3.1) of the halo is presented in figure 3.2 and behaves as r^{-2} (where r is the radial distance from the scattering centre in half resolution pixels).

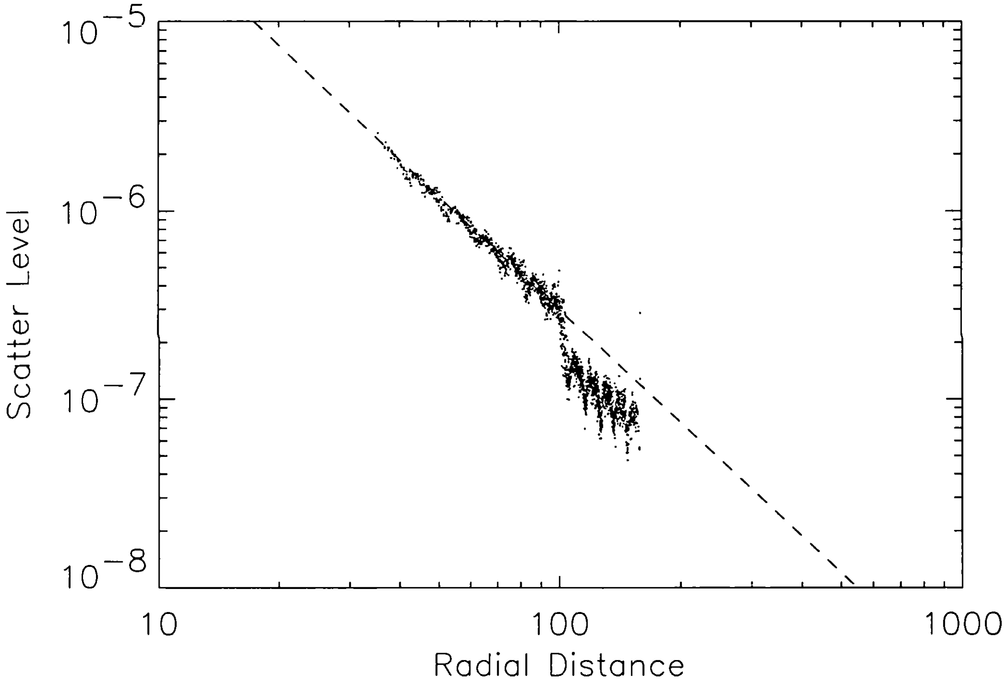

Figure 3.2: The radial variation in the level of telescope scattered light extracted from the 1992, September 6^{th} flare. The dashed line represents a power law with an index of -2. The slope of the index was left fixed at this value throughout the investigations of the azimuthal variation. This was neccessary as the fits obtained when this parameter was left free were found to pivot substantially around the mean. The decrease in the level of scattered light at a distance greater than 100 pixels is due to vignetting.

To investigate the azimuthal variation in the value of α (equation 3.6) the scattered light halo was fitted in degree steps azimuthally (in the plane of the CCD). Originally the power law index was left as a free parameter. However, the fitting process was found to be unstable with the power law index varying linearly with the logarithm of the normalisation. This was verified as being non-intrinsic by repeating the fit with an index fixed to different values. The linear relationship was reproducible so the power law index was left fixed at -2, which is consistent with previous work (*see* Ping, & Van Speybroeck, 1995). The results are illustrated in figure 3.3 with the fitted level normalised to the total PFI recorded counts. These were background-subtracted in a manner similar to that performed for the full frame image.

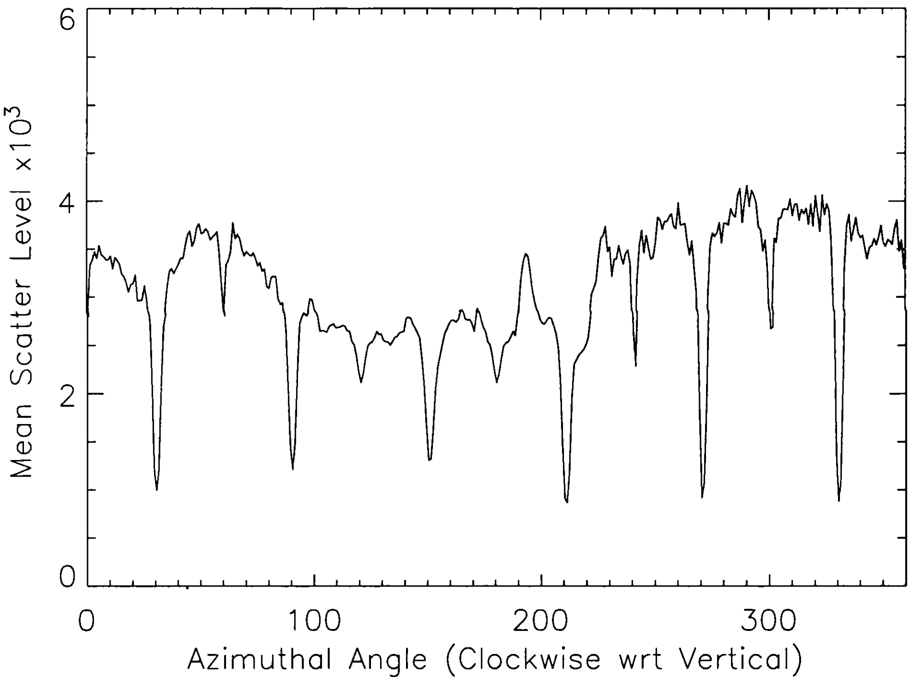

Figure 3.3: The variation of the normalisation determined with azimuth for the 1992, September 6th. This flare is located at a CCD location of 403, 228. ~16 minutes of arc off-axis (power law index fixed at -2.)

The variation of the scattered light level with azimuth illustrated in figure 3.3 is non negligible, particularly when compared to the mean level found by Hara of 2.4×10^{-3} (over 50% greater). The increased level is due mostly to the inclusion of the azimuthal variation and the background subtraction of the PFI emission. The process described above was repeated for the data presented in table 3.1. The azimuthal bin size was increased from 5 to 10 degrees for all of the flares in the table depending of the quality of the observed halos, with the exception of the flares observed on 27^{th} February 1992, and the 28^{th} June 1992. The azimuthal variation for these two events is illustrated in figures 3.4 and 3.5. It is clear that the azimuthal variation differs from flare to flare. This is due to vignetting which was first discussed in section 2.4.

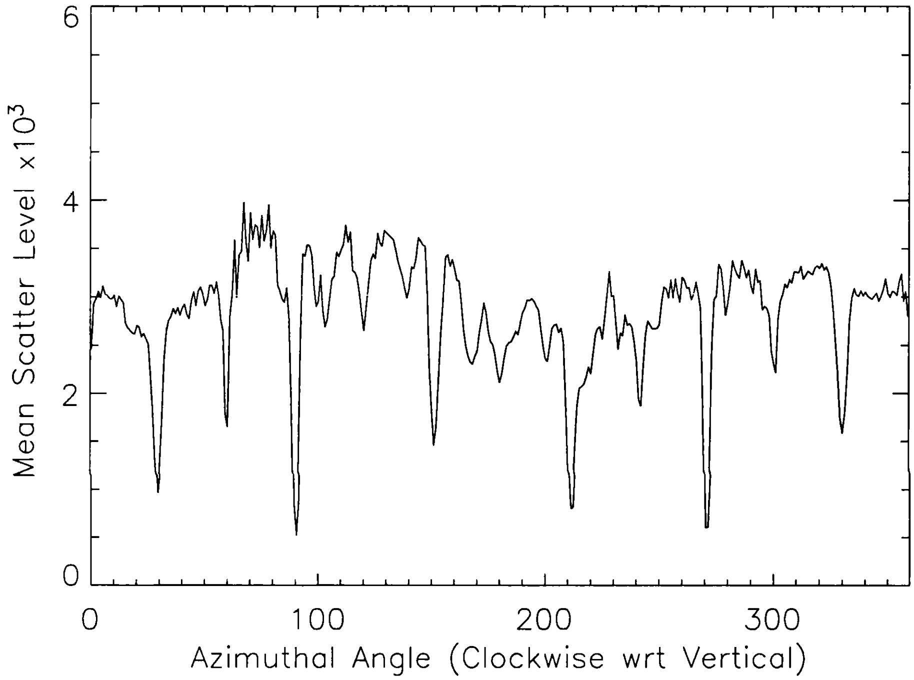

Figure 3.4: The extracted normalisation for the 27^{th} February 1992. This was evaluated using a fixed power law index of -2. Note the strong variation of the scatter-level about azimuth. This is due to the vignetting effect of the telescope (both obscured and optics). This flare is located close to the optical axis at CCD position 512,640

3.2.2 Wavelength Parameter

The accuracy in the determination of a mean wavelength for the observed solar flare emission is strongly dependent upon the validity of the isothermal assumption (*c.f* Section 2.2). Observations and analysis of solar flare emission has demonstrated the presence of super-hot plasma (Culhane, 1996).

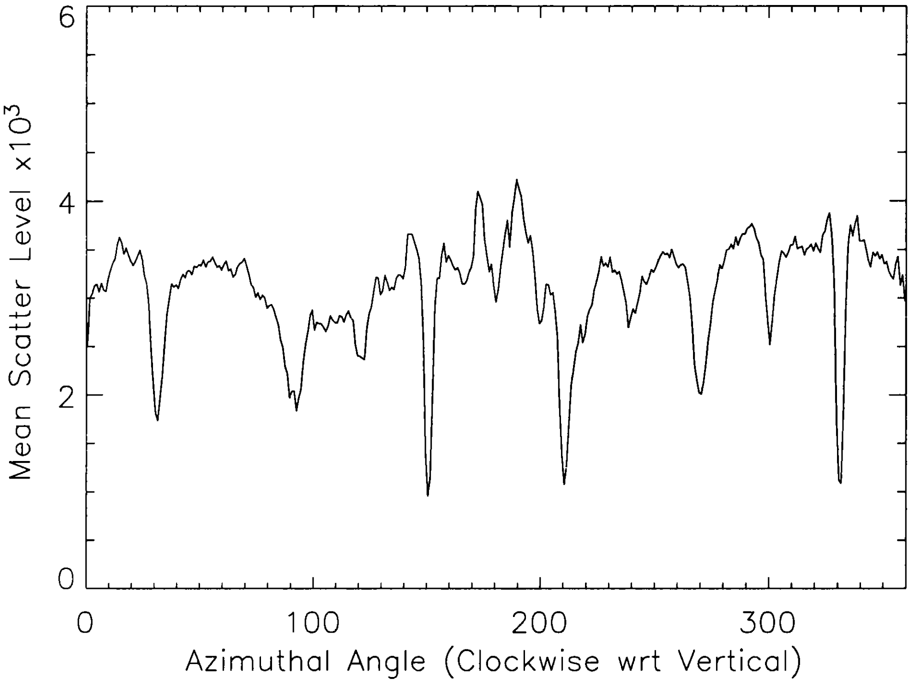

Figure 3.5: Same as figure 3.3 for the 28th June 1992 flare. This flare is located ~ 14 minutes of arc off-axis.

Date	Filter	Observation Time	Background exposure	Peak Goes Class
1992-Jun-9	Al.1	02:30:16	02:21:44	C5.2
1992-Sep-6	Al.1	18:57:06	18:30:00	X1.7
1992-Sep-6	Al.1	19:03:30	18:30:00	X1.7
1992-Jun-28	Al.1	05:32:52	04:36:52	X1.8
1992-Feb-27	Al.1	09:59:37	09:02:37	X3.3
1992-Oct-7	Al12	05:18:12	05:21:34	M3.1
1992-Oct-7	Al12	05:07:36	05:11:46	M3.1
1992-Oct-7	Al.1	05:07:40	05:14:56	M3.1

Table 3.1: The flares which were selected for the scatter level analysis

This superhot plasma is believed to originate close to the footpoints of the flares (Phillips, 1996) but represents a relatively small emission measure component. These findings confirm the findings of Bornmann and Strong (1988) who found that a single temperature component was inadequate to describe flare emission observed with the SMM spectrometer. Because the SXT takes broadband observations of flares no information is available to infer the emission measure distribution of the flaring plasma with temperature. This is because the observations are typically made through three filters which only provides sufficient information for a single component analysis of the flaring plasma. In this work the inferred temperature through the thinnest x-ray analysis filters has been used to represent the mean wavelength of the light observed through the thin filters. Similarly, the inferred temperature through the thickest filters has been used to represent the light observed through the thicker filter. This technique is fairly arbitrary, with no way of determining the error in the evaluation. The uncertainty in the mean wavelength of flare emission observed with the Yohkoh SXT can be estimated by considering all reasonable distributions of the plasma which are possible. As in the case of Bornmann and Strong a two component analysis is used. The intensity which is observed with the SXT (using equation 2.2) through each of a pair of observing filters may simply be expressed as

$$I_1 = \mathrm{F}_1(\mathrm{T}_{\mathrm{eC}}) \int \mathrm{N}^2_{\mathrm{eC}}\mathrm{dv} + \mathrm{F}_1(\mathrm{T}_{\mathrm{eH}}) \int N^2_{\mathbf{eH}}dv \tag{3.7}$$

and

$$4I_2 = \mathrm{F}_2(\mathrm{T}_{\mathrm{eC}}) \int \mathrm{N}^2_{\mathrm{eC}}\mathrm{dv} + \mathrm{F}_2(\mathrm{T}_{\mathrm{eH}}) \int N^2_{\mathbf{eH}}dv \tag{3.8}$$

Representing the emission measure ratio of the hot component to the cold component by em_C^H, and factoring this out leads to

$$em_1^2 = \frac{((\mathrm{F}_1(\mathrm{T}_{\mathrm{eC}}) - \left(\frac{\mathrm{I}_1}{\mathrm{I}_2}\right)\mathrm{F}_2(\mathrm{T}_{\mathrm{eC}}))}{(\left(\frac{I_1}{I_2}\right)\mathrm{F}_2(\mathrm{T}_{\mathrm{eH}}) - \mathrm{F}_1(\mathrm{T}_{\mathrm{eH}}))} \tag{3.9}$$

where the subscripts **C** and **H** denote the cold and hot component respectfully. Although there is not a unique solution to the equation, there does exist a continuous range of solutions. This is used to determine the best representation of the flare plasma in terms of the mean wavelength of the photons reaching the CCD.

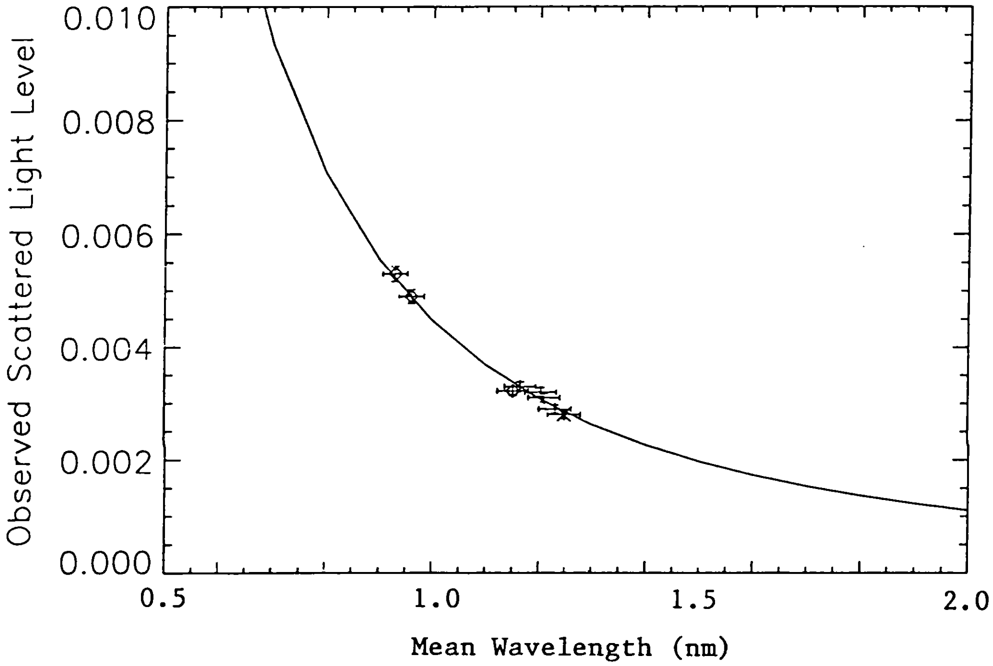

Figure 3.6: The resultant points and model for the scatter light normalisation. The error bars are representative of the statistical error.

3.2.3 Vignetting of Telescope Scattered light

From figures 3.1 and 3.3 it is evident that the scattered light halos are split into twelve segments (vignetted every 30 degrees). These raidal rays are produced by the sun shield which is illustrated in figure 3.7. This limits the SXT's aperture to prevent image degradation such as ghosting. This is located before the mirror assembly and so is actually vignetting the incoming light instead of the scattered light.

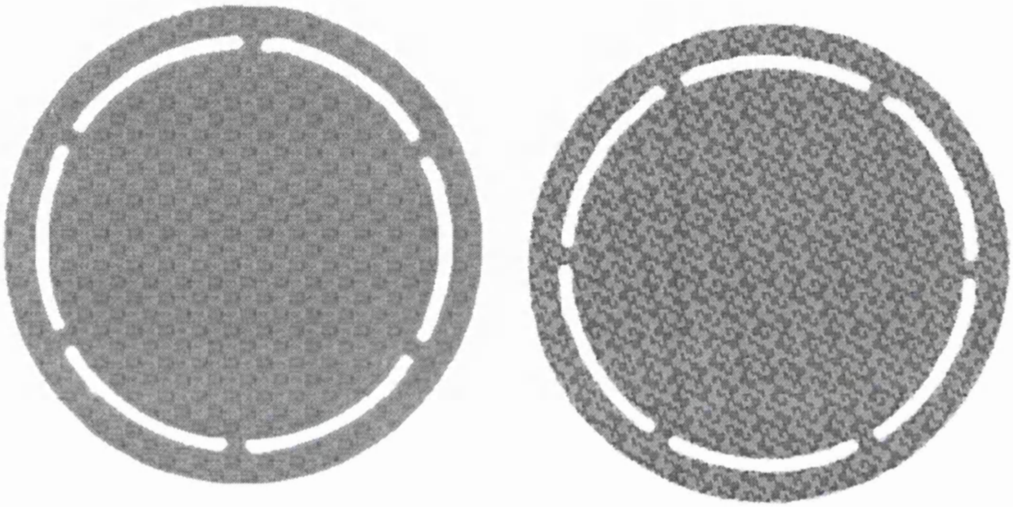

Figure 3.7: The SXT's sun-shield which limits the SXT's aperture to prevent image degradation such as ghosts forming. The effects of this are clearly visible in the scattered light halos as the radial cuts in the scatter halos

A region which is clearly affected by vignetting is far off-axis where a sudden dip in the level of scattered light is observed (see figure 3.2). This is most probably due to the effect of the aperture stops which prevent single reflections reaching the optical axis and thus also eliminate ghosting of the image. This is observed to be sharpest where the scatter source is located close to the vignette boundary. This illustrates a relationship between the source's location relative to the boundary and the amount of vignetting which is observed. On this basis the variation was investigated with respect to the distance of the source from the boundary (in the plane of the CCD). The result is illustrated in figure 3.8. There is a clear relationship which was found to be represented by the expression

$$\%_{vig} = 1 - \frac{\Gamma + 170}{512} \tag{3.10}$$

where Γ is the distance to the vignette boundary measured in half resolution pixels.

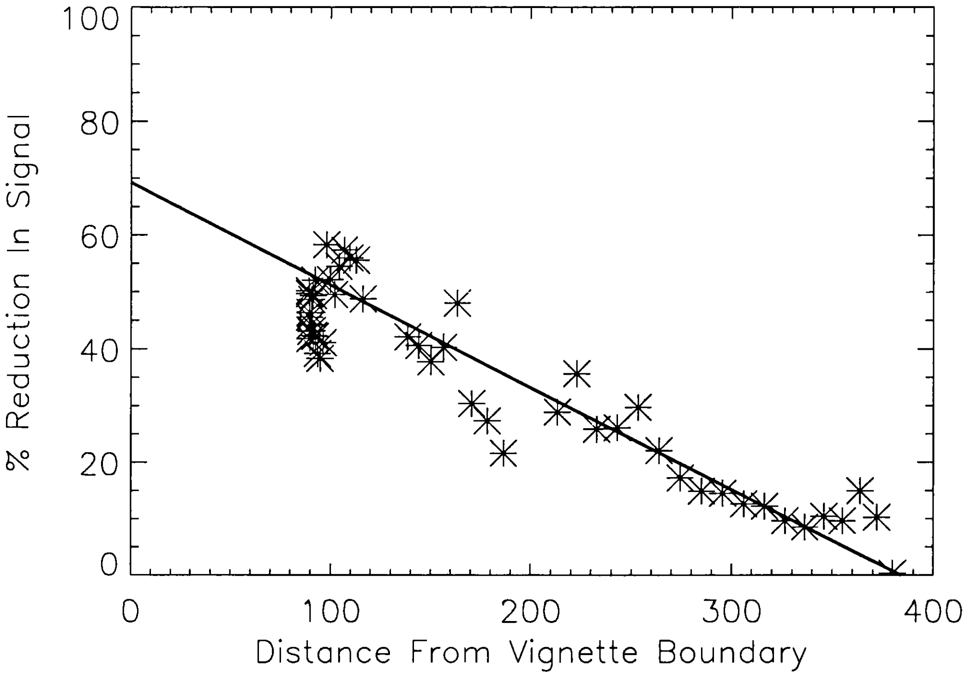

Figure 3.8: The variation of the percentage reduction in the signal observed to occur at the vignette boundary. The distance from the boundary is measured in half resolution pixels

From figures 3.3-3.5 it is event that the azimuthal variation of the scattered light varies with the source's position on the CCD as illustrated in figure 3.9. A comparison of the data for the different halos was also found to suggest a relationship between the scatter source position in relation to the vignette boundary expressed as:

$$\%_{vig} = 1 - \frac{\Gamma}{940} \tag{3.11}$$

Application of this to the scatter variation for the 1992, September 6^{th} flare is illustrated in figure 3.11. This function was also found to agree reasonably with the vignette function that was determined preflight. This

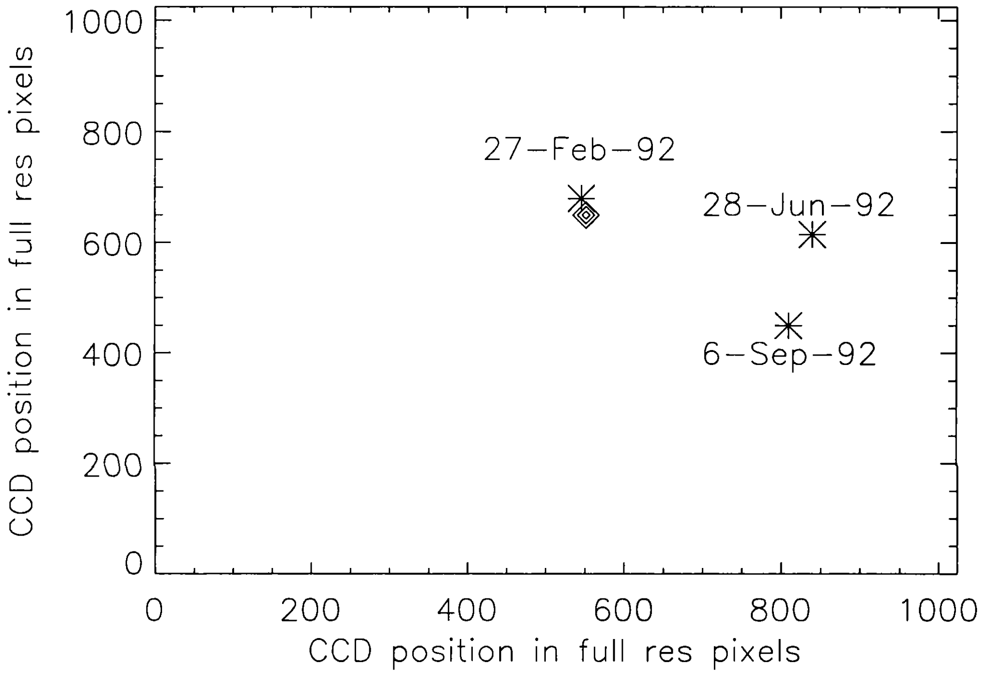

Figure 3.9: The positions of the scatter light halos on the CCD. These are used to investigate the azimuthal distribution of scattered light with position on the CCD. The optical axis determined prior to flight is indicated by the diamonds. The flare observed on the 27-Feb-92 is almost concentric with this axis and is used as the reference scatter source.

suggests the reason for the non-axi-symmetric distribution of the scattered light may also be due to vignetting.

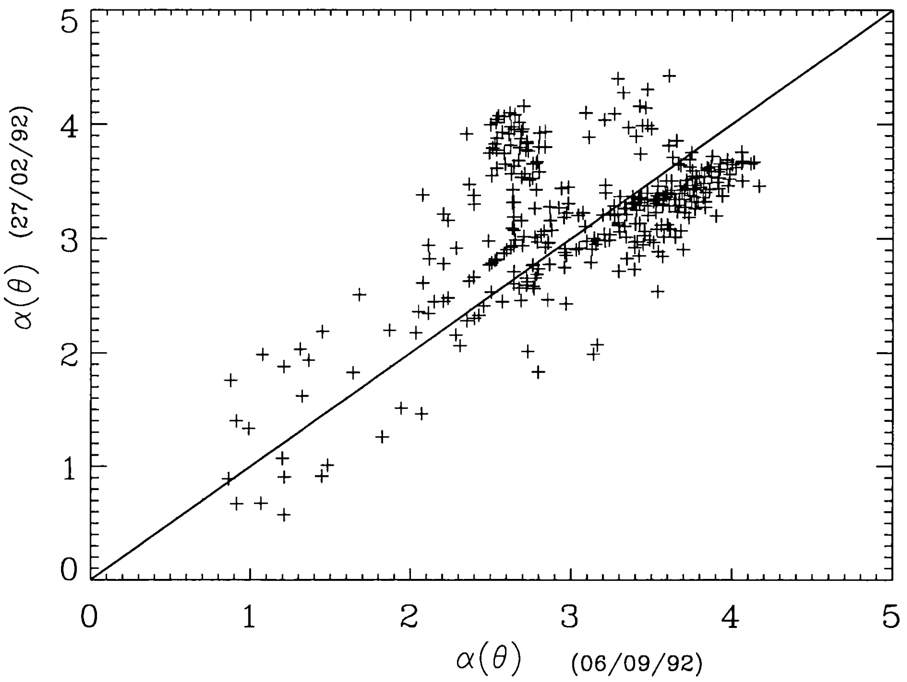

Figure 3.10: A comparison of the variation of the value of α ($\times 10^3$) with azimuthal angle ϑ (in the plane of the CCD) for the 1992, September 6th and 1992, February 27th (different positions on the CCD). The latter of these is located close to the optical axis.

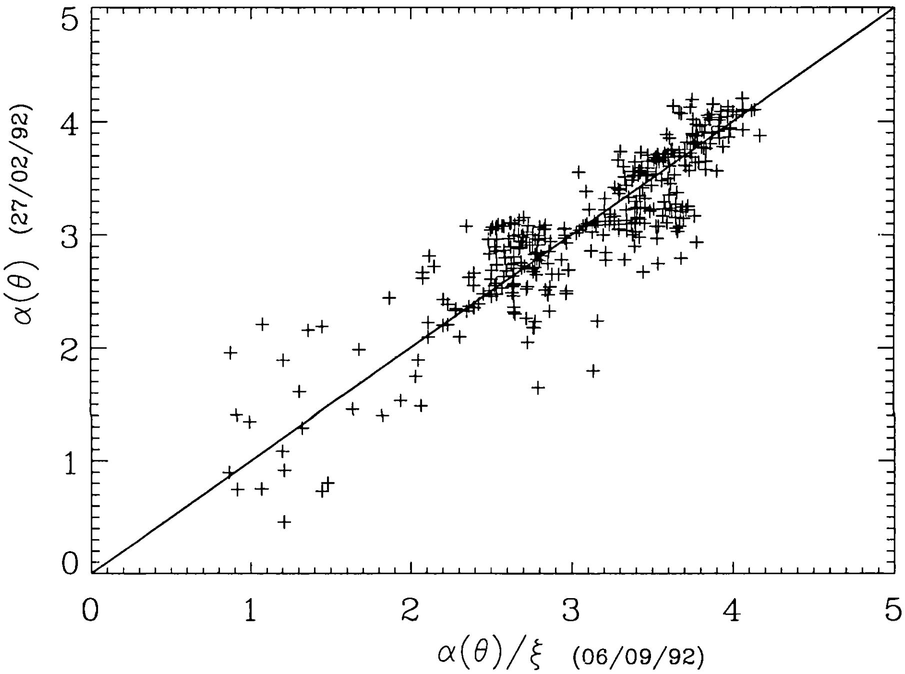

Figure 3.11: The same as figure 3.10 with the exception that a correction has been applied to the data for the vignetting (*c.f* equation 3.9)

3.3 Summary

The level of telescope-scattered light in the images obtained by the Yohkoh SXT has been evaluated for a series of flare observations. To enable use of this normalisation at wavelengths more typical of the quiescent corona a relationship has been obtained between the level of this scattered light and the wavelength of the incident radiation. This is found to be inversely dependent upon the wavelength to the second power. This can have the effect of biasing the temperature positively in faint coronal regions which surround bright sources. This is demonstrated for the two thinest SXT filters in figure 3.12 which illustrates the temperatures predicted from the ratio of the scattered light signals expected from sources of varying temperature.

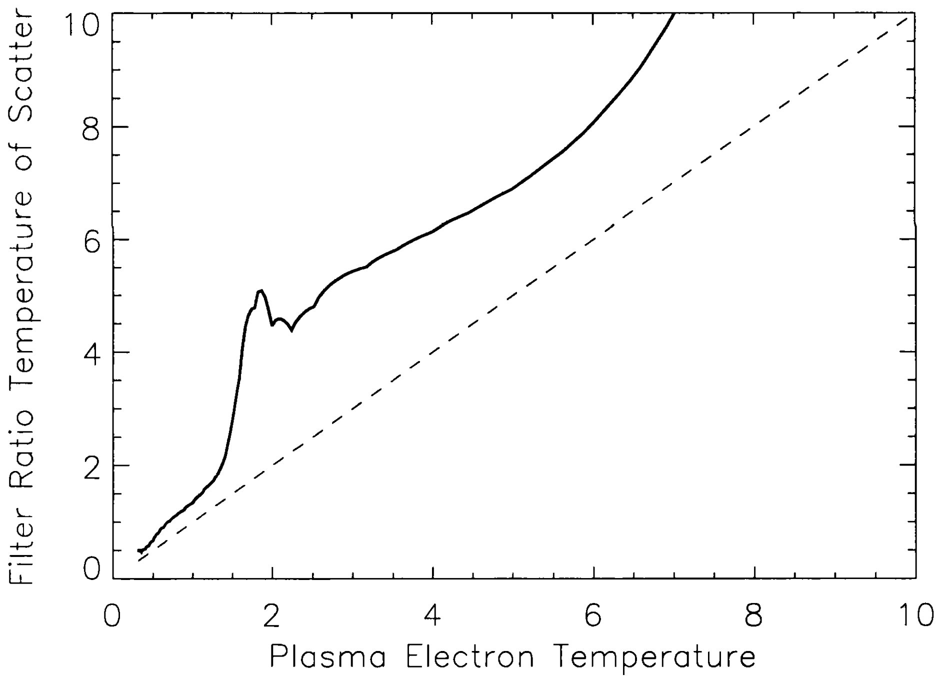

Figure 3.12: The effect of telescope scattered light on temperatures evaluated from the Yohkoh images.

As part of this work it was determined that the scattered light halos exhibit substantive azimuthal variation. The origin of this variation has been investigated empirically and appears to be due to a combination of effects ; the difference of the mirror surfaces optical properties, and/or the degree that the optical path is obscured. This variation has additionionaly been found to be dependent upon the location of the source with respect to the optical axis. This also appears to be consistent with the reduction expected due to vignetting. An empirical description of the scattered light is contained in equation (3.12).

$$I_{scat} = \alpha\eta(\lambda r)^{-2.} \tag{3.12}$$

Chapter 4

Plasma Parameters of a Polar Coronal Hole

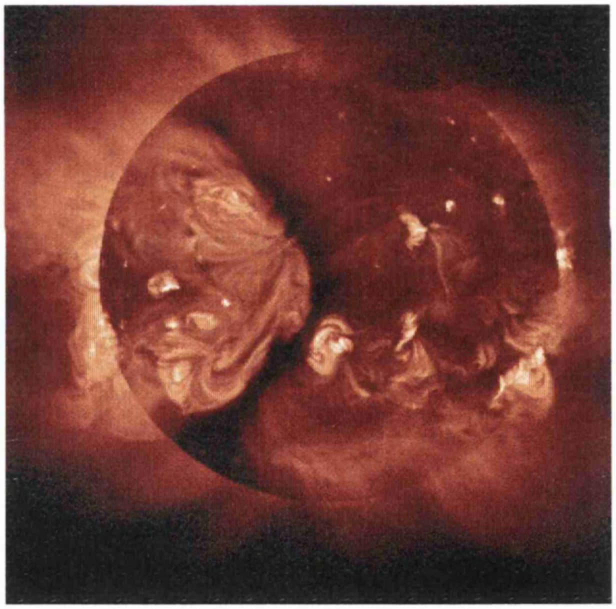

A chevron shaped coronal hole observed on the 1992, May 14^{th}, which is an extension of the southern coronal hole. The northern part can be seen to be separated from the north polar region by a arcade system of loops.

4.1 Introduction

Coronal holes are regions of open magnetic field along which the high speed solar wind flows. The plasma parameters within these regions have historically been demonstrated to be substantially reduced in comparison to the surrounding closed field corona outside of hole regions. The reduced parameters are conceptually consistent with energy being carried away by the extra energy sink : the solar wind. This has been confirmed by many authors who have modelled the outflow from the regions. The most fundamental and simple representation of the outflow is that due to the pressure gradient which is present in the low corona. This was first postulated by Parker (1958) before the direct observations of coronal holes had illustrated the presence of these open field regions. Parker's thermal solar wind model has a hot corona so that no energy deposition is required above the coronal base. However, from the first observations of the corona in the EUV regime it has been demonstrated that the temperature increase in the low corona is consistent with a positive extrapolation of the increase which commences above the photosphere. In this wavelength range the coronal holes appear to be similarly inhomogeneous as is the case for the closed field regions, with collimated plume like emission originating in strongly unipolar regions, and more general interplume emission. The open nature of the regions substantially reduces the complexity of the geometrical interpretation when modelling the regions. However, because there is an outflow from the regions a simple static interpretation as described in §1.2.2 is not possible and solutions of the equations governing the conservation of energy, momentum, and flow is required. This has been done by Withbroe (1988) who used the observational data obtained from coronal holes to fit his model.

Observationally the regions are most clear in soft X-rays where the emission is substantially depressed in comparison to the surrounding quiet region corona. This is the first indication that the plasma in these regions is of lower density and / or temperature. The previous observations of coronal holes with other spacecraft and techniques (Saito 1970, Munro & Withbroe 1972, Raymond & Doyle 1981, Habbal *et al.* 1993, *Galvin et al.*, 1984) have confirmed that the plasma is indeed cooler and less dense, with temperatures in the region of a million Kelvin as opposed to about double that for the quiet corona. These observations were made predominantly in the EUV regime, the lines of which typically have peak responses in that temperature region. Soft X-ray observations have a response which peaks in the millions of Kelvin regime ($\sim$ 6MK in the case of the SXT) which makes them useful for establishing the peak temperature of the plasma in the low corona. Indeed the observations of coronal holes with the Skylab soft X-ray telescope revealed an electron temperature in the region of 0.9-3MK (The high uncertainty was due to the dominance of the telescope scattered light within these regions). Earlier Yohkoh observations of coronal holes on the disk were reported by Hara *et al.* (1994). Temperature and emission measure were evaluated from observations of equatorial holes on the disk and the analysis included a correction for X-ray scattering by the telescope mirrors from sources of emission distributed over the rest of the solar surface. The temperatures reported for the individual coronal holes were in the range $1.8\text{-}2.4\mathrm{x}10^6$ K which is the same as that found for the nearby quiet corona. However, the electron density values were found to be about three times lower than that determined for the surrounding quiet region corona. The higher temperatures reported for the coronal holes have an imediate consequence for our understanding of solar wind outflow from the coronal holes. These being that the enhanced temperatures mean a higher base pressure, and thus higher observed velocity at the Earths orbit. The results of Hara would thus lead us to the conclusion, that there is a reduced requirement for non-thermal energy sources to further accelerate the solar wind.

To avoid the possibility of any structures outside the coronal hole contaminating the observed coronal hole emission, Hara *et al.* (1994) selected coronal holes located at the centre of the solar disk. A problem in using this technique is that the expected signal (assuming spherically symmetric emission) will be at a minimum at the centre of the solar disk. Additionally, the observation is closest to the other major source of contamination ; namely telescope scattered light from the bright active region corona. The optimum location for observing coronal hole emission (if the possibility of contribution from other non-coronal hole structures can be excluded) is thus in a polar region. Making an observation across the polar limb has the additional benefit that the limb brightening which is expected provides a characteristic increase of the observed signal as the limb is crossed. This is due to the effective doubling of the observer's line of sight above the limb. This could be used to estimate the intrinsic signal for the coronal hole regions in the abscence of suitable background corrections.

Data have been selected from a time period when Yohkoh observations obtained over a solar rotation indicated the north polar hole region to be essentially free of any contamination. However, it is still necessary to assess the importance of any possible contribution from high latitude coronal structures which surround the coronal hole and lie along the line of sight (*c.f.* figure 4.1). This has been done here by using the fact that the emission above the solar limb falls off exponentially. This then allows the emission gradient measured at the coronal hole boundary to be extrapolated into the coronal hole region to estimate the contribution (if any) to the observed coronal hole from foreground or background coronal structures.

In this work the observation of a north-polar coronal hole on 1992, October 3 is described. A coronal hole region that is essentially free of contamination from surrounding (non coronal hole) structures has been selected, and its boundary delineated. The X-ray flux expected from a coronal hole based on the previous empirical models of Withbroe, (1988) has been calculated. The calculated intensities are compared with observational data for which the level of scattering by the telescope PSF has been carefully assessed. Finally the results of this comparison are used to estimate the plasma properties for the coronal hole.

4.2 Observations

The observations consist of a sequence of five image pairs taken between 02:22 UT to 17:01 UT on the 3^{rd} October 1992, with exposure times of 15.1s through the Al and Al/Mg/Mn filters. A typical image of the observed region is shown in figure 4.2. These data are carefully aligned and corrected for the effects of CCD saturation, dark noise and particle hits. Since the signal is weak, the data are summed to produce a total exposure of 75.5

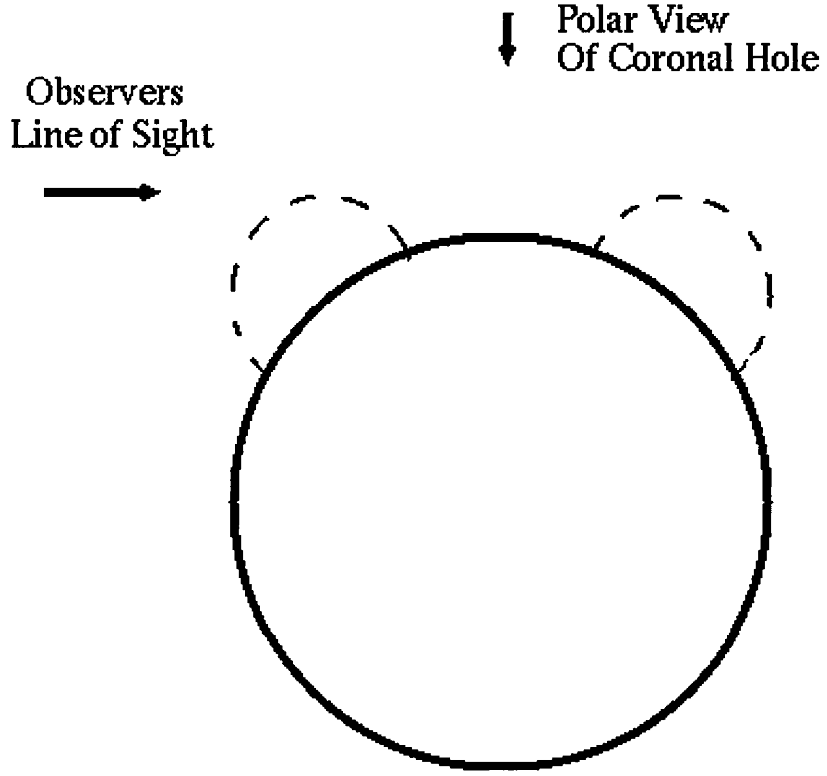

Figure 4.1: The observers line of sight through the coronal hole region. The dashed lines illustrate the possible contribution of surrounding quiet coronal structures along the line of sight. This possibility is reduced substantially by selecting a coronal hole region which is extended along the line of sight

seconds in each filter. The signal obtained through the central portion of the coronal hole region of the summed data is illustrated in figure 4.3. In order to reduce the noise the coronal hole signal is summed into circumferential arcs of constant distance from disk centre and of width 5 arc sec (i.e. one SXT half-resolution pixel).

As was pointed out by Mariska (1978) the polar regions may be subject to the inclusion of foreground or background quiet coronal structures along any line of sight through the coronal hole. Such contributions must be minimised by careful selection of the data. The northern polar coronal hole region, observed on 1992 October 3, appeared as a sector of low emission between the large scale structures that mark the high latitude activity zones on either side of the pole. These structures are apparent in the synoptic display which covers the period before the observation (see figure 4.4). The data when observed in movie format over a long period, suggest that the structures do not extend into the line of sight. Hence the coronal hole sector chosen for this analysis appears to be clear of any emission from these high latitude structures.

In the work of Mariska (1978) an emission measure analysis was used to model the observed emission through a series of EUV emission lines. The derived emission measure distribution with temperature suggested significantly hotter material lay along the same line of sight. This material was attributed to the contribution of quiet coronal structures located both in front of and behind the coronal hole. The intensity observed in the Si **XII** $\lambda 52.1nm$ emission line, (temperature of peak formation $\sim$ 2 MK) was used to construct a model representation of this quiet coronal material, and to estimate the emission gradients for the other (cooler) emission lines, which would be attributed to this 'quiet coronal material'.

Since the SXT is a broad band instrument, it is not possible to use the same analysis technique. Instead the position of the coronal hole boundary at the coronal base has been estimated, and the emission gradient assessed at this boundary. The measured emission gradient was then extrapolated into the coronal hole region to estimate the contribution from any quiet coronal structure located in front or behind the coronal region. Figure 4.5

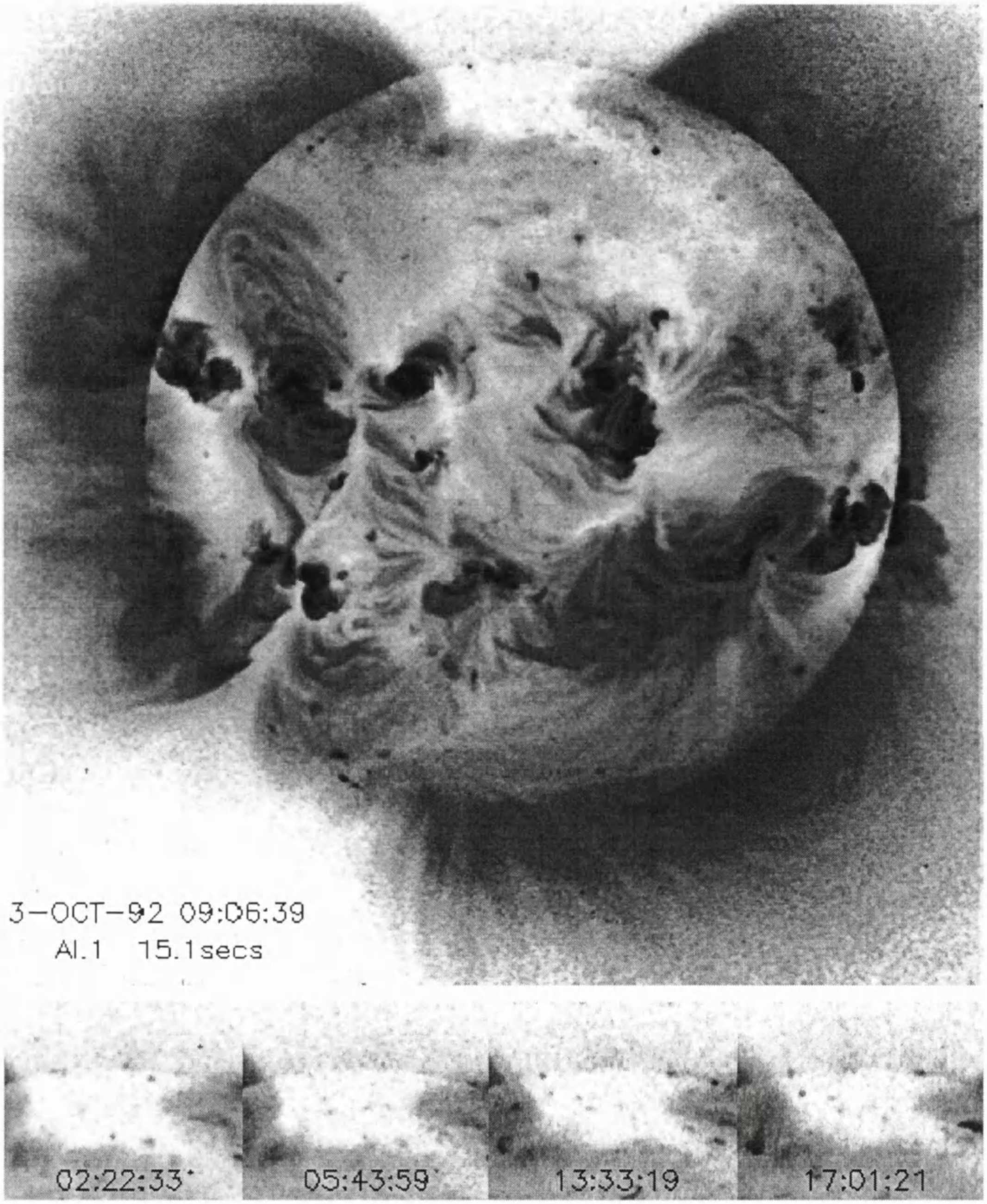

Figure 4.2: The coronal hole region observed on 1992 October 3, which appears as a sector of low emission between the large scale magnetically closed structures that mark the high latitude activity zones on either side of the pole. The sub-figures at the base of the illustrate the stability of the coronal hole over the period which the emission was averaged.

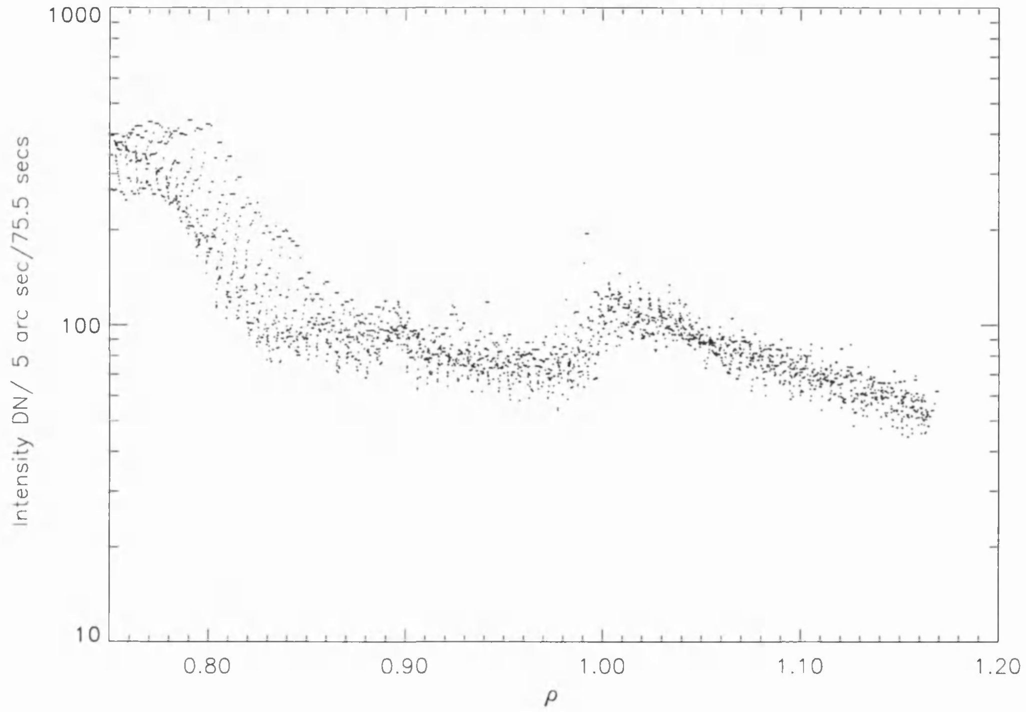

Figure 4.3: The spatially unaveraged intensity extracted from the coronal hole region plotted as a function of ρ, the distance from disk centre in solar radius.

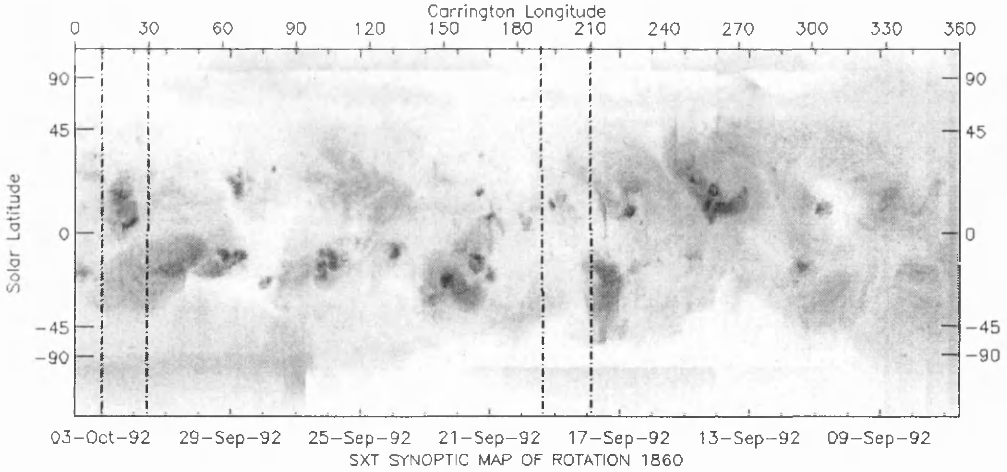

Figure 4.4: Synoptic image for the period of October 1992. The emission observed above the northern limb of the synoptic map between longitude 30^o and 180^o is attributed to the transit of the magnetically closed high latitude activity zones though the central meridian, and thus the line of sight. It is clear that these zones do not contribute to the coronal hole signal for the observation. The coronal hole region appearing as a 'valley of emission" between these zones.

illustrates the polar extent of the coronal hole along with the emission gradients for the boundary regions along the line of sight on October 3 and October 17. The gradients observed at the boundary are consistent with the qualitative results discussed above and suggest that the signal from the polar coronal hole is essentially free from foreground or background emission from structures outside the hole.

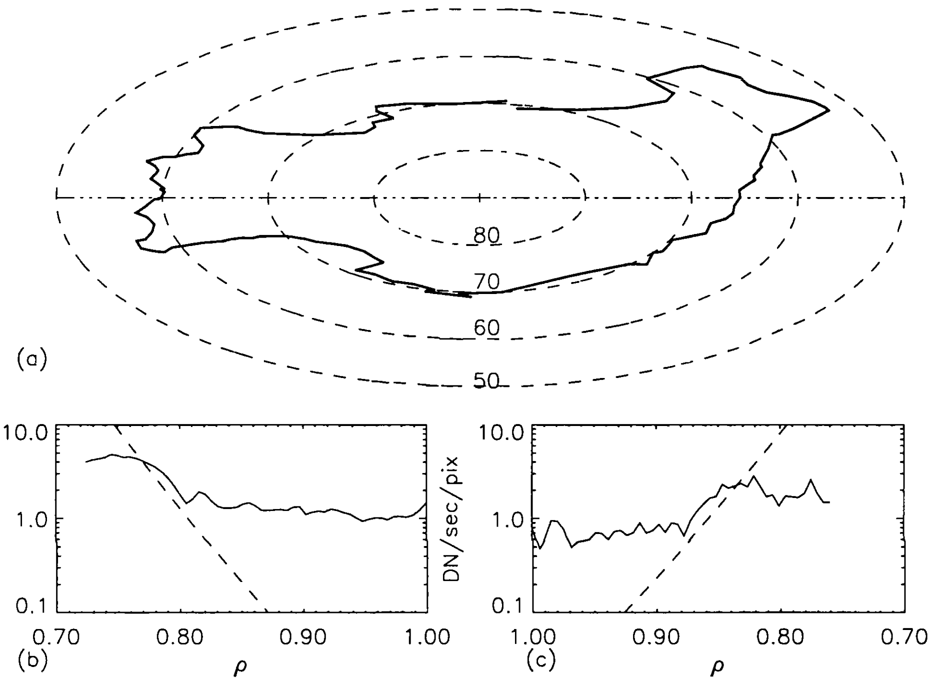

Figure 4.5: (a) A polar view of the coronal hole boundary, The line of sight through the coronal hole observed on October 3, runs left-right. (dash-dot line). Lines of constant latitude are indicated by the dashed lines. (b) The emission gradient observed at the coronal hole boundary on 1992 October 3. (c) The emission gradient observed at the coronal hole boundary on 1992 October 17.

Coronal holes are regions of very faint intrinsic emission in an otherwise bright X-ray corona. It is therefore necessary to correct for the effects of X-rays scattered by the telescope surfaces from other sources on the Sun. Since the bright active region emission comes predominantly from latitudes $< | 35^o |$, polar coronal holes are usually least affected. The telescope's large angle point spread function (Chapter 2) is used to evaluate the contribution of scattered X-rays from sources on the disk to the coronal hole signal.

4.3 Limb Brightening and Temperature Analysis

The temperature as a function of height in the solar corona is an indication of the line of sight integrated energy content. The flow, momentum, and energy of each plasma element along the line of sight must be conserved. These conservation laws are represented by the following equations

$$(N_e + N_i)\mu V A(r) = \gamma \tag{4.1}$$

$$(N_e + N_i)\mu V \frac{\mathrm{dV}}{\mathrm{dr}} = -\frac{\mathrm{dp}}{\mathrm{dr}} - (N_e + N_i)\mu \frac{GM_\odot}{r^2} - \frac{\mathrm{d}}{\mathrm{d}r}\left\langle \frac{\delta B^2}{8\pi} \right\rangle \tag{4.2}$$

$$\Phi(\mathrm{T})\mathrm{N_e N_p} + \frac{1}{A(r)}\frac{\mathrm{d}}{\mathrm{dr}}\left(A(r)[\kappa \mathrm{T}^{2.5}\frac{\mathrm{dT}}{\mathrm{dr}} + F_m + F_A] + \gamma\left[\frac{2.5kT}{\mu} + \frac{V^2}{2} - \frac{GM_\odot}{r}\right]\right) = 0. \tag{4.3}$$

where γ represents the mass flux, N_e and N_i are the electron and ion number densities, T is the temperature, μ the effective particle mass. For the Sun where the helium abundance is $\sim$ 10%, μ has a value of 1.04×10^{-24}g. A represents flow tube cross-sectional area, P the plasma pressure, B is the magnetic field strength, V the plasma flow velocity, Φ is the radiative loss coefficient, G is the gravitational constant, $M_\odot$ is the solar mass, F_c is the conductive flux, F_m is the mechanical energy flux, and F_A is the Alfven wave energy flux. A fully ionised hydrogen plasma with 10% Helium was assumed. Hence, the ratio of specific heats was taken as 5/3.

Withbroe (1988) used these conservation laws in conjunction with the prior empirical observational data from coronal holes, to obtain the variation of heating with radial distance. This was performed by iteratively solving conservation equations (4.1)-(4.3) whilst using just four adjustable parameters ; the base mechanical energy flux F_{mo} and its dissipation scale length L_h, the area expansion factor A(r) and the energy flux of Alfven waves F_A. The fits were performed using an initial radial density structure which was obtained from the white light observations (Saito 1970) and supplemented in the lower corona by values obtained by using ratios of EUV emission line intensities. The mechanical energy flux was represented by the following equation

$$F_m(r) = \frac{F_{mo}}{A(r)} e^{\frac{(R_\odot - r)}{L_h}} \tag{4.4}$$

where $R_\odot$ is the solar radius. The Alfven wave energy flux was represented by

$$F_A = \epsilon(V_A + 1.5V) \tag{4.5}$$

where V_A is the Alfven speed. Only solutions which became supersonic with T(r) approaching 0 at large distances were selected. The model parameters found are presented in table 4.1. The variation of electron temperture and density for the polar coronal hole at solar minimum and maximum are shown in figure 4.6.

Parameter	Coronal Hole (Maximum)	Coronal Hole (Minimum)	Quiet Corona
F_m (ergs cm^{-2} s^{-1})	$10^{5.62}$	$10^{5.49}$	$10^{5.9}$
L_h ($R_\odot$)	0.38	0.77	0.25
F_A (ergs cm^{-2} s^{-1})	$10^{5.3}$	$10^{5.18}$	0

Table 4.1: Model parameters from the Withbroe fits for the quiet corona

Based on the model data plotted in figure 4.6, the emission which would be registered from a polar coronal hole by the Yohkoh SXT can be calculated by integrating equation (4.6) over λ and θ along the line of sight for each value of ρ

$$I(\rho) = \zeta(\rho) \int_\lambda \int_\theta \psi(\lambda, T_e(\theta,\rho))\nu_i(\lambda) N_e(\theta,\rho)^2 \rho \cos(\theta) d\lambda d\theta \tag{4.6}$$

where ρ is the distance from disk centre and is measured in units of solar radius. N_e and T_e are the electron density and temperature and $\psi(\lambda, T_e)$ is the power emitted by a plasma of temperature T_e at wavelength λ (Mewe *et al.*, 1985, 86). The term $\nu_i(\lambda)$ represents the response of the SXT for filter i and ζ is the telescope vignetting function (Tsuneta et al., 1991). The predicted I(ρ) is plotted against ρ in figure 4.7 for the most sensitive Yohkoh filter (Al.1) and exhibits notable limb brightening.

The averaged signal extracted from the data is plotted as a function of distance from the disk centre, ρ, in figure 4.9. The individual points include the contribution of the scattered radiation while the calculated scattered signal is indicated by the dash-dot line. The solid line represents the sum of the radial intensity profile calculated from the solar maximum model of

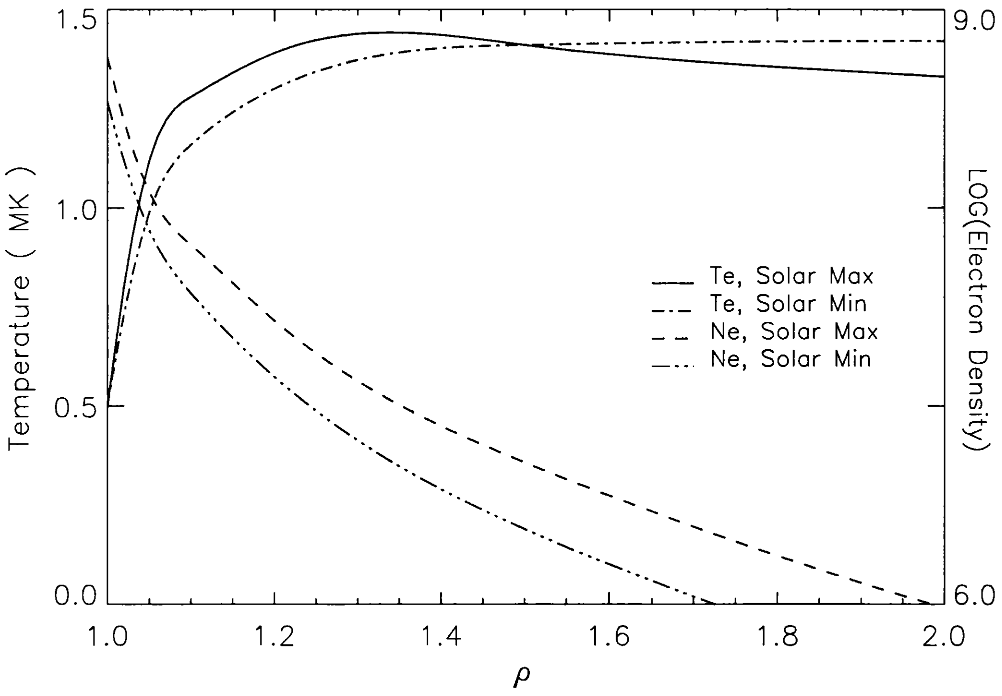

Figure 4.6: The radial variation of temperature and density for the polar coronal hole models of Withbroe (1988).

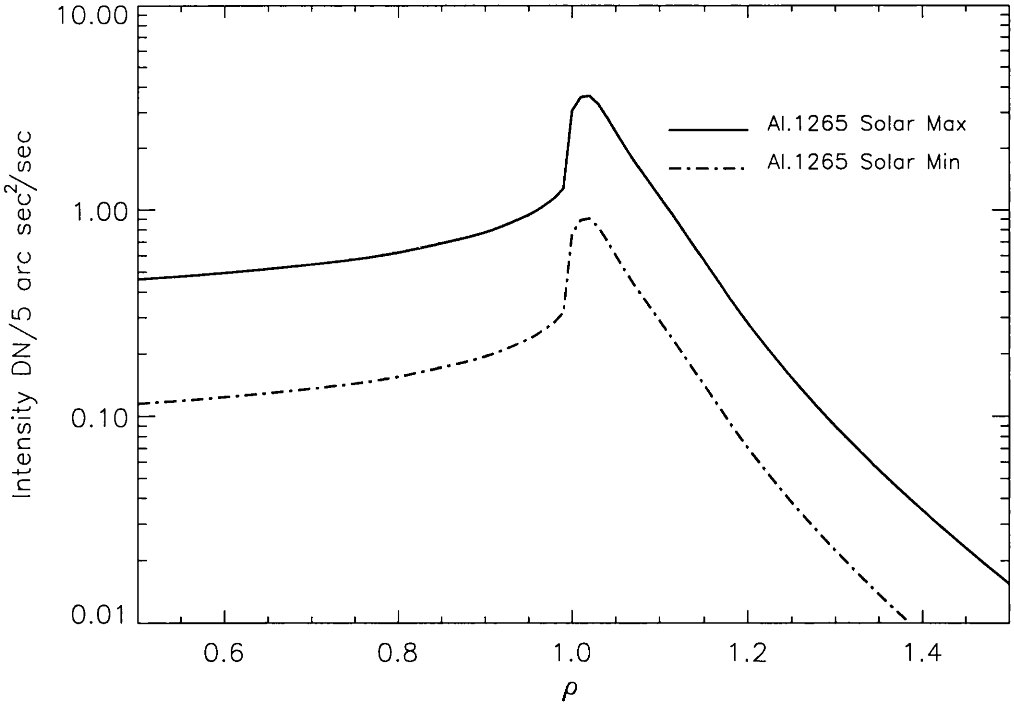

Figure 4.7: The limb brightening constructed by numerically integrating the line of sight integral (equation 4.6) using the parameters displayed in figure 4.6.

Withbroe (1988) as described above plus the scattered and boundary contributions. This solid line has been normalised to the data points by finding the best fit coronal radial density profile. The appropriate density is found to be approximately half that for the solar maximum model of Withbroe (1988), varying from 2.85×10^{8} cm^{-3} at the coronal base to 4.93×10^{5} cm^{-3} at 2 $R_{\odot}$.

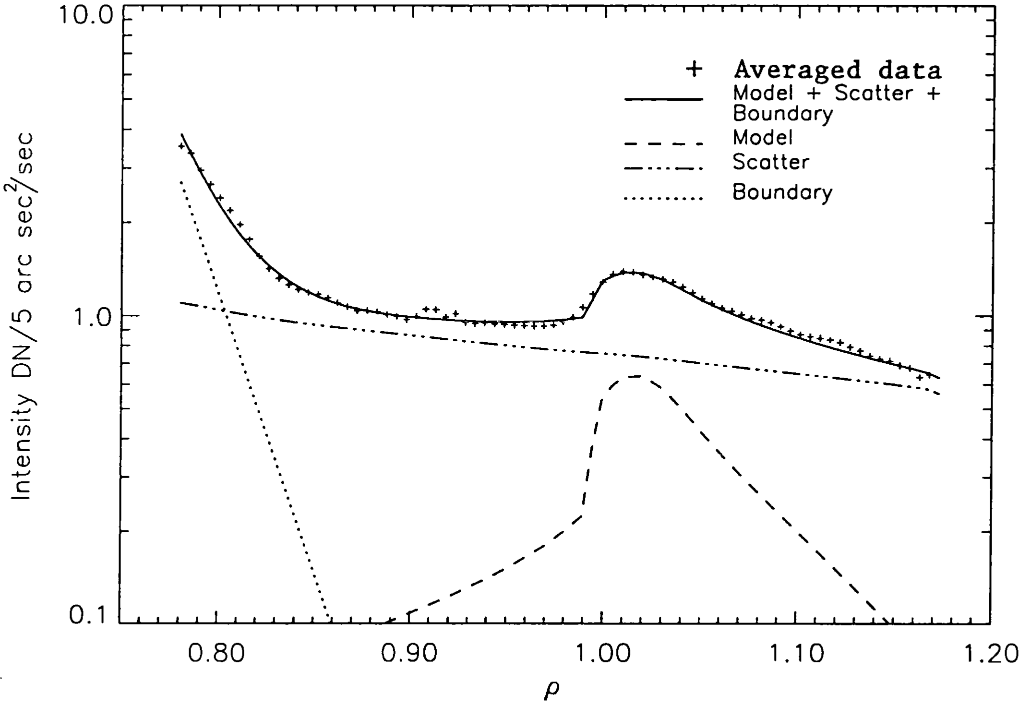

Figure 4.8: The average signal observed through the northern coronal hole (points), and the three components which compose the observed emission for the thin Al filter.

Since significant signals are obtained in two different filter passbands up to a height of R~1.18 $R_{\odot}$, line of sight values of T_e may be obtained by taking the ratio of the signals (Maxson & Vaiana. 1977; Hara et al. 1992). Withbroe's models predict temperature as a function of height. However the plasma is optically thin, so the signal registered by the filter/CCD combination during any SXT observation will reach the instrument from along lines of sight which include material at a range of heights and temperatures. In order to compare the observed T_e values with those from the model, weighted average values of temperature such as would be registered by the SXT have been calculated from the solar maximum model of Withbroe (1988). Here equation (4.5) is used to predict $I(\rho)$ for each filter and line of sight. The ratio of these predicted signals are used to derive a filter ratio temperature expected for each line of sight.

The solid line in figure 4.9 shows these predicted values over the observed height range while the model values are also plotted for comparison. The filter ratio method was used to make four estimates of T_e for the height range $0.9 < \rho < 1.2$. Although the statistical errors are large due to the faintness of the emission and the effect of scattering by the telescope, the data points are in reasonable agreement with the predictions of both the solar maximum and minimum models. In addition, a detailed analysis of ionic charge composition data obtained at high heliographic latitude from the SWICS instrument on Ulysses by Ko *et al.* (1997) has allowed the determination of the temperatures at which the relative ion stage populations "freeze-in" due to the effective cessation of ionisation and recombination interactions between electrons and ions in the solar wind. Consideration of data for a range of elements constrains the location and value of the maximum in T_e to 1.5 ± 0.5 MK at 1.4 ± 0.1 $R_\odot$. The data point from this work is also shown in figure 4.9 and though slightly higher than the model values, it can together with the Yohkoh observations reported here, constrain the electron temperature values in the inner high speed solar wind flow.

Ko *et al.* (1997) have also ruled out models where temperature decreases monotonically from the base of the corona. The same technique used to compare the Withbroe model with the observations, may be used to compare this model also. For this a power law decrease in temperature with ρ is combined with the solar minimum density profile. The power law dependence for temperature is given by (Owocki *et al.*, 1983) as

$$T(\rho) = T_o(\rho)^{-2/7} \tag{4.7}$$

where T_o, the temperature at the base of the corona was set to 2.0 MK. The resulting SXT signal is shown plotted against ρ in figure 4.10 along with the prediction of Withbroe's solar minimum model for comparison. It is clear that the decreasing temperature assumption predicts intensities which are much larger than observed (figure 4.9), are more strongly peaked at the limb and fall off more steeply with increasing ρ. Thus a model with monotonically decreasing temperature and a value of base temperature similar to

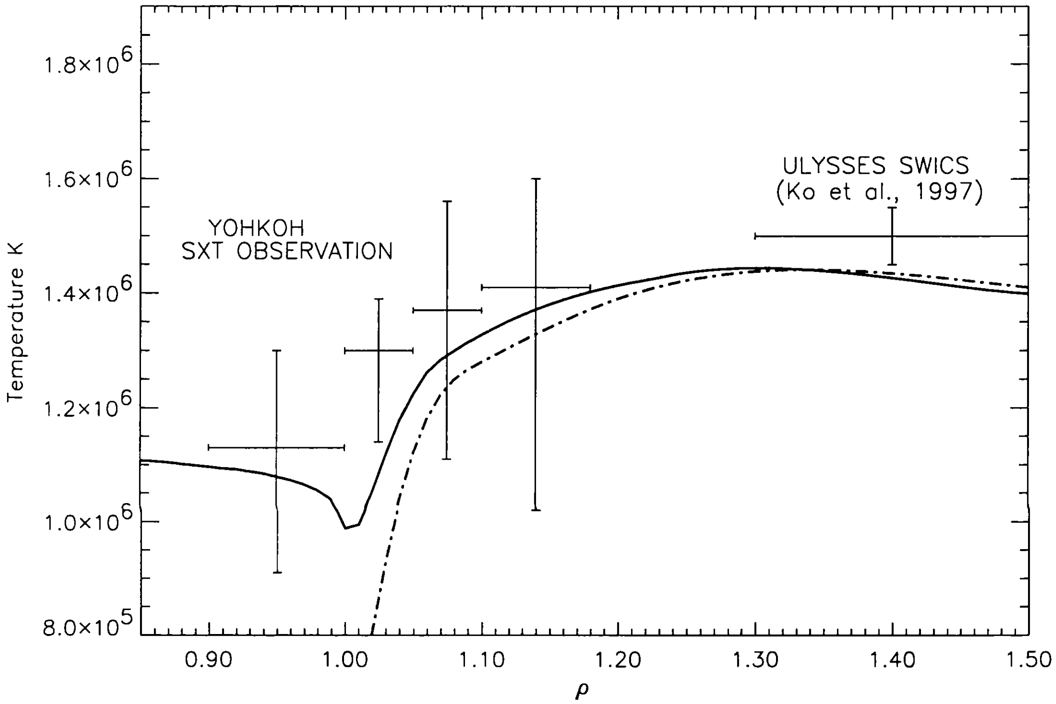

Figure 4.9: Filter ratio temperatures for the coronal hole region. Also shown are the values from the solar maximum model of Withbroe (*dash-dotted line*) The solid line represents the effective line-of-sight temperatures that would be expected to be seen with the SXT from the Withbroe model. The *Ulysses* **SWICS** point was obtained by Ko *et al.* (1997) from an analysis of ion species concentrations when *Ulysses* was at high southern helio-latitudes.

that found by Hara *et al.* (1994) for coronal holes on the disk, would appear to be ruled out.

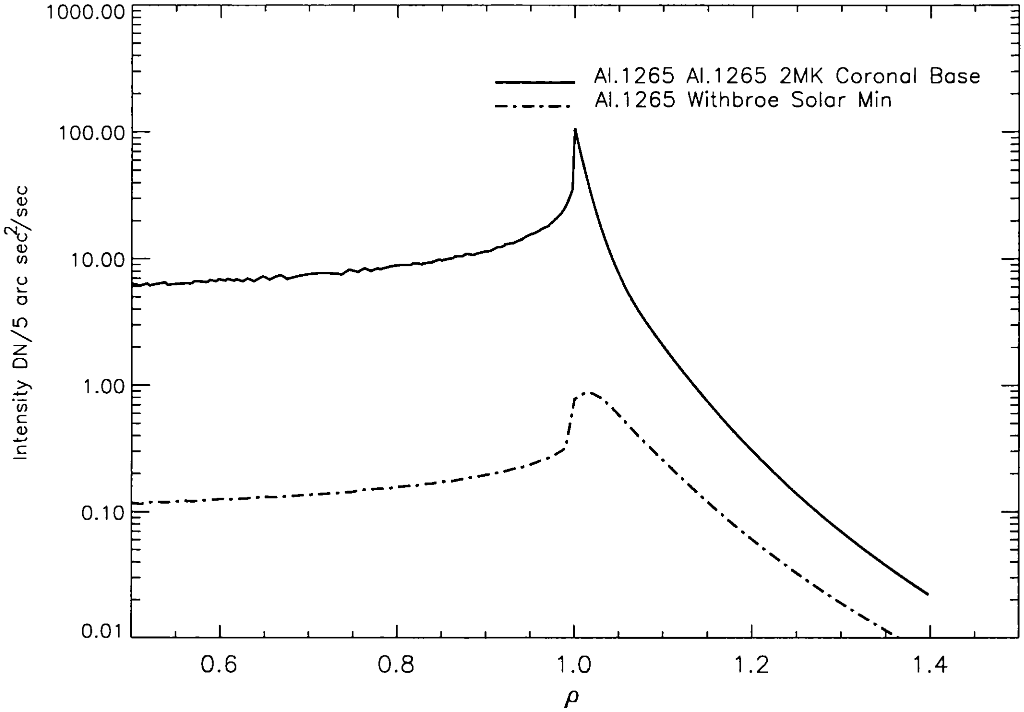

Figure 4.10: The response of the SXT to a solar wind with temperature decreasing monotonically from a value of 2 MK at the base of the corona. Predictions of the Withbroe model are also shown again for comparison. Both calculations use solar minimum density profiles.

4.4 Discussion

Observations of a north polar coronal hole have been presented which were made on 1992 October 3. The X-ray output was essentially free of contamination from the emission normally attributed to the magnetically closed high latitude structures. The limb brightening observed at the polar limb was found to agree well with the Withbroe (1988) model, but with a reduced density profile. The ratios of X-ray signals obtained from two different filters have been used to estimate electron temperature as a function of height. When appropriate allowance has been made for the effect of material at different temperatures along the telescope line of sight, the measured T_e values are in reasonable agreement with those predicted by the Withbroe model. The measured temperatures are also consistent with a maximum value of 1.5 MK at 1.4 $R_\odot$ estimated from "frozen-in" ionisation stage population concentrations measured by Ulysses at a distance of 2 A.U. and at high heliographic latitude.

Consistency with Withbroe's model for a polar hole at either solar maximum or minimum implies electron temperatures > 1 MK at heights above 1.03 $R_\odot$ with a peak value of 1.45 MK at 1.4 $R_\odot$. However the data presented in figures 4.9 and 4.9 can not in fact allow us to discriminate between these two models as far as temperature is concerned. Habbal *et al.* (1993) in an extensive review of coronal hole temperatures, suggest average values < 1.3 MK at heights < 1.6 $R_\odot$. The present observations tend to support slightly higher temperatures than these, although the restriction to X-ray wavelengths of $\lambda <$ 4.5nm might be expected to cause some bias towards higher temperatures in the measurements made close to the limb. It is clear that a model in which temperature falls monotonically from a value of 2.0 MK at the base of the coronal hole due to the dominance of thermal conductive flux does not fit the observations.

Chapter 5

Temperature Structure of The Diffuse Solar Corona

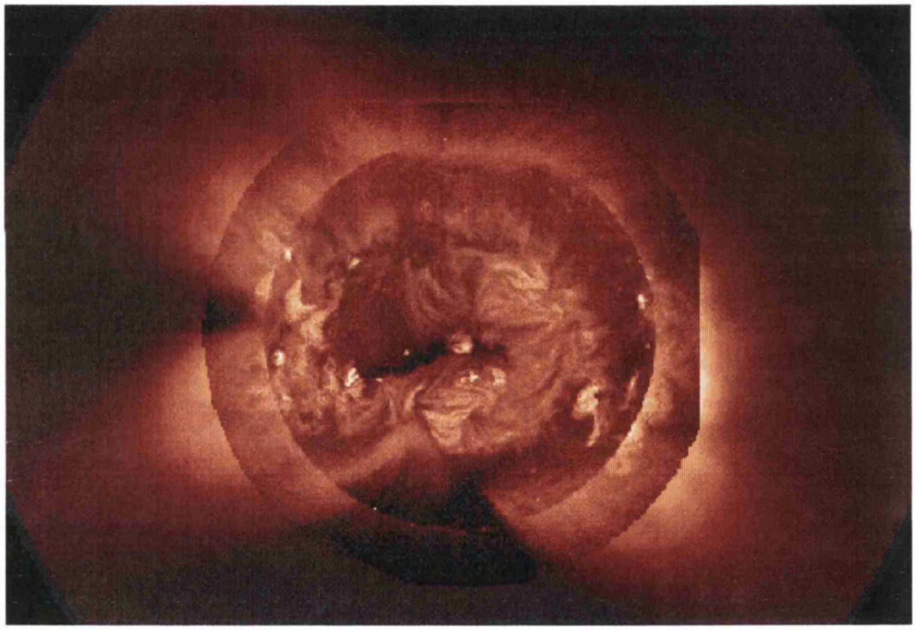

A composite of the corona observed with the MK3 Mauna-Lao Coronagraph (outer region), and the Yohkoh SXT.

5.1 Introduction

The corona outside coronal hole regions is generally very structured and inhomogeneous when observed in coronal emission lines. The observations demonstrate that it is composed almost entirely of loop like structures in various different arrangements and scale (see for example Rosner, Tucker, & Vaiana, 1978). The loops, which most probably represent bundles of filamentary magnetic flux tubes, have been demonstrated to be aligned with the extrapolations of the photospheric magnetic field (*e.g.* Poletto *et al.*, 1975). This is anticipated for an atmosphere in which the magnetic pressure so greatly dominates the plasma pressure, as is the case for the solar corona, with a plasma beta$\sim 10^{-3}$ (*c.f.* §1.2). The conductive flux transverse to the magnetic field is typically 10^{-10} times less that along the field. Hence, these loops which are most visible in or around the active region corona where the field is known to be strong. These loops occupy much of the corona and are often highly time varying in their soft X-ray emission and consequentially their energy content. Their ephemeral existence is evidence of two important well known characteristics of the solar corona; its high conductivity, and the presence of an impulsive, spatially localised heating process. Conversely any observations of diffuse emission would indicate the presence of a background heating mechanism which is either not highly localised or has a frequency of occurrence such that the resultant heating takes place almost uniformly with area, as may be the case for the nanoflare heated corona (Parker 1988 and references therein). Indeed analysis of the soft X-ray emission observed from the active region corona by Yoshida and Tsuneta (1995), reveals that much of the emission around the usual bright coronal loops is somewhat diffuse in nature. An investigation of the observed lifetimes for active the region emission, with the radiative and conductive timescales, suggested that two fundamental forms of heating must be working in concert to maintain the corona. The soft X-ray observations made with the Yohkoh SXT of the global corona has revealed that much of it outside of active regions is also diffuse and that these regions generally possess positive temperature gradients, (Foley *et al.* 1995, Culhane, 1997). The most extended of these regions are identified as being the soft X-ray counterparts of coronal streamer structures which are identified in coronagraph images made of the extended corona. By definition diffuse regions cannot easily be classified as magnetically open or magnetically closed in the high latitude regions, as there is no clear evidence that either geometry can be excluded. Whether this diffuseness observed in the soft X-ray regime is due to unresolved closed and or open field emission remains unclear. However, loop structures and arcades are sometimes found to be discernibly embedded within the diffuse emission which in conjunction with the correspondence with streamers suggest they may in fact be magnetically mixed. The stability of this soft X-ray emission is also found to follow that of the white light counterparts, sometimes extending over several Carrington rotations. Although the emission is commonly stable over extended durations, periodic disturbances in the form of large scale eruptions are occasionally observed (Hiei *et al.*, 1993). These usually result in the prompt (few days) regeneration of the original streamer. A possible and widely accepted scenario for these eruptions is that they are a natural relaxation process for a stressed magnetic configuration due to the cumulative effects of differential rotation. This results in a build up of magnetic shear, which has been associated with enhanced heating within the active region corona, as has been noted and studied by Moore *et al.* (1996) and Falconer *et al.* (1997). This may also be the driver of heating within the high latitude corona also.

Historically the physical parameters within the quiescent corona have been investigated using many different instruments and observational techniques (see for example Withbroe 1970; Dupree, 1972, Mariska and Withbroe 1975, and Mariska and Withbroe 1978). These observations indicate that coronal plasma within the quiet corona outside coronal holes is both denser and hotter in comparison to that within coronal holes by $\sim 50\%$. with electron temperatures in the region of 1.5-2MK. However due to the relatively large uncertainties in the abundances and instrument calibration, these measurements have generally been averaged over the observed regions and an isothermal approach adopted. To be able to ascertain properties of the heating mechanism however, what is really required is the temperature, density, and flow as a function of height within discrete structures as is clear from the energy balance relation (*c.f. equation 4.3*). In the case of the diffuse and apparently unstructured corona these measurements have been relatively sparse. The best data prior to Yohkoh are those from the EUV emission lines obtained with the spectrometers of the telescopes mounted on Skylab. Analysis of this data was presented in various publications, the most notable of which was that of Mariska and Withbroe, (1978). They explored the range of possible vertical temperature gradients of the corona by using fundamental models to reproduce the observed emission gradients of Mg **X** λ62.5nm and O **VI** λ103.2nm, and using the emission observed in the relatively hot Si **XII** λ52.1nm (peak temperature of formation $\sim 2MK$) to constrain the upper limit of the temperature structure. One of these models was based on the temperature structure of the lower corona ($\rho < 1.4$) being solely explained by a conserved inward flow of heat. The application of Mariska's model to the data however resulted in the requirement for a significant energy sink within the lower corona which was deemed unlikely.

Sturrock *et al.* (1996) re-investigated the possibility that the vertical temperature structure in the diffuse corona could be reconciled with the model described above. They analysed a large scale diffuse region, selected from data obtained whilst the Yohkoh spacecraft was performing off-point observations. These data are generally of high quality due to the use of long exposures and image the faint high latitude corona more distintively. Their work assumed that the low corona may be approximated as being radial and spherically symetric. Radiation was also assumed neglible in comparison to the conductive flux. Based on these assumptions a temperature profile was generated which fit their data. The results of this study disagreed with those of Mariska (1978) in that the model provided an excellent fit to the data for the region investigated. However, these reports were conducted with the old telescope scattered light calibration which was reported in Hara *et al.* (1994). This erroneous calibration has been shown to be a possible explanation for the high temperature component reported by Hara for coronal holes observed with the SXT (chapter 3 *c.f.* figure 3.12). This erroneous calibration may may have similarly biased their temperatures due to an under correction of the telescope scattered light.

Other recent investigations of the temperature structure of the quiescent corona were made by line ratio analysis of SERTS EUV emission by Falconer

(1994). The temperature was found to increase linearly over the height range $1. < \rho < 1.2$ for three different observations. No attempt was made to quantify the variation of heat input as a function of height within the regions, although the conductive and radiative power were found to requirement energy deposition at or above the maximum observed height range. The linear temperature structure is however uncharacteristic of the increase in temperature which is expected for the conserved heat flux model as will be demonstrated in subsequent sections.

In this chapter the radial temperature structure in the diffuse and high latitude corona is investigated, and compared with the conserved heat flux model of Sturrock *et al.* (1996). Although substantial data is available, two dates were selected based primarily on the availability of high quality exposures, and the level of solar activity being reduced during the period of observation. This later criterion was used in an effort to reduce the contribution of the telescope scattered light from the bright active regions. Although this may not be anticipated to contribute significant flux in the lower coronal regions of the images, it is found to have an increasing contribution with height above the solar limb, with a typical contribution of the order of a few percent close to the limb increasing to $\sim$ 20 percent at $\rho \sim 1.5$.

5.2 Conserved Heat Flux Model

The assumption that the corona is static and in a state of hydrostatic equilibrium allows great simplication of the conservation of energy equation (*c.f.* chapter 4, equation 4.3). The energy along a static magnetic flux tube will then only be a balance between the heating, radiation and conduction terms ;

$$\mathrm{H(s)} - \Phi(\mathrm{T_e})\mathrm{N_e N_p} = -\frac{1}{A(s)}\frac{\mathrm{d}}{\mathrm{ds}}A(s)\kappa \mathrm{T}^{2.5}\frac{\mathrm{dT}}{\mathrm{ds}} \tag{5.1}$$

.where H is the volumetric heating rate, Φ is the radiative loss function, N_e is the electron density, T_e is the electron temperature, and κ is a numerical factor which has a weak dependence upon both temperature and density. Its value for coronal densities: $10^6 - 10^9$, and electron temperatures : $10^6 - 10^7$ is $10^{-5.77\pm0.1}$.$A(s)$ represents the rate of coronal expansion, for a spherically symmetric corona it takes on a value of ρ^2.

Equation (5.1) may be solved analytically without the use of numerical techniques (see for example Kano and Tsuneta 1996) as was required for the former relation (equation 4.3). If it is assumed that the radiative losses of the corona are neglible in comparison to the conductive flux equation (5.1) may be simplified further, resulting in an balance between heating and the conductive losses.

$$\mathrm{H(s)} = -\frac{1}{A(s)}\frac{\mathrm{d}}{\mathrm{ds}}A(s)\kappa \mathrm{T}^{2.5}\frac{\mathrm{dT}}{\mathrm{ds}} \tag{5.2}$$

If E_t occurs at the top or above the maximum height of observation this can be expressed as

$$E_t = -A(s)\kappa \mathrm{T}^{2.5}\frac{\mathrm{dT}}{\mathrm{ds}} = -F_{co}A_o \tag{5.3}$$

where A_o is the area of the flux tube at the coronal base, F_{co} is the base conductive flux. This is simply an expression of the conservation of heat flux with height within the solar corona, and can be integrated for the general case where the coronal expansion rate goes as $A(\rho) = A_o\rho^{(b+1)}$ where $\mathrm{b} \geq 1$.

$$\mathrm{T_e}(\rho) = T_o\left[1 + \frac{3.5R_{\odot}bF_{co}}{\kappa T_o^{3.5}}(1-\rho^{-b})\right]^{2/7} \tag{5.4}$$

In the case of a radial spherically symmetric corona $A(s)$ may be expressed as $A(\rho) = A_o\rho^2$. This results in equation (5.4) representing the radial variation of temperature as expected for the conserved inward heat flux model for a spherically symmetric radial corona (equation 5.5), which is adopted here.

$$\mathrm{T_e}(\rho) = T_o\left[1 + \frac{3.5R_{\odot}F_{co}}{\kappa T_o^{3.5}}(1-\rho^{-1})\right]^{2/7} \tag{5.5}$$

5.3 Observations

The data were selected from the high quality coronal hole campaign as was discussed in chapter 4. During this period the Yohkoh SXT frequently recorded images through the thin filters with an enhanced exposure duration of 15 seconds (~ five times the nominal value). From this data archive observations were selected by excluding any data which were obtained whilst in transit of the SAA or during periods of highly transient solar activity.

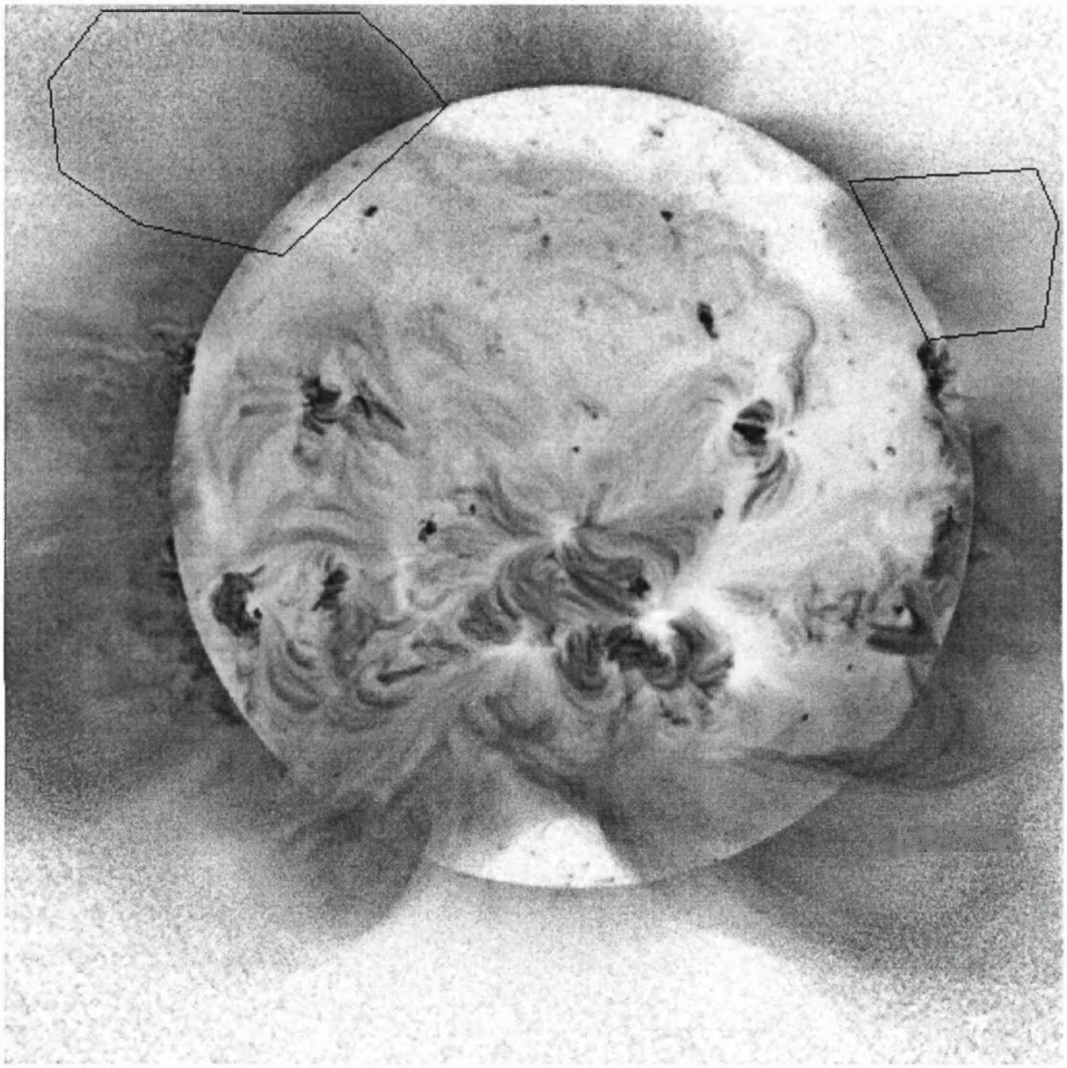

Figure 5.1: The solar corona observed with the Yohkoh SXT on the 10^{th} May 1992. The image has been enhanced using the method described in §4.2. The regions selected for analysis are those delineated in black above the north-east and north-west limbs.

5.3.1 1992 May 10

On this date a clear well resolved coronal streamer was located above the north east limb. Although the soft X-ray counterpart was diffuse, it could just be discerned as an arcade of loops of increasing height, (see figure 5.1). This region was selected as it was originally the region studied by Sturrock *et al.* (1997) on the observation date of 9^{th} May 1992. However, on this date the region appeared to be located behind the limb, hence the data obtained on the 10^{th} May were selected. Four pairs of high quality image pairs were successfully recorded on this date. In addition to the streamer, the region above the north west limb was selected for comparison. This region, unlike that above the north eastern limb, appears to be diffuse with no resolvable structure in the SXT data. Comparison with the coronagraph data taken with the MK3 coronagraph located at Mauna-Loa demonstrates that the region has no substantial white light counterpart, but appears to be typical of the quiet region, above which no systematic structures are observed to emerge.

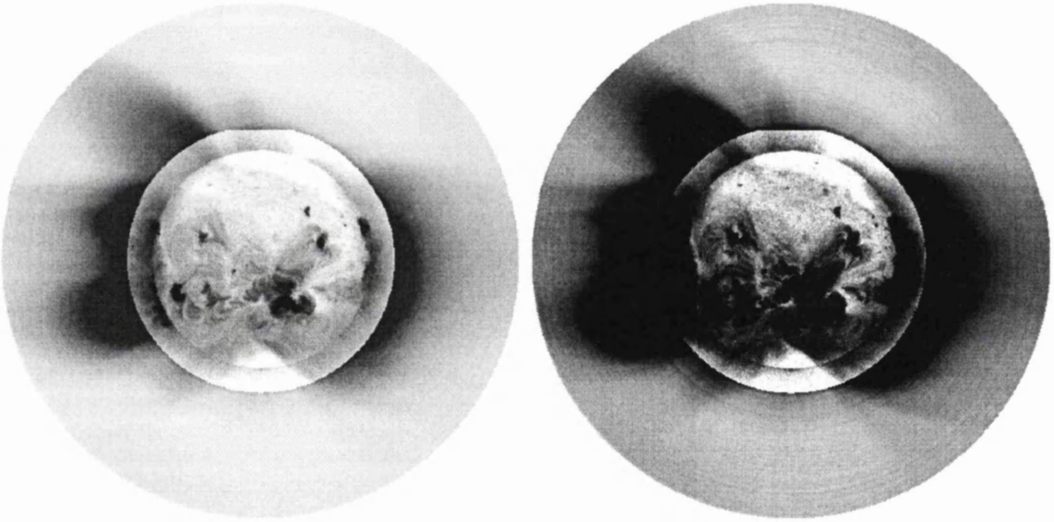

Figure 5.2: The observation of the extended corona with the Mauna Loa Solar Observatories MK3 coronagraph on the 10th May 1992. The coronagraph observes the corona between the height range of 1.1-2.5 solar radii. The centre has been replaced by an image obtained of the solar corona with the SXT, scaled with a square root algorithm so that the observed intensity is consistent with the density variation in the corona. The image on the right is the same as the left hand image, but rescaled to emphasise the fainter characteristics in the coronagraph. Note that in this image the correspondence between the SXT and the coronagraph is reduced, indicating that the emission observed by the SXT is generally due to closed field hotter emission.

5.3.2 1992 October 3

This observation was selected for the relatively small latitudinal extent of the high latitude regions on either side of the coronal hole observed in the north, and was described in detail in chapter 4, where the emission from the northern coronal hole was investigated. The MLSO MK3 coronagraph didn't record any data on that date due to cloud cover.

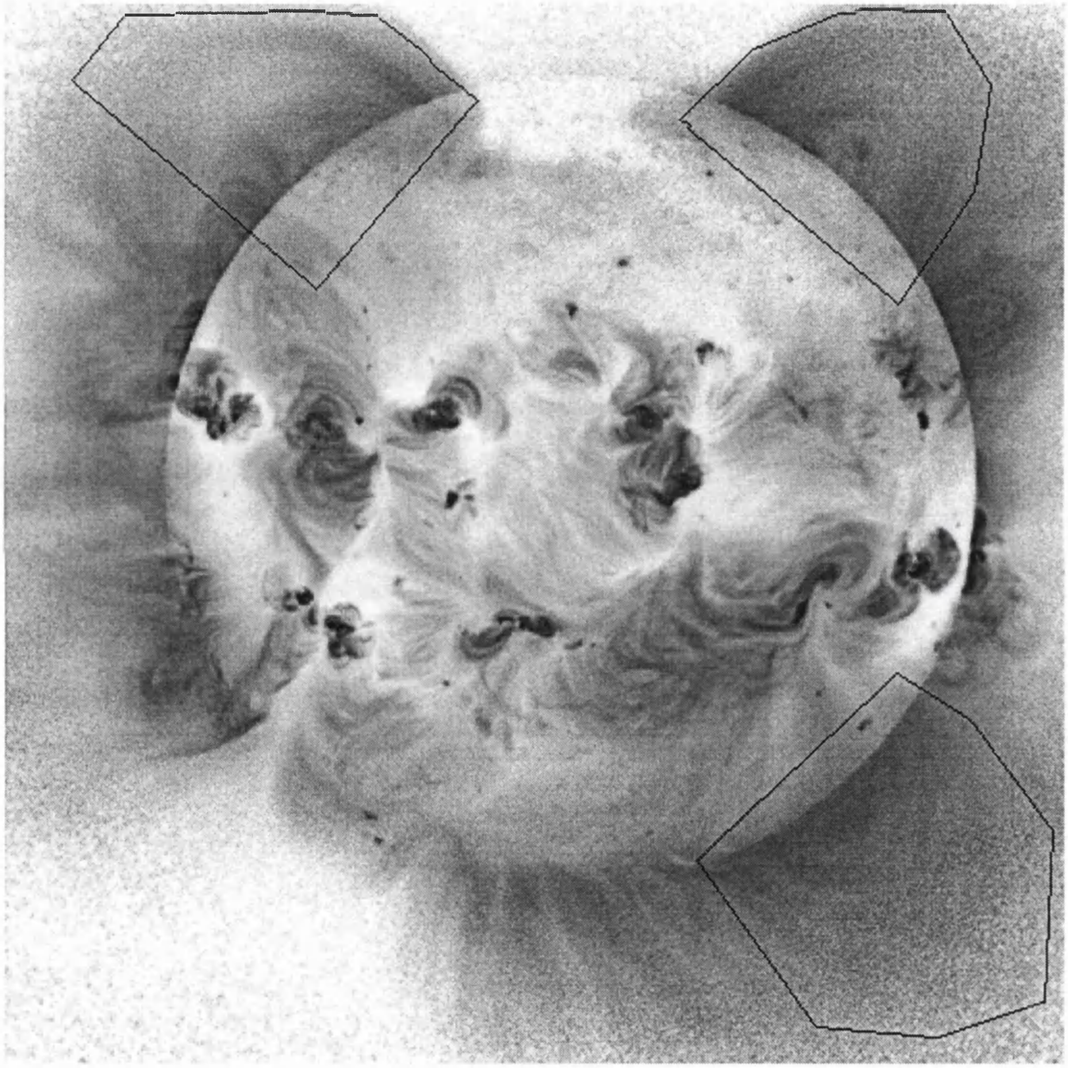

Figure 5.3: The corona observed on the 3^{rd} October 1992. The regions of interest are indicated with the solid black lines encompassing regions above the north-east, north-west, and south-west limbs.

5.4 Analysis and Results

The corrections and analysis techniques described in the previous chapter were applied in a similar manner to the data presented here. To reiterate, when extracting the radial variation in signal, the data which were contained in regions of equal distance from the disk centre were averaged. To preserve the statistical quality of the data with height, a minimum count rate was used to limit the radial extent over which this averaging was performed. This allowed a significant increase of the statistical importance of each data point due to the reduced size of the combined statistical errors, which were combined in quadrature. The errors assessed include those due to decompression errors, photon statistics, and the uncertainty in the background subtraction where the later includes the contribution of scattered light and dark current. Another possible source of error, which in some cases may be expected to dominate, is that due to the line of sight integration. This is anticipated to be maximised where the temperature gradient is at its greatest, *ie* close to the limb. It is then anticipated that neglecting the effect of this in an environment where the temperature gradient is positive results in a slight positive bias to the observed temperature profile, and in a negative temperature gradient a slight negative bias. This was indeed found for the coronal hole analysis contained in chapter 4. As neglecting the effect of this error is predictable it will not be addressed directly (*e.g.* using inversion techniques), but its possible influence on the results will be included as part of the chapters concluding comments.

In selecting regions along which to investigate the radial temperature structure it was found that the results were quite sensitive to the region selected. In order to have a consistent sample which is representative of the temperature structure in the base of these streamer structures, the selecting of sub elements of regions in this chapter has been excluded. This is left for a more critical assessment of the spatial temperature structure of these regions which is performed in the next chapter.

5.4.1 10th May 1992

North-East Limb

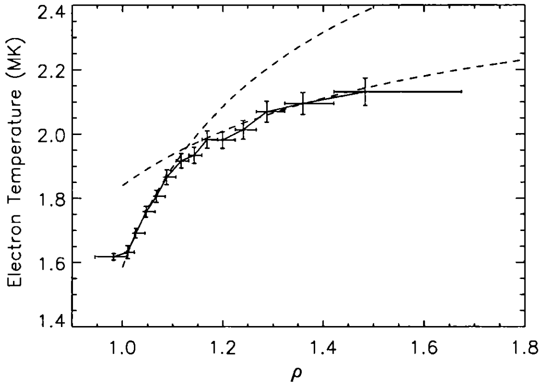

Figure 5.4: The temperature structure for the region above the North-East limb on the 10^{rd} May 1992. The dashed lines represent the best fits of the model to the data, which was performed for the two discrete height ranges. The values obtained are T_{eo} =1.58e6 and F_o =4e5 for ρ <1.07 and F_o =1.5e5,T_{eo} =1.84e6 for ρ >1.07.

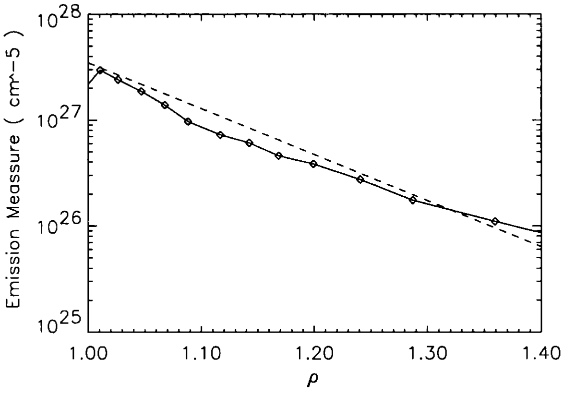

Figure 5.5: The emission measure determined for the temperature structure illustrated in 5.4, for the average signal observed above the North-Eastern limb on the 10^{th} May 1992. The dashed line represents the function $(5.5 \times 10^{13} \exp[-5.8 \times (\rho - 1)])^2$

North-West Limb

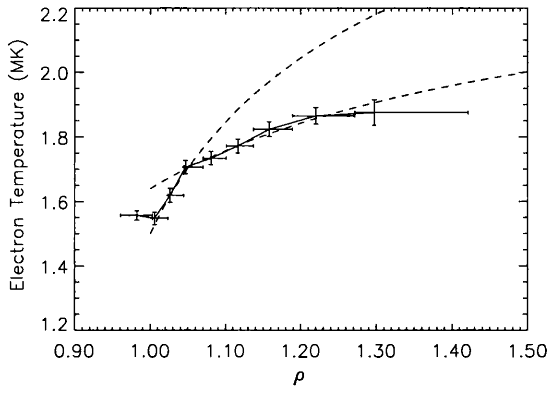

Figure 5.6: The temperature structure for the region above the North-Western limb on the 10^{rd} May 1992. The dashed lines represent the best fits of the model to the data, which was performed for the two discrete height ranges. The values obtained are T_{eo} $=1.5e6$ and F_o $=4e5$ for $\rho < 1.07$ and F_o $=1.4e5$,T_{eo} $=1.64e6$ for $\rho > 1.07$.

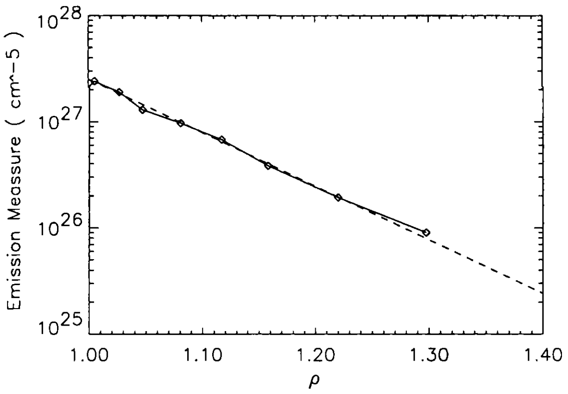

Figure 5.7: The emission measure determined for the temperature structure illustrated in 5.6, for the average signal observed above the North-Western limb on the 10^{th} May 1992. The dashed line represents the function $(5 \times 10^{13} \exp{[-5.8 \times (\rho - 1)]})^2$

5.4.2 3^{rd} October 1992

North-West Limb

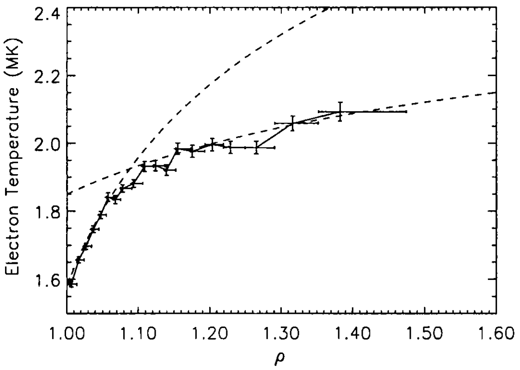

Figure 5.8: The temperature structure for the region above the North-Western limb on the 10^{rd} May 1992. The dashed lines represent the best fits of the model to the data, which was performed for the two discrete height ranges. The values obtained are T_{eo} =1.58e6 and F_o =5e5 for ρ <1.07 and F_o =1.3e5,T_{eo} =1.85e6 for ρ >1.07. The variation above $\rho = 1.07$ is better represented by the linear function $T_e(\rho) = (\rho - 1) * 0.58MK + 1.87MK$

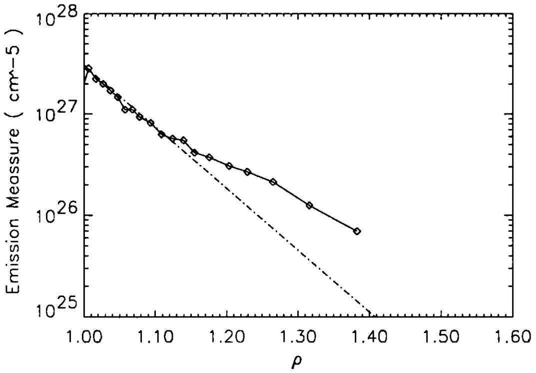

Figure 5.9: The emission measure determined for the temperature structure illustrated in 5.8, for the average signal observed above the North-Western limb on the *3^{rd} October 1992.* The dashed line represents the function $(5.5 \times 10^{13} \exp[-7. \times (\rho - 1)])^2$.

North-East Limb

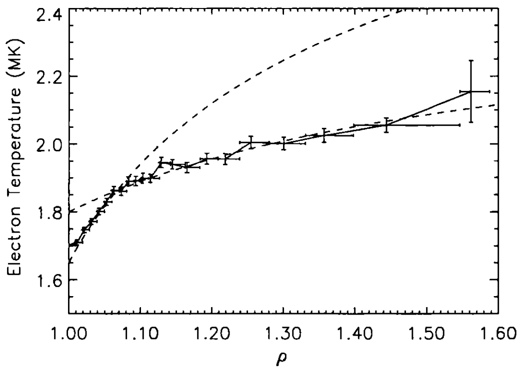

Figure 5.10: The temperature structure for the region above the North-Eastern limb on the 3^{rd} October 1992. The dashed lines represent the best fits of the model to the data, which was performed for the two discrete height ranges. The values obtained are T_{eo} =1.65e6 for ρ <1.07 and F_o =1.3e5,T_{eo} =1.8e6 for ρ >1.07. The variation above $\rho = 1.07$ is better represented by the linear function $T_e(\rho) = (\rho - 1) * 0.5MK + 1.85MK$

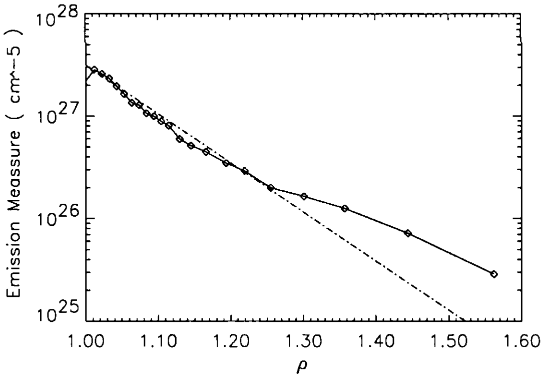

Figure 5.11: The emission measure determined for the temperature structure illustrated in 5.10, for the average signal observed above the North-Eastern limb on the*3^{rd} October 1992.* The dashed line represents the function $(5.6 \times 10^{13} \exp[-5.5 \times (\rho - 1)])^2$

South-West Limb

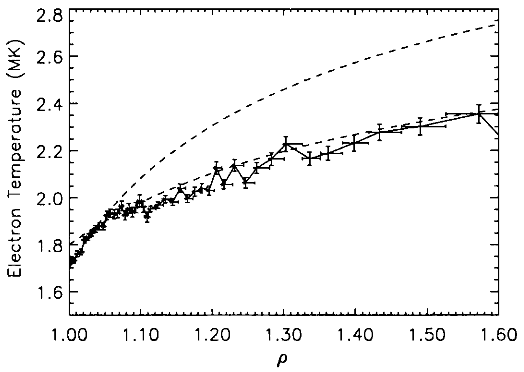

Figure 5.12: The temperature structure for the region above the south-western limb on the 3^{rd} October 1992. The dashed lines represent the best fits of the model to the data, which was performed for the two discrete height ranges. The values obtained are T_{eo} =1.7e6 and F_o =6e5 for ρ <1.07 and F_o =2.8e5,T_{eo} =1.8e6 for ρ >1.07. The variation above $\rho = 1.07$ is better represented by the linear function $T_e(\rho) = (\rho - 1.) * 0.8MK + 1.9MK$

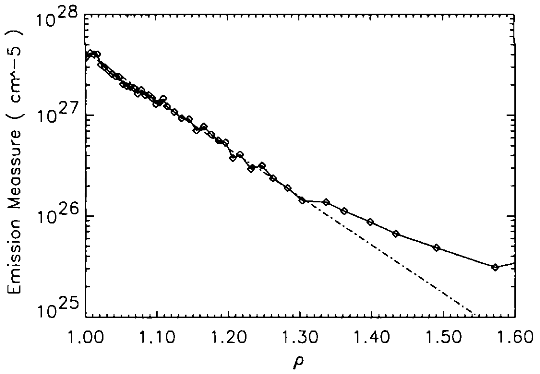

Figure 5.13: The emission measure determined for the temperature structure illustrated in 5.12, for the average signal observed above the south-western limb on the3^{rd} *October 1992.* The dashed line represents the function $(6.5 \times 10^{13} \exp\left[-5.5 \times (\rho - 1)\right])^2$

The comparison of the temperature structure determined for the large scale structure above the North-East limb on the 10^{th} May 1992 (figure 5.4) which was identified to be the soft x-ray counterpart of the white light coronal streamers, possess temperatures which are enhanced by about 10% in comparison to a more unstructured typical region of quiet corona which was located above the North-Western limb 5.6. This also is exhibited in the emission measures determined for the two regions with the absolute value illustrated in figure 5.5 being ~10% greater than than for the 5.7. The regions investigated for the 3^{rd} October 1992, all have similar structure to that found above the North-East limb on the 10^{th} May 1992. The most appreciable difference between the regions investigated is that the region above the south-western limb appears to be more extended over latitude. Interestingly this is also exhibited in the temperatures and emission measures obtained for the regions with the values obtained for the more extended region being enhanced by approximately 10% as depicted in figures 5.12. In all the regions investigated the temperature structures have been shown to possess a positive temperature gradient above the solar limb (figures 5.4, 5.6, 5.8, 5.10 and 5.12). A comparison with the conserved inward heat flux model which was applied successfully to the similar data by Sturrock *et al.* (1996), indicates that the regions are all inconsistent with the model over the complete height range. Although the model does not accurately describe the data through the entire height range, excellent fits are observed above and below a particular height (typically $1.1\mathrm{R}_\odot$). This is similar to the conclusion of Mariska and Withbroe (1978) who required an energy sink (radiation) in the low corona $< 1.1 R_\odot$ to explain their observations. In the case of the results presented here an energy source is required as opposed to an energy sink. An energy sink would in fact reduce the total conductive loss from the corona, not increase it as is required. This being the case the magnitude of the expected radiative losses in the corona are investigated in the next section.

5.4.3 Radiative Loss

The radiative losses in the solar corona have been estimated to be approximately an order of magnitude smaller than the observed conductive loss from the corona (few $\times 10^5$ergs/cm^2/sec; see Kopp, 1972), with a magnitude in the region of a few $\times 10^4$ergs/cm^2/sec. This generally supports the hypothesis that the radiation in the corona is not a significant loss mechanism. However, in the work of Falconer (1994) it was found that the dominant energy loss mechanism in three coronal regions investigated with the EUV SERTS instrument was radiation as opposed to conduction. His estimates varied from $\sim 1\times 10^4 - 3\times 10^5$ ergs/cm^2/sec. It is clearly important to validate the assumption that the coronal conductive loss significantly exceeds the radiative losses. This is particularly important for the work contained here as it was a principle assumption In order to calculate the radiative flux from a region it is clearly necessary to estimate the density so that the quantity of radiation can in turn be calculated. A useful estimation uses the fact that as the region is static and in a state hydrostatic balance, the density will fall off with a scale height $\sim 5800T_e cm$ (for an isothermal corona *c.f.* §1.2.2). This results in typical scale heights of $\sim 0.18R_\odot$ for a mean coronal temperature of $\sim 2.2MK$ as implied from the results above. This has the implication that the emission observed is strongly dominated by that perpendicular to both the observers line of sight and the limb. The emission measure distributions (illustrated in figures 5.5, 5.7, 5.9, 5.11 and 5.13) correspond to scale heights approximately equal to this value. Thus, the value of ~ 0.18 is used to represent exponential decline of the coronal density above the limb in the following analysis. The emission measure using equations 2.4, and 1.6 can be represented as

$$EM = \int_{-200R_\odot}^{\inf} N_e^2 \exp\left[2\Pi^{-1}(1-\rho)\right] dl \tag{5.6}$$

or

$$EM = N_e^2(\rho')\xi \tag{5.7}$$

, where Π represents the effective scale height, dl is the line of sight element, and ξ is the effective line of sight. The former of these two relationships may be integrated numerically (performed using a five-point Newton-Coates integration formula incorporated into IDL's *int_tabulated*). This was performed over the truncated limits of $\pm 20R_{\odot}$. The results of this analysis for a range of effective scale heights is illustrated within Figure 5.14. The numerically determined effective scale heights are found to be reasonably represented by the relationship

$$\xi = 1.6\Pi^{0.5} - 0.4\Pi + 7\Pi^2 \tag{5.8}$$

The result of the numerical integration with increasing depth of the spherical shell is illustrated in Figure 5.15. Truncation of the integral appears to be validated by the observed asymptotic behaviour of its value towards an effective line of sight ξ of $0.83R_{\odot}$. This value for the effective scale height may then be used to determine an estimate of the radiative flux (F_r) from the corona. This is obtained from

$$F_r = \left((EM_{\rho=1}/L)\exp\left[2\Pi^{-1}(1-\rho)\right]\right)\Phi \tag{5.9}$$

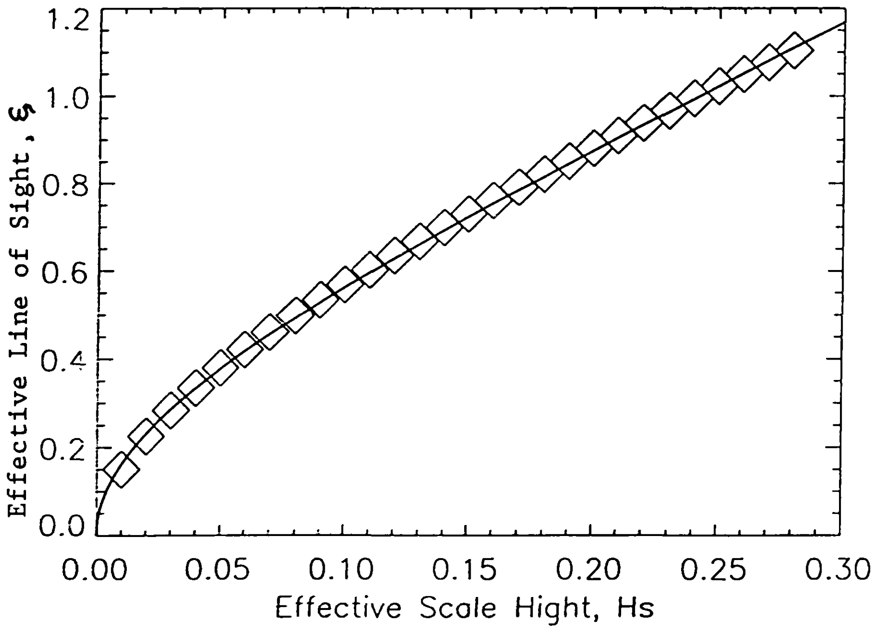

Figure 5.14: The effective line of sight for a radial and spherically symmetric coronal shell of depth ρ, and varying Π.

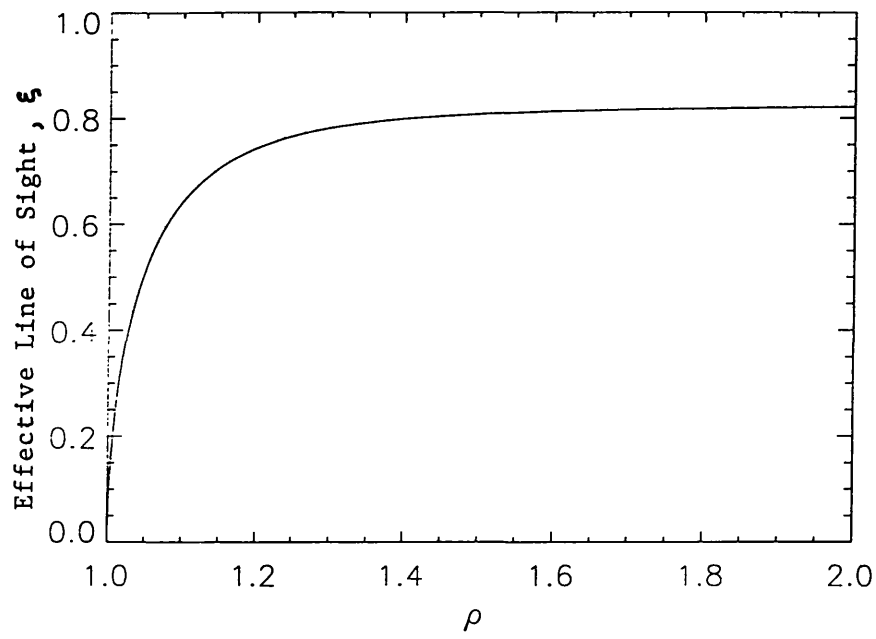

Figure 5.15: The effective line of sight obtained for the data presented in 5.14

where F_r is the radiative flux in $ergs/cm^3/sec$, EM is the determined value of the emission measure, and Φ is the radiative loss function from Cook (1989). The value of this function with height ρ is depicted in Figure 5.16, along with the value for F_r determined using the radial density structure determined by Withbroe (1988) for comparison [1]. Integrating this function over the lower coronal region yields a typical radiative loss within the range $1.03 - 1.1R_\odot$ $\sim 2 \times 10^4$ ergs /cm^2/sec, compared with conductive losses in the region of 3×10^5ergs/cm^2/sec. Thus it appears that neglecting radiation in this region is acceptable.

5.5 Discussion

In this chapter the temperature in the quiet regions of the solar corona which are observed to be the soft x-ray counterparts of the white light coronal streamers have been shown to increase with height. Comparison of the

---

[1] Withbroes radial density structure was determined by performing fits of a single fluid radiative energy balance model to the empirical observations of quiet unstructured regions of the corona (*c.f.* §4.3)

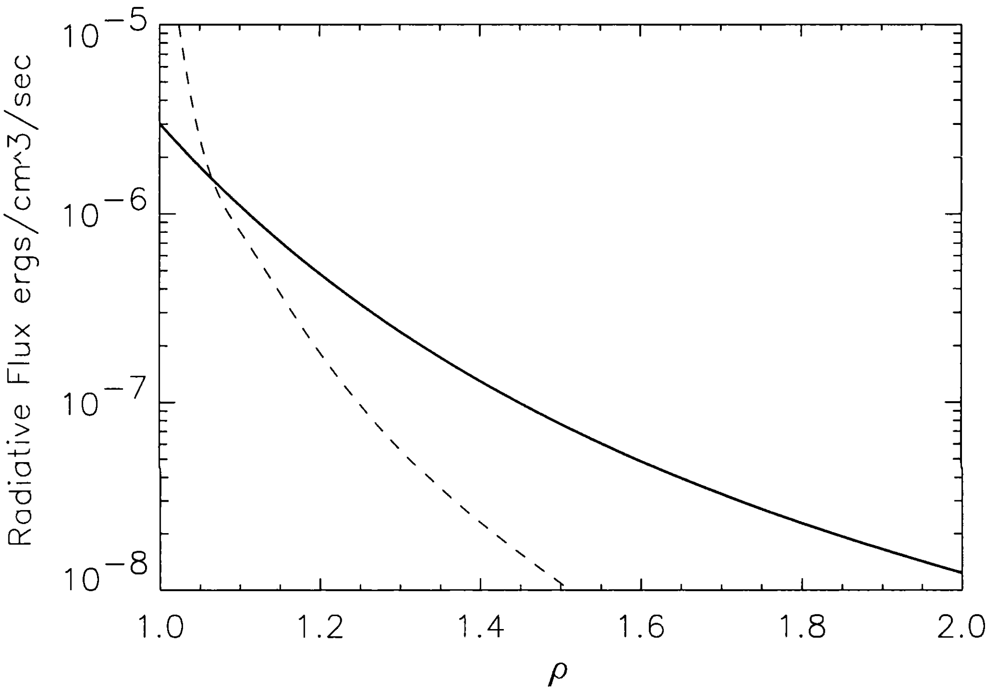

Figure 5.16: The radiative flux as a function of height above the solar limb as determined from the emission measure data (solid line). The dashed line again represents the radiative flux as a function of height, but evaluated using the quiet coronal density structure from Withbroe (1988)

data with a coronal region typical of the quiet corona not located directly below a coronal streamer demonstrates that the coronal temperature within the structures is enhanced by approximately 10%, as is its apparent emission measure. Attempts made to perform fits to a conserved heat flux model were unsuccessful over the whole height range, although excellent fits were obtained when the observed regions were split into a low corona (typically $<1.1R_\odot$), and extended coronal region ($1.1R_\odot$+). The application of the model to these two regions resulted in the conclusion that the conductive flux in the lower region exceeded that in the high corona by nearly a factor of two. If the representation of the coronal geometry as radial and spherically symmetric is correct, a conclusion that may be drawn from these data that energy deposition of the order of 3×10^5ergs/cm^2/sec is required in the height range 1-1.1 $R_\odot$ and 1×10^5ergs/cm^2/sec close to the summits of these structures to explain the observations. The latter of these energy sources may be a transient energy source such as those associated with the large scale eruptions of the high latitude corona (see Hiei, Hundhausen, & Sime, 1993). An alternative possibility is that modelling these regions as radial and spherically symmetric is unrealistic. This is in part confirmed from the enhanced images of the regions within which closed field loop structures are observed, which suggests the configuration is closed. The only concrete conclusion about the energy deposition from these observations that can be drawn without incorporating geometrical factors, is that energy must be deposited at great heights above the solar limb. It is conceivable that two heating processes are contributing to the observed temperature profiles. The observations here suggest that the dominant input would be located near the coronal base. It is additionally noted that the emission measure in the low corona is positively related to the overall temperature structure of a region, and subsequently the energy contained within a region. If we consider the emission to come from only closed field emission there is evidence that the temperature increases with the increasing height of the loops. This appears to be contrary to that expected from simple RTV scaling (*c.f.* §1.1.2) which was used by Klimchuk and Gary 1995 to describe the decreasing temperature discovered above the active region corona. However, with loops above a scale height this normal scaling may be expected to be influenced by the density stratification, and not to hold in the same manner (*see* Rosner, Tucker, & Vaiana, 1978).

Chapter 6

The Heating of Large Scale Loops

6.1 Introduction

In the previous chapter the spatially averaged electron temperature as a function of height in the diffuse corona was found to disagree with a simple conserved inward heat flux model. This model was applied to the data under the simplifying assumption that the regions under investigation were radial and spherically symmetric. However, the evidence from the enhanced images of the regions presented in the previous chapter (Figures 5.1 and 5.3) would appear to contradict this simplified geometry. Instead they are apparently composed of large scale loop structures which extend up to 400Mm above the solar surface. Thus the aim of this chapter is to isolate a large scale structure and obtain the temperature as a function of distance parallel to the loop's apparent magnetic topology. This can then be compared with that expected for the conserved heat flux model or other representations of the heating function.

There have been other studies to determine the condition of the plasma within coronal loops but these have generally been restricted to the most visible loops which are observed to exist within the active region corona. The height of these coronal loops within active regions usually does not exceed one coronal pressure scale height or approximately 70Mm and thus the density stratification which is expected to occur within a static coronal region (*c.f* §1.2.2) is negligible. Consequentially, these previous studies have usually adopted constant values for the electron density and temperature throughout the loops with the emphasis of the studies being a focus on the statistical properties of a reasonable sample of objects. The most notable of these analyses, prior to the observations with Yohkoh, was that performed by Rosner, Tucker, & Vaiana (1978) with the data obtained from the spectrometers flown on the Apollo Telescope Mount (ATM) on Skylab. This was a pioneering piece of work which firstly introduced the notion of the solar corona as a collection of many small coronas which were contained in magnetic loop structures. In their work a model was developed for these structures which assumed that they were ; quasistatic, thermally isolated from the ambient corona, and in a state of hydrostatic equilibrium. The result of the analysis was a derived expression which is commonly known as the *loop scaling law* (*c.f. §1.1.2*) which may be expressed as :

$$T_m = 1.4 \times 10^3 (PL)^{1/3} \tag{6.1}$$

where T_m is the maximum temperature, P is the pressure, and L is the loop length. The relationship was derived under the assumption that the loops investigated were in a state of hydrostatic equilibrium. Thermal stability arguments were used to deduce that energy deposition was required along most of the loop length with the actual temperature maximum being located close to the loop apex. Reasonable agreement was observed between the parameters predicted by the model and the peak electron temperatures and pressures. The agreement of the model with the data demonstrated that it is reasonable to assume that coronal loops can be viewed as isolated mini-atmospheres well approximated by hydrostatic equilibrium. More recent work with data obtained with the Yohkoh SXT on the subject of *the loop scaling law* has been performed by Kano and Tsuneta (1995). In this work the exact scaling law determined by RTV did not fit the data although a slightly modified expression was found to be an resonable representation of their observations :

$$T_m = 3.8 \times 10^4 (PL)^{1/(5.1 \pm 0.5)} \tag{6.2}$$

Although the equation is different in detail to that obtained by Rosner, Tucker and Vaiana (1978) it still confirms their original findings. The difference in the values of the normalisation and power law obtained were attributed to the different sensitivity of the Yohkoh SXT and Skylab's soft X-ray telescope. The conclusion of these *scaling law* studies allow the observed coronal loops to be considered as individual static systems, the energy balance of which may be described with equation (5.1).

The qualitative characteristics of the coronal heating mechanism for coronal loops were also recently investigated using the observational characteristics in Yoshida and Tsuneta (1996). This work investigated the emission structure of the active region corona and found that the observed structures could generally be described by two different species of structure ; quasistatic and impulsive. These observations suggest that the fundamental mechanism responsible for their heating may similarly be quasistatic or impulsive. The general emission characteristics which they reported were also found to be reflected in the temperature structure of the active regions which they determined using the filter ratio method (*c.f* section 2.3). In these temperature maps the structures seen in the soft X-ray images lost their identity completely. These characteristics are also reflected in the soft X-ray observations of the high latitude regions within which it is often difficult to resolve any loop structure, both within the soft X-ray images and the temperature maps. The closed field nature of the high latitude regions is often confirmed during transient heating events during which emission along the magnetic field is enhanced as the energy is re-distributed by thermal conduction along the field lines. These transient events (see Hiei, Hundhausen, & Sime, 1993; and Hudson, Acton, & Freeland., 1996) are presumably the same as those which are frequently observed within the active region corona. To reiterate it may be similarly hypothesised that the reason for the diffuse characteristics of the corona both within and outside of the active regions is due to the same ubiquitous heating mechanism which is spatially uniform over the typical observational and cooling time scales.

Kano and Tsuneta, (1996), as a progression to their work on the *loop scaling law* (described above), investigated the variation of the electron temperature along the individual loops. This revealed that the temperature along the loops from the footpoints appeared linear over much, or even all, of their length on a $T_e^{\frac{7}{2}}$ vs s plot. This was interpreted as indicating that the energy deposition was concentrated around the loop tops, with the temperature profiles throughout the lower portions of the loops being a result of the conductive heat flow to the lower cooler parts of the loops and the transition region. The study was restricted to loops located around the centre of the disk, which may have influenced their results due to the non linearity of their geometrical interpretation of the length along the loop and other projection effects as have been highlighted by Alexander and Katsev (1996). The analysis of the large scale coronal loop structures within which the spatial deposition of heat would be more clearly determinable from the temperature structure will be discussed in the next section.

6.2 Energy Considerations

The theory for the heating of the loops follows a similar path to that of the analysis in §5.2, which uses the static energy balance equation as a starting point. In this case we can use the hypothesis that the energy input is along the loop, and not concentrated at the loop top. Integration of the relation leads to the expression for the temperature along the loop (Priest, 1997).

$$T = T_o \left[1 + \int_o^s \frac{3.5}{\kappa A(s') T_o^{3.5}} ds' \int_{s'}^{l} H(s'') A(s'') ds'' \right]^{2/7} \tag{6.3}$$

where l is the half loop length ($l = 0.5L$) .

In a study of the variation of cross sectional area as a function of height in the solar corona Klimchuk *et al.* (1992) found there to be little. Thus a useful and acceptable simplification on this basis is adopting a constant value of unity for $A(s)$. In the next 3 subsections the fundamental modes in which the heat may be distributed along the coronal structures is examined. In all the models radiation has been assumed to be negligible in the corona as was implied in §5.4.3.

6.2.1 Exponential Heating from Coronal Base

As discussed above, the thermal stability analysis of static coronal loops was used by Rosner, Tucker, & Vaiana (1978) to demonstrate that heating was required over much of the coronal loop lengths. A suitable form for this heating which has been commonly used to represent the coronal heating term for the quiescent corona, both open and closed field, is :

$$H(s) = H_o \exp^{-s/L_h} \tag{6.4}$$

where L_h represents the scale length over which the heating decays exponentially, $H(s)$ is the heating flux at distance s along the loop, and H_o is the heat flux at $s = 0$ (see Endler *et al.*, 1979). An example of the mechanical form for this mode of heating is the dissipation of MHD waves. Indeed, the expression for the mechanical energy flux which was used in the analysis of Withbroe (1988) took this form (which is the basis of the analysis of the coronal hole emission presented in chapter 4). Incorporating this heating function into equation (6.3) leads to an expression for temperature structure for heating which decays exponentially from the foot points.

$$T(s) = T_o \left[1 + 3.5 \frac{H_o L_h^2}{\kappa T_o^{3.5}} \left(1 - \frac{s}{L_h} \exp^{-l/L_h} - \exp^{-s/L_h} \right) \right]^{\frac{2}{7}} \tag{6.5}$$

with a maximum value of

$$T_m = T_o \left[1 + 3.5 \frac{H_o L_h^2}{\kappa T_o^{3.5}} \left(1 - (1 + \frac{l}{L_h}) \exp^{-l/L_h} \right) \right]^{\frac{2}{7}} \tag{6.6}$$

6.2.2 Constant Volumetric Heating Rate

The constant flux case, which may be expressed as $H(s) = H_o$, results in a temperature profile which is given by

$$T(s) = T_o \left(1 + \frac{3.5 H_o}{\kappa T_o^{3.5}} (ls - 0.5 s^2) \right)^{\frac{2}{7}} \tag{6.7}$$

with a maximum value of

$$T_m = T_o (1 + 1.75 \frac{H_o l^2}{\kappa T_o^{3.5}}) \tag{6.8}$$

The energy source for the mechanism which ultimately heats the corona is generally believed to originate from the turbulent motions of the convection zone (*c.f* §1.3). An alternative way (to wave dissipation) in which the turbulent motions of the convection zone may be dissipated in the corona is via DC field aligned currents, which would be expected to be generated by tangential discontinuities. These have been studied by Parker (1991) and would by generated naturally by the twist which is introduced into the overlying corona by the random motions of the photosphere. This form of heating is associated with the dissipation of energy in the many small current sheets which would be generated by the random photospheric twists of the coronal flux tubes, which would be anticipated to create highly tangled coronal structures. There are many reasons why this form of heating may explain the observed heating of the solar corona, a simple one being that the many current sheet scenario is the natural configuration of a coronal loop prior to it flaring. This is typified by the use of a self organised criticality analysis which may explain the power law frequency distributions of solar flares. It was noted by Hudson (1991) that an extrapolation of the observed flare occurrence rates to the nanoflare regime would result in a substantial shortfall in the energy for nanoflares to explain the energy budget of the corona. There is more recent statistical evidence that a simple extrapolation of a power law may not be valid as an upturn in the frequency of these events is expected when the energy scale is reduced closer to the more elemental region as reported by Georgeolis and Vlahos (1996).

6.2.3 Injection at Loop Apex

Solar flare observations have removed the spatial ambiguity of the energy release locations in solar flares with the launch of Yohkoh. These observations offer strong support for the solar flare being caused by an inverted Y type reconnection. The primary energy release site has been identified as occurring at the loop top from the simultaneous soft and hard X-rays of solar flares (Masuda, 1994). This form of heating is also observationally consistent with the cusp features which are often observed in the active region corona, and have been demonstrated to be well represented by the model of Tsuneta in which the energy is injected into the newly forming coronal loops by way of a reconnection jet originating from an overlying current sheet. Additional observational evidence for this form of heating can be obtained from the fact that these coronal streamers have been identified to be sites of the type III radio bursts. These bursts are mostly believed to be generated by the non-thermal flow of accelerated electrons. The case of energy injected at the loop top was presented in equation (5.3) in the previous chapter. However, in this chapter it is assumed that there is no significant expansion in volume of these coronal loops with altitude, the area expansion factor being represented by a constant. The relationship for the temperature as a function of height then becomes :

$$T(s) = T_o \left(1 + 3.5 \frac{F_{co} s}{\kappa T_o^{3.5}}\right)^{\frac{2}{7}} \tag{6.9}$$

where F_{co} represents the conductive flux which flows through the loop.

6.3 Analysis and Results

6.3.1 Loop Analysis

In this section the temperature structure along an isolated large scale loop is extracted and compared with the three forms of heating which have been discussed above.

The loop region has been selected from the data observed on the 3^{rd} October 1992, which was the basis of the analysis presented in the previous two chapters. The corrections applied have been described in §4.2 and will not be discussed again here. The data obtained over a period of 15 hours was summed, in a similar manner to the analysis of the coronal hole region (§4.2). It would of course be preferable to obtain the coronal parameters as a function of time to verify that there is no significant evolution in the results over the observational period. However, due primarily to the exponential decline in the coronal intensity as a function of height, the CCD signal in locality of the loop top is comparable to that within the coronal hole region. As the models which were described in the previous section are most sensitive to the form of heating close to this region, a similar temporal sampling is used to obtain a reasonably significant count rate within the loop apex region. During these observations made on the 3^{rd} October 1992, structures could be partially resolved above both the North-Eastern and North-Western Limb. The region above the North-Eastern limb was however observed to fade substantially over the observation period and thus may not

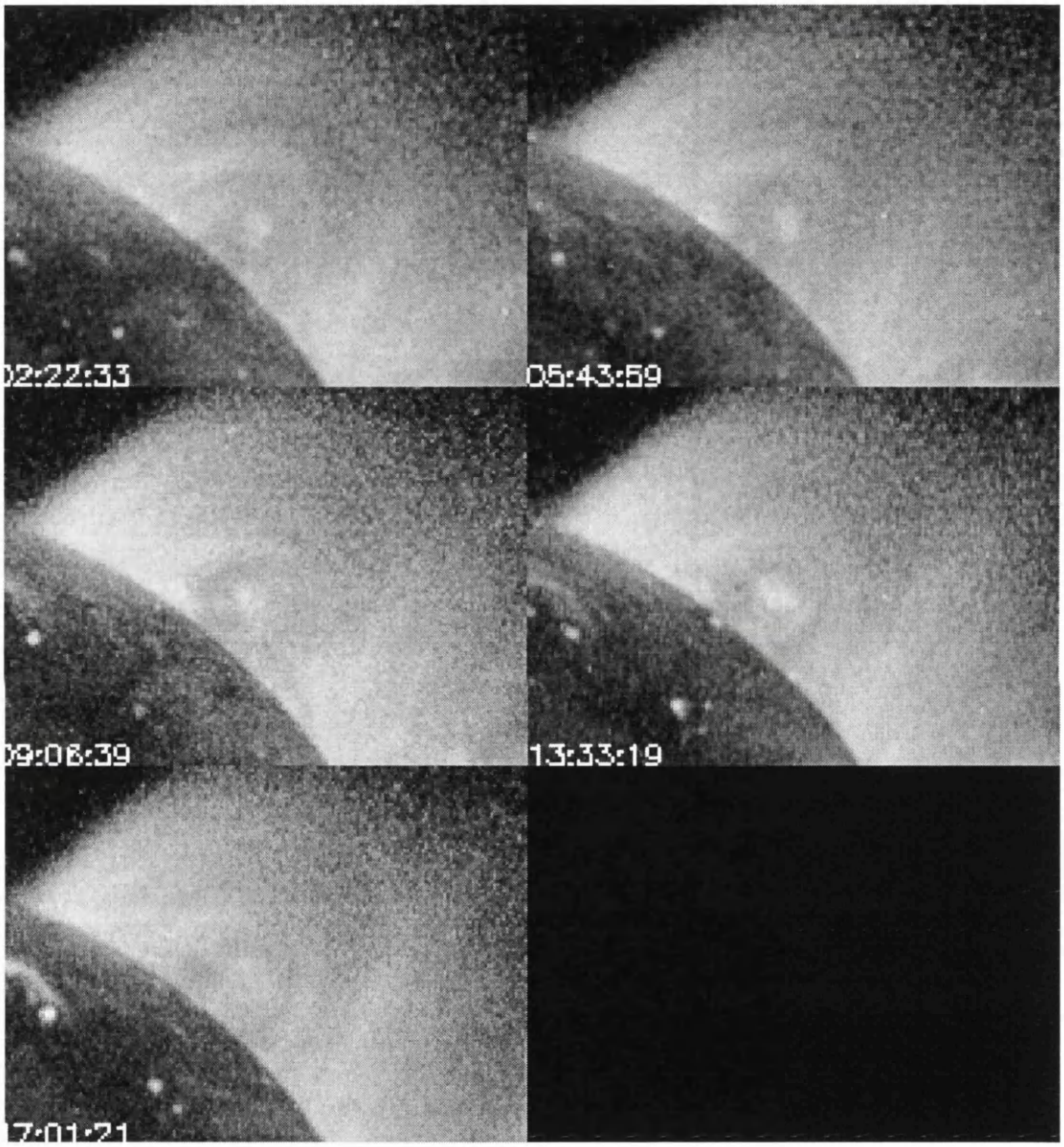

Figure 6.1: The emission observed above the North West limb over the period of observations. The diffuse nature of the region is readily apparent, however there is no evolution with time.

be considered to be in a quasistatic equilibrium. Instead it appears that this large scale structure is heated transiently as was discussed above for elements in the active region corona. The analysis which is now described is thus limited to the region above the North-Western limb, which appeared more stable over the observation (see Figure 6.1). Perceiving the structure, which is delineated in Figure 6.2, is difficult in the usually compressed soft X-ray images. This is again due principally to the exponential decline in the coronal density (and thus emission measure) above the solar limb (*c.f* §1.2.2). For this reason the region has been enhanced by using an edge-enhancing algorithm which reduces the effect of the radial gradient in the images. This was applied by dividing the image by a smoothed version of itself. The overall result of the enhancement is illustrated in Figure 6.3 in which a truncated grey-scale is used to emphasise the loop structure. The signal obtained through the two broad band filters was then measured as a function of distance along the loop. This was used in conjunction with the filter ratio curves (*c.f.* 2.4) to infer a mean temperature for the plasma distributed along the line of sight. A minimum count rate was used to dictate the size of the region over which the counts were averaged.

The result of fitting the different forms models to the data are illustrated in Figure 6.4. The best fit was obtained for the uniform heating model which was fitted with the volumetric heating rate, H_o, and base electron temperature left free. The next best model deposited its heat at the top of the loop and was fitted to the data leaving the heat flux, F_o, and base electron temperature, T_{eo}, free. The exponential heating from each of the coronal foot-points was fitted with a damping scale length of $0.1l$ with the amount of heat H_o and base temperature T_o left as free parameters. This model was the worst fit to the data. However, when the damping scale length was included as a free parameter the model provided a fit indistinguishable from that obtained for the uniform heating case. In a similar manner a slight modification to the second model may be an incorporation of a parameter which represents an axi-symmetric distribution of the heating about the loop apex. This would similarly relax the model sufficiently that it would in fact provide a similar solution to the observed temperature profile. Thus, it appears that a definitive solution to the coronal heating problem cannot be

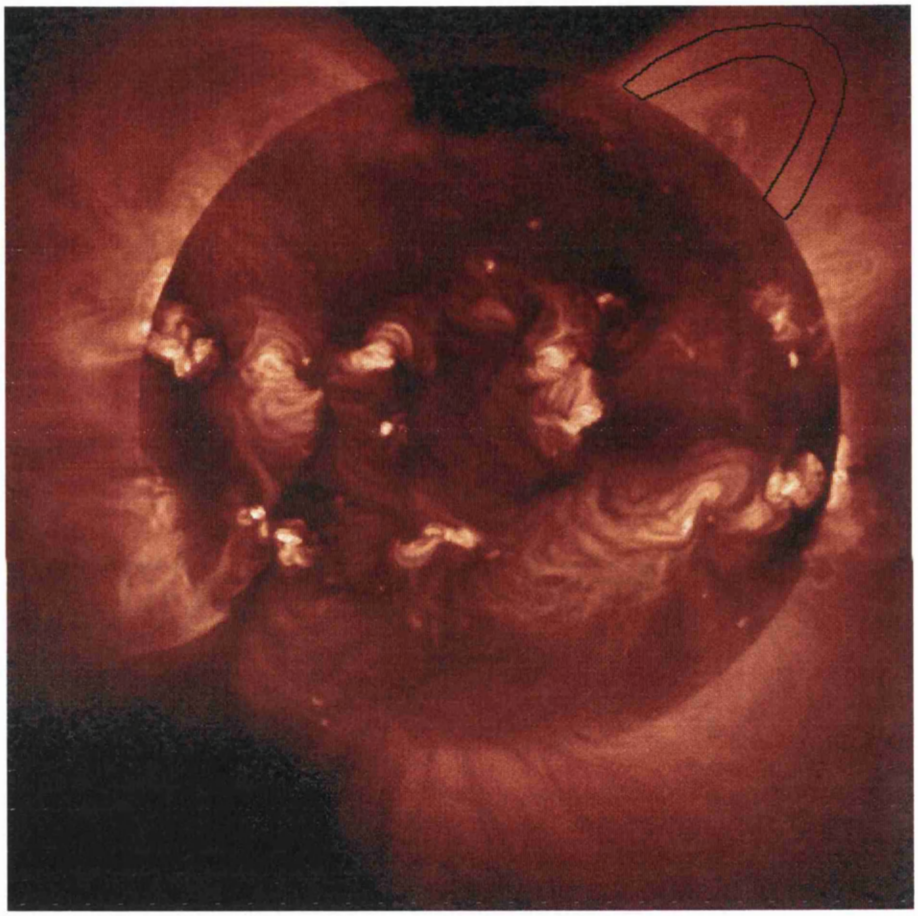

Figure 6.2: The solar corona observed on the 3 October 1992. The large loop regions analysed are delineated in black.

obtained from the observed temperature profile alone although extreme case scenarios may be excluded. A simple statement which is clearly apparent from these observations, and is similar to that stated in the previous chapter, is that whatever the nature of the heating mechanism it extends to great heights in the corona.

6.3.2 Arcade Analysis

An alternative approach to the heating problem is to address the implications for the underlying heating mechanism which may be ascertained from the variation of temperature from loop to loop. This is a direct indication of the relative amount of heating going into structures of increasing height. Further information which can be obtained simply from the observed temperature structure is a measure of the relative heating rate for structures of increasing loop length. This variation has been demonstrated to be useful in discriminating between competing heating mechanisms (*see* Porter and Klimchuk, 1995). In the case of the observations reported here it is possible to explore this by extracting the temperature from the central axis of the region and assuming it to be composed of concentric loops. This has been performed for the region located above the North-Western limb which contains the large loop structure analysed in the previous section. The temperature extracted is illustrated in Figure 6.5 within which the dependence of the electron temperature, T_e, on the half loop length, l, is illustrated by the dashed line. This may be represented by

$$T_e \propto L^{0.07} \tag{6.10}$$

This can be used in conjunction with the energy balance equation (5.1) to estimate the dependence of the loop averaged heating rate, $< H >$, as a function of loop length. This has been done by Klimchuk and Gary (1995). In their work it was assumed that radiation is negligible in comparison to both the heating and conduction terms with the conductive flux approximated as the right hand side of :

$$< H >= \frac{2}{7}\kappa\frac{T^{3.5}}{L^2} \tag{6.11}$$

where $< H >$ represents loop averaged volumetric heating rate. The expression is derived under the additional assumption that the cross-sectional area of the coronal loops is independent of their loop length. This assumption appears to be validated by the observations made with Yohkoh (*see* Klimchuk *et al.*, 1992). Substitution of the electron temperature dependence, equation (6.10), into this expression yields the dependence of $< H >$ on the length of the loop :

$$< H > \propto L^{-1.75} \tag{6.12}$$

This compares favourably with a similar statistical study of 47 coronal loops by Porter and Klimchuk, (1995). In their work it was determined that the variation was in the region $L^{-1.95\pm1}$. This dependence of the volumetric heating rate upon the loop half length to the power -2 was also demonstrated in their work to be consistent with Parker's (1983, 1988) nanoflare model. In Parker's model the photospheric convective motions cause twist to propagate into the overlying corona and to be dissipated in the form of many small current sheets, gradually or impulsively in the form of nanoflares.

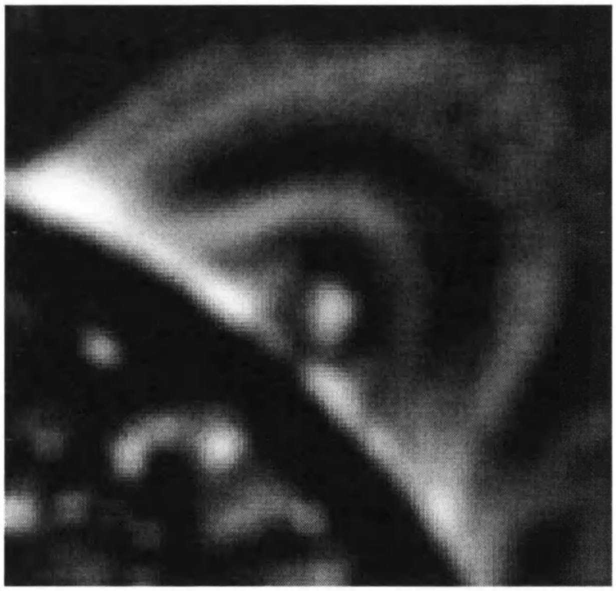

Figure 6.3: An enhanced image of the region delineated in figure 6.2

(a) Exponential decay over 0.1L

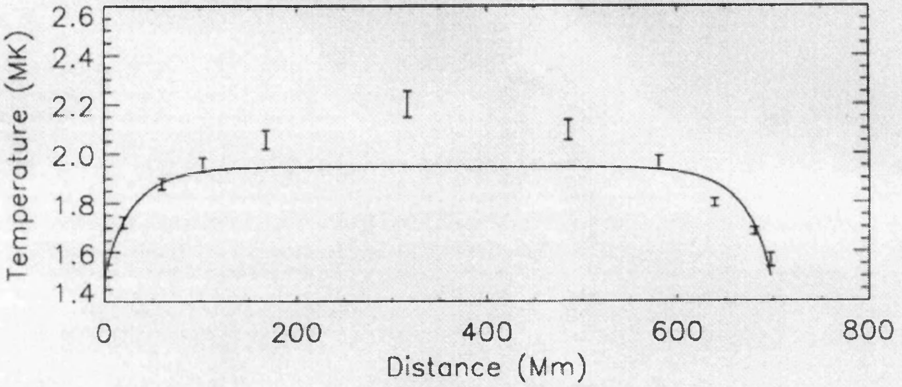

(b) Localised at top

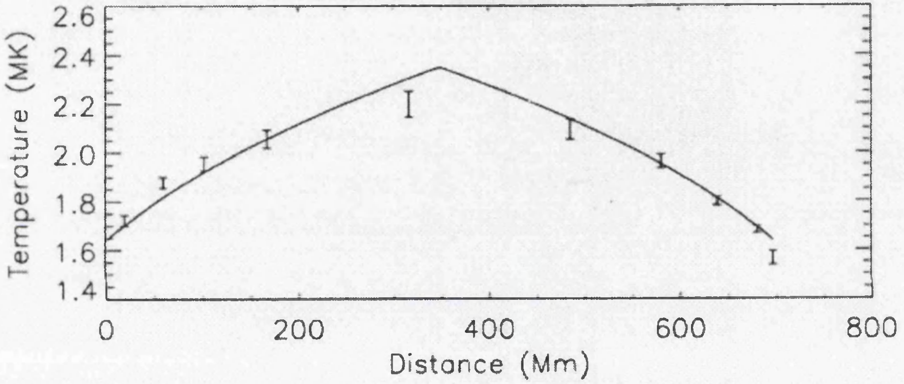

(c) Uniform

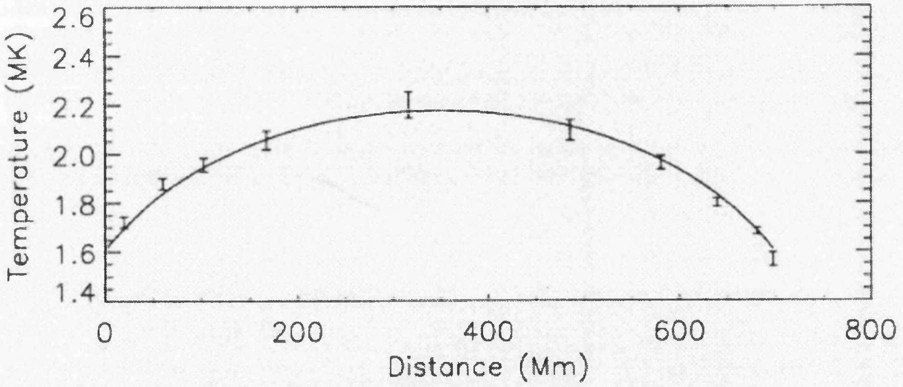

Figure 6.4: The temperature structure obtained along the large scale loop structure clearly observed above the North-Western limb on the 3^{rd} October 1992 . The fits of the three individual models are displayed together

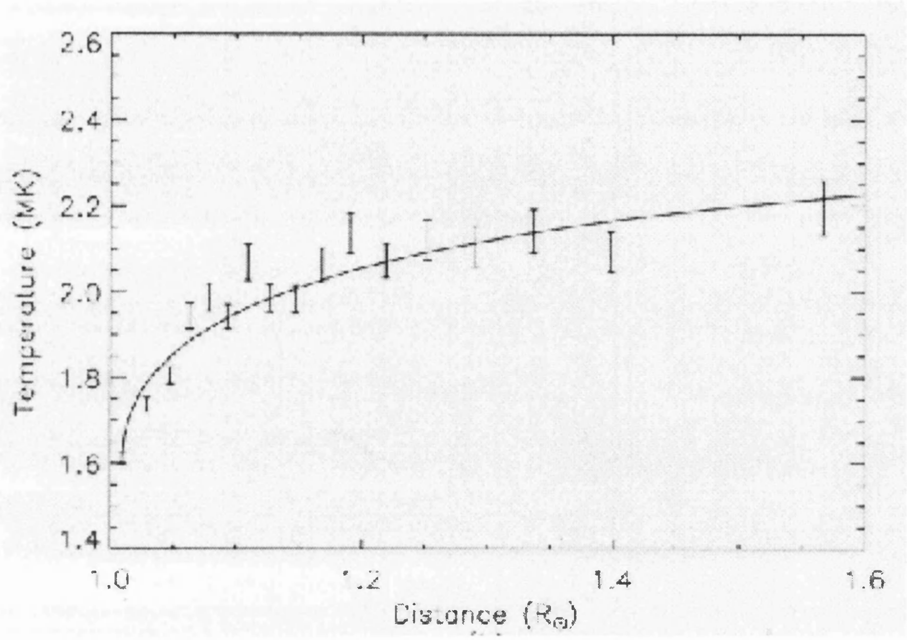

Figure 6.5: The temperature structure through the centre of the arcade (North West Limb).

6.4 Conclusion

In this chapter the temperature distribution along a large diffuse coronal loop has been extracted using the images provided by the Yohkoh SXT. The temperature structure was then compared with that expected for three fundamental coronal heating models. This comparison suggests that uniform heating would best represent the observations. However, by refining the latter two models slightly by incorporating one additional free parameter both of the other models may also provide reasonable representations of the observed temperature variation.

An examination of the variation of temperature as a function of loop length through the axis of the region (making the assumption that the observation is of an arcade of concentric coronal loops) demonstrates that this varies approximately as $T_e \propto L^{0.07}$, which in turn suggests that the time averaged heating rate along each loop varies approximately as $L^{-1.75}$. This was found by Porter and Klimchuk (1995) to be an important parameter to distinguish between competing mechanisms of coronal heating. The magnitude of the dependency of L found in this work would be supportive of

Parker's nanoflare heated corona. The uniform heating which was found to best represent the large loop's temperature profile would also be expected from his model.

The general emission characteristics of the high latitude corona are found to resemble that of the active region corona with the heating taking on two fundamental forms : episodic and quasi-continuous. From the analysis along the structure in this chapter there is evidence that the quasi-continuous form appears to heat these large scale coronal features relatively uniformly and inversely with the coronal loop length to almost the second power. However, other forms of heating may be found to represent the data for the isolated structure with some refinement. This result combined with the observed radial variation through the tops of the structures would suggest that a fundamental form of heating that can reproduce the observations reported here could be that due to nanoflares.

Chapter 7

Summary and Future Work

7.1 Telescope Scattered Light

The scattered light from the SXT's mirror surface has been evaluated using the halos surrounding a sample of solar flares. The measured levels were then extrapolated to longer wavelengths relevant for the emission associated with non-flaring plasma. This was done using an expression which represents the effect of surface roughness on the reflectivity of the mirror. In measuring the level of scattered light it was noted that a significant variation was observed in the scatter level with azimuthal angle (in the plane of the CCD). This variation was found to be roughly commensurate with an estimate of the effective area of the mirror surface.

It is clear that in future work careful consideration of the effect of vignetting on scattered light is required. This is particularly important when evaluating low level signals as has been performed in this thesis. It is probable that with brighter X-ray sources, such as those available at the European Synchrotron Radiation Facility (ESRF), the full characteristics of the telescopes response will be evaluated prior to flight (as has been the case for the mirrors of AXAF ; see Zhoa, & Speybroeck, 1995).

7.2 Plasma Parameters within a Polar Coronal Hole

An observation of a coronal hole, which was demonstrated to be free of significant contribution from structures surrounding it has been used to compare the emission observed with that expected from the observations reported during the Skylab era (and represented by the model of Withbroe, 1988). The results suggest that these regions do not possess any plasma with an electron temperature in the region of 2MK as was suggested by Hara *et al.* (1994). The possibility that the solar wind is thermally driven was also examined, and conclusively excluded. The observations however cannot place strong empirical constraints on the absolute variation of electron temperature with height, although they have demonstrated the temperature values to be broadly consistent with the prior empirical information.

The recent observations with the various instruments of SOHO have indicated that the electron temperatures present within coronal holes are even lower than implied from the observations reported here. For example David *et al.* (1998) report temperatures in the region of 0.8MK close to the limb in which the temperature is observed to rise to approximately 1MK (at $\rho = 1.15$) and to fall again to 0.4Mk at a distance of ($\rho = 1.3$). These observations are supported by similar reports by Wilhelm *et al.* (1998) for the SUMER instrument. There are two clear possible reasons for the differences which are ; (1) The work presented based upon the SOHO observations which were made during the minimum of the solar cycle. During this period the coronal hole regions are found to expand much more rapidly than that observed during solar maximum. Consequentially the plasma contained within holes would be expected to be less energetic during the minimum of the cycle. (2) The regions which are known not to be isotropic, may be expected to have different temperature components located at the same coronal heights, and SOHO sees the cooler component whilst the SXT observes the hotter. This is indeed a principle argument for observations of coronal holes made in soft X-ray's. The latter of these possibilities appears most likely, particularly since the plumes which exist within coronal holes are observed to be cooler and denser than the interplume regions (see for example Deforest *et al.*, 1998), with temperatures reaching a maximum relatively close to the coronal base (see Wang, 1998).

To explore the conditions within coronal holes further, it may be useful to examine the differential emission measure of the plasma observed as a function of position and height. It may then be possible considering the relatively long lifetimes of the structures present to use topographic techniques in conjuction with simple thermal arguments to determine the run of temperature in the different zones of coronal holes.

7.3 Temperature Structure of the Diffuse Corona

The temperature structure of the diffuse regions was investigated, and compared with a simple conserved heat flux model. The model was found not to be able to reproduce the obtained temperature structure over the entire height range, although suitable fits were obtained above and below $\sim 1.07R_\odot$. The emission if well approximated as radial and spherically symmetric coronal, as suggested by Sturrock et al. (1997), would have the consequence that substantial energy input (of the order 2×10^5ergs/cm^3/s) is required near the coronal base ($\rho < 1.2$). There is also an indication from these data that the volumetric heating rate is positively related to the emission measure, and thus the pressure of a region. Withbroe (1988) came to a similar conclusion as a result of his work, where it was found that 'the characteristic dissipation length for the mechanical energy input responsible for plasma heating in the corona increases with decreasing pressure'.

It is important to investigate the validity of some of the assumptions used in the course of this work. These are principly associated with the geometry, flow and general nature of the regions under investigation. In a manner similar to that mentioned for the coronal regions it would be useful to use the differential emission measure distribution of the plasma in different zones and heights of the diffuse corona to attempt to distinguish different components and or geometrical effects. This may also be aided by the simultaneous use of the green line images of the corona like those provided by the Lasco instrument on SOHO to identify the locations of the large scale arches which appear to be relatively clear in these images.

7.4 The Heating of Large Scale Loops

The temperature structure along a large scale loop structure which appeared to be embedded or part of the diffuse corona has been obtained and compared with simple representations of the coronal heating function. It was found that a heating mechanism which deposits heat into the overlying corona uniformly could reproduce the data. and exclude such models with which energy is deposited either very close to the coronal footpoints or at the apex of the loop. These latter rejected forms of heating may however also be able to produce similar temperature profiles if the models are made increasing complex. In the case of the exponential heating, allowing the scale length of the heating rate to extend to approximately a third of loops length, and in the case of heating at the loops apex distributing it over a distance on either side of the apex (as may be the case for slow shocks) may also produce similar profiles.

It is clear that the region which is most important to place constraints on the heating mechanism responsible for heating these large scale loops is at or around their apex. These regions should be subject to future observations, to investigate the temperature distribution within this region and its evolution, in attempt to extend the analysis of chapter 6. The use of DEM analysis as mentioned for the diffuse work, would also play an integral part in identifying the nature of these large scale arches and their relationship with the surrounding corona.

Acknowledgements

I would like to acknowledge and thank my supervisor Professor J. Leonard Culhane **FRS** for advice and encouragement given in the course of this work. It truly would not have been as enjoyable or productive without your guidance, Thanks. Special thanks is also due to Dr's Louise Harra-Murnion and Sarah Mathews, who must be credited with getting me to submit to their demands for weekend reading material, and thus in improving the clarity of this work which resulted from their ardent proof reading.

I would also like to acknowledge and thank the PPARC for funding for three of the years of study I undertook at the MSSL. To Annick Rouillon to whom I dedicate this work, thank you for the support and backing you generously extended to me.

Bibliography

[1] Abdelatif, T. E., 1987, **ApJ**, 322, 494-502

[2] Alexander, D., & Katsev, S., 1996, **SolPhys**, 167, 153-166

[3] Alfven, H., 1947, **MNRAS**, 107, 211

[4] Anderson, S. W., Raymond, J. C., and Ballegooijen, A. V., 1996, **ApJ**, 457, 939-948

[5] Athay, R. G., 1990, **ApJ**, 362, 364-369

[6] Altschuler, M. D., Trtter, D. E., and Orrall, F. Q., 1972, **SolPhys**, 26, 354

[7] Babcock, H. W., & Babcock, H. D., 1954, **ApJ**, 121, 349

[8] Beckmann, P., & Spizzichino, A., 1963, in **The Scattering of Electromagnetic Waves from Rough Surfaces**. 81-90

[9] Biermann, L. 1948, **Zs f. Astrophys**, 25, 161

[10] Bornmann, P. L., & Strong, K. T., 1988, **ApJ**, 1014-1025

[11] Burnight, T. R., 1949, **Phys. Rev.**,76, 165

[12] Cook, J, W, Cheng, C.-C., Jacombs, V. L., and Antiochos, S. K., 1989, **ApJ**, 1176-1183

[13] Culhane, J, L, 1966, **PhD Thesis**, University College London

[14] Culhane, J, L, 1996, **Advances in Space Research**, 17, 29

[15] Culhane, J, L, 1997, **Advances in Space Research**, 19, 1839-1848

[16] David, C, Gabriel, A. H., Bely-Dubau, F., Fludra, A., Lemaire, P., Wilhelm, K., 1998, **Astron. Astrophys.**, 336, L90-L94

[17] Davila, J, M, 1987, **ApJ**, 317, 514-521

[18] Debye, P., 1914, **Ann. Phys. (Leipzig)** , 43, 49

[19] Deforest, C.E., Hoeksema, J.T., Gurman, J.B., Thomson, B.J., Plunkett, S.P., Howard, R., Harrison, R.C., Hasslerz, D. M., **SolPhys**, 175, 393-410.

[20] Dowdy, J. F., Jr.; Moore, R. L., & Emslie, A. G., 1987, **SolPhys**, 112, 255-279

[21] Dupree, A. K., 1972, **ApJ**, 178, 527-542

[22] Edlén, B., 1942, **Z. Astrophys**, 22, 30

[23] Endler, F., Hammer, R., and Ulmschneider, P., 1979, **Astron. Astophys.**, 73, 190

[24] Falconer, D. A., 1994, **NASA Technical Memorandom**, 104616

[25] Falconer, D. A., Moore, R. L., Porter, J. G., Gary, G. A., and Shimuzu, T., **ApJ**, 482, 519

[26] Foley, C. A., Culhane, J. L., Acton, L. W., & Lemen, J. R., *in proceedings* **Magnetohydrodynamic Phenomena in the Sun and other Stellar Atmosphere's**, Makuhari, 1995

[27] Fuller,R., Lemen, J., Acton, L. W., 1994, **SXT Calibration Note 37a**

[28] Galvin, A. B., Ipavich, F. M., Gloekler, G., Hovestadt, D., Klecker, B., & Scholer, M., 1984, **Journal of Geophysical Research**, 89, 2655

[29] Georgoulis, M. K., Vlahos, L., 1996, **ApJL**, 469, 135

[30] Grossmann, W. & Smith, R. A., 1988, **ApJ**, 332, 476-498

[31] Grotrian, W., 1939, **Naturwissenschaften**, 27, 14

[32] Guhathakurta, M., Rottman, G. J., Fisher, R. R., Orrall, F. Q., & Altrock, R. C., 1992, **ApJ**, 388, 633-643

[33] Habbal, S. R., Esser, R., & Arndt, M. B. 1993, **ApJ**, 413, 435

[34] Hara, H., Tsuneta S., Lemen, J. R., Acton, L. W., & McTiernan, J. M. 1992, **PASJ**, 44, 135

[35] Hara, H., Tsuneta, S., Acton, L. W., Bruner, M. E., Lemen, J. R., & Ogawara, Y. 1994, **PASJ**, 46, 493

[36] Hara, H., **PhD Thesis**, 1996

[37] Hastings, C. S., 1873, **Amer. J. Sci.**, 5, 539

[38] Heyverts, J., & Priest, E. R., 1983, å, 117, 220

[39] Hiei, E., Hundhausen, A. J., Sime, D. G., 1993, **Geophysical Research Letters**, 20, 24, 2785-2788

[40] Hood, A. W., Gonzalez-Delgado, D., and Ireland, J., 1997, å, 324, 11-14

[41] Hoover, R. B., (*Editor*), 1989, **Papers presented at the 1989 SPIE conference " X-ray/EUV Optics for Astronomy and Microscopy"**, Proc SPIE, 1160

[42] Hoyle, F., and Bates, D. R., 1948,**Terr. Mag.**, 53, 51

[43] Hudson, H. S., 1991, **SolPhys**, 1991, 133, 357

[44] Hudson, H. S., Acton, L. W., & Freeland, S. L., 1996, **ApJ**, 1996, 470, 629

[45] Hulbert, E.O., 1938, **Phys. Rev.**, 53, 344.

[46] Kano,R and Tsuneta, S, 1995, **ApJ**, 454, 934

[47] Kano,R and Tsuneta, S, 1996, **PASJ**, 48, 535-543

[48] Klimchuk. J. A., & Gary, D.E., 1995, **ApJ**, 448, 925

[49] Klimchuk, J. A., Lemen, J. R., Feldman, U., Tsuneta, S., Uchida, Y., 1992, **PASJ**, vol 44, 5, L181-L185.

[50] Ko, Y.-K., Fisk, L.A., Geiss, J., Gloeckler, G., & Guhathakurta, M., 1997, **SolPhys**, 171, 345

[51] Kopp, R. A., **SolPhys**, 1972, 27,373

[52] Krucker, S., Benz, A. O., 1998, **ApJ**, 501, 213

[53] Lemen, J., Acton, L. W., Brown, W. A., Bruner, M. E., & Catura, R. C., 1991, **Advances in Space Research**

[54] Lockyer, J.N., 1870, **Remarks on the Recent Eclipse of the Sun as Observed in the United States , London**

[55] Lyot, B., 1937, **L'Astronomie**, 51, 203

[56] Martens, P. C., Acton, L. W., & Lemen, J. R., 1995, **SolPhys**, 157, 141.

[57] Marsden, P. C., and Smith, E. J., 1996, **Advances in Space Research**, 17, 293

[58] Martyn, D. F., 1946, **Nature**, 158, 632

[59] Mariska, J. T. 1978, **ApJ**, 225, 252

[60] Mariska, J. T. & Withbroe, G. L., 1975, **SolPhys**, 44, 55-68

[61] Mariska, J. T., & Withbroe, G. L., 1978, **SolPhys**, 60, 67

[62] Maxson C. W., & Vaiana, G. S. 1977, **ApJ**, 215, 919

[63] Mewe, R., Gronenschild, E. H. B. M., & Van den Oord, G. H. J. 1985, **Aston. &Astr. supp. ser.**, 62, 197

[64] Mewe, R., Lemen, J. R., & Van den Oord, G. H. J. 1986, **Aston. &Astr. supp. ser.**, 63, 511

[65] Meyer, J.-P., 1985, **ApJ Suppl.**, 57, 173.

[66] Michette., A. G., 1993, in **X-ray science and technology**, eds Michette., A. G., & Buckley., C. J., 1993

[67] Mitchell, S.A., 1913, **ApJ**, 38, 407

[68] Moore, R., Porter, J., Roumeliotis, G., Tsuneta, S., Shimuzu, T., Sturrock, P. A., Acton, L. W., in **proceedings of the Kofu Symposium, Kofu, Japan**, 1993, 89-92

[69] Munro, R. H., & Withbroe, G. L. 1972, **ApJ**, 176, 511

[70] Nariai, K., 1987, **Appl. Optics**, 26, 4428

[71] Nariai, K., 1988, **Appl. Optics**, 27, 348

[72] November, R. H., & Kouchmy, S., 1996, **ApJ**, 466, 512

[73] Ofman, L., Klimchuk, J.A., and Davila, J. M., **ApJ**, 493, 474-479

[74] Owocki, S. P.,Holzer, T. E., & Hundhausen, A. J. 1983 **ApJ**, 275, 354

[75] Parker, E. N., 1958, **ApJ**, 128, 664

[76] Parker, E. N., 1983, **ApJ**, 264, 642

[77] Parker, E. N., 1988, **ApJ**, 330, 474

[78] Parker, E. N., 1991, **ApJ**, 376, 355-363

[79] Phillips, A. T., 1996, **Advances in Space Research**, 17, 39-42

[80] Poletto, G., Vaiana, G. S., Zombeck, M. V., Krieger, A. S., & Timothy, A. F., 1975, **SolPhys**, 44, 83-89

[81] Porter, L, J, and Klimchuk, J,A, 1995, **ApJ**, 454, 499-511

[82] Priest, 1997, private communication

[83] Raymond, J. C., & Doyle, J. G. 1981, **ApJ**, 247, 686

[84] Rosner, R., Tucker, W. H., & Vaiana, G. S., 1978, **ApJ**, 220, 643-665

[85] Saito, K. 1970, **Ann. Tokyo Obs.**, 12, 53

[86] Sandbaek, O., & Leer, E., 1995, **ApJ**, 454, 486-498

[87] Schwarzschild, M., 1948, **ApJ**107, 1

[88] Scudder, J. D., 1992, **ApJ**, 398, 299-318

[89] Scudder, J. D., 1994, **ApJ**, 427, 446-452

[90] Sylwester, J., Sylwester, B., Siarkowski, M., 1996, in **Magnetic Reconnection in the Solar Atmosphere**, p244

[91] Spitzer, L., Jr. 1962, **Physics of Fully Ionised Gases** , Interscience Tracts on Physics and Astronomy, 2nd ed., Interscience Publishers, New York, London. p. 1

[92] Sturrock, P. A., Wheatland, D., & Acton, L. W., 1996, **ApJ**, 461, L115-117

[93] Tsuneta, S. et al., 1991, **SolPhys**, 136, 37

[94] Vaiana, G. S., Krieger, A. S., and Timothy, 1973, ?

[95] Vegard, L., 1938, **Geophys. Publ.**, 12, 5

[96] Wang, Y. -M., 1998, **ApJL**, 501, L145

[97] Withbroe, G. L. 1988, **ApJ**, 325, 442

[98] Wilhelm, K., Marsch, E., Dwivedi, B. N., Hassler, D. M., Lemaire, P., Gabriel, A. H., & Huber, M. C. E., **ApJ**, 500, 1023

[99] Wolter, H., 1952, **Ann Phys. 6th ser.** 10, 94

[100] Wolter, H., 1952a, **Ann Phys. 6th ser.** 10, 286

[101] Young, C. A., 1895, **The SUN** , London, Kegan Paul

[102] Yoshida, T., & Tsuneta, S., 1996, **ApJ**, 459, 342

[103] Zhoa, P., & Van Speybroeck, L.P., 1995, **SPIE**, 2515, 391